UNIVERSITY OF CALIFORNIA, SAN DIEGO

Engineering Smart Drug Delivery Systems to Treat Inflammatory Disorders

A dissertation submitted in partial satisfaction of the
requirements for the degree
Doctor of Philosophy

in

Chemical Engineering

by

Viet Anh Nguyen Huu

Committee in charge:

Professor Adah Almutairi, Chair
Professor Kang Zhang, Co-Chair
Professor Yi Chen
Professor Michael Heller
Professor Jesse Jokerst

2017

The dissertation of Viet Anh Nguyen Huu is approved, and it is acceptable in quality and form for publication on microfilm and electronically:

_____

_____

_____

_____
Co-Chair

_____
Chair

University of California, San Diego

2017

DEDICATION

I dedicate this thesis to my friends and family.
Their support motivates me in my everyday life.

EPIGRAPH

It is not the strongest of the species that survives,
nor the most intelligent that survives.
It is the one that is most adaptable to change.
—Charles Darwin

TABLE OF CONTENTS

Signature Page iii

Dedication iv

Epigraph v

Table of Contents vi

List of Figures ix

List of Tables xiv

Acknowledgements xv

Vita xvii

Abstract xviii

Introduction 1
0.1 References 4

Chapter 1 Light-responsive Nanoparticle Depot to Control Release of a Small Molecule Angiogenesis Inhibitor in the Posterior Segment of the Eye 5
1.1 Abstract 5
1.2 Introduction 6
1.3 Methods 7
1.3.1 Nanoparticle formulation 7
1.3.2 *In vitro* release studies 8
1.3.3 UV calibration using lens explants 9
1.3.4 *In vivo* release of fluorescent dye 9
1.3.5 *In vitro* cytotoxicity assay 10
1.3.6 *In vivo* biocompatibility of materials 11
1.3.7 mRNA extraction and reverse transcription 12
1.3.8 Quantitative real-time polymerase chain reaction . 12
1.3.9 Histology 13
1.3.10 Laser-induced choroidal neovascularization (CNV) 13
1.3.11 Retinal and corneal tomography 14
1.4 Results 14
1.4.1 Light-triggered release in cells 14
1.4.2 Light-sensitive nanoparticles are biocompatible ... 16

1.4.3 Irradiation required for release does not damage the eye ... 17
1.4.4 Light-triggered release *in vivo* ... 20
1.4.5 Light-released nintedanib inhibits CNV ... 20
1.5 Discussion ... 22
1.6 Conclusions ... 24
1.7 Acknowledgements ... 24
1.8 Supporting Information ... 25
1.9 References ... 31

Chapter 2 Light-Triggered Chemical Amplification to Accelerate Degradation and Release from Polymeric Particles ... 34
2.1 Abstract ... 34
2.2 Introduction ... 35
2.3 Experimental Data ... 37
2.4 Conclusions ... 43
2.5 Acknowledgements ... 43
2.6 Supporting Information ... 45
2.6.1 General methods and instrumentation ... 45
2.6.2 Abbreviations ... 46
2.6.3 Synthesis of polymer **1** ... 47
2.6.4 Degradation of polymer **1** ... 50
2.6.5 Particle formulation and characterization ... 50
2.6.6 *In vitro* release from particles ... 53
2.6.7 Cytotoxicity assays ... 55
2.7 References ... 59

Chapter 3 In Vivo Visible Light-Triggered Drug Release From an Implanted Depot ... 62
3.1 Abstract ... 62
3.2 Introduction ... 63
3.3 Results and discussion ... 66
3.3.1 Design, light response and degradation mechanism 66
3.3.2 Formulation of Nile red-loaded polymeric particles and photo-induced release ... 71
3.3.3 Photorelease of dexamethasone from implanted depot ... 74
3.4 Conclusions ... 77
3.5 Acknowledgements ... 78
3.6 Supporting Information ... 78
3.6.1 General methods and instrumentation ... 78
3.6.2 Synthesis of **5** ... 80
3.6.3 Synthesis of **6** ... 81

3.6.4 Synthesis of **7** ... 82
3.6.5 Synthesis of **8** ... 83
3.6.6 Synthesis of polymer **1** ... 84
3.6.7 Synthesis of **2** ... 85
3.6.8 Synthesis of **3** ... 86
3.6.9 Photochemical synthesis of **3a** ... 87
3.6.10 Hairless mouse skin preparation ... 88
3.6.11 Irradiation studies of polymer **1** through mouse skin tissue filter ... 89
3.6.12 Formulation of P-**1**-NR by electrospray ... 92
3.6.13 Encapsulation efficiency of Nile red ... 93
3.6.14 Nile red release experiments from P-**1**-NR ... 93
3.6.15 Encapsulation efficiency of dexamethasone ... 94
3.6.16 *In vivo* release of dexamethasone ... 95
3.6.17 Cytotoxicity assay ... 96
3.7 References ... 110

Chapter 4 Drug depot responsive to recurrence of pathological angiogenesis for long-term management of retinal vascular disorders ... 112
4.1 Abstract ... 112
4.2 Introduction ... 113
4.3 Materials and Methods ... 115
4.3.1 Nanoparticle formulation ... 116
4.3.2 Quantification of aflibercept encapsulation and activity ... 117
4.3.3 Short-term therapeutic efficacy *in vivo* ... 118
4.3.4 Delivery material biocompatibility ... 119
4.3.5 Laser-induced choroidal neovascularization (CNV) 120
4.3.6 Analysis ... 121
4.4 Results ... 123
4.5 Discussion ... 128
4.6 Acknowledgments ... 130
4.7 Supporting Information ... 130
4.8 References ... 134

LIST OF FIGURES

Figure 0.1: General classification of drug delivery stimuli and action modalities. Adapted from Ref[5,6] with permission from American Chemical Society and Nature Publishing Group. Copyright 2011 American Chemical Society, 2016 Nature Publishing Group. 2

Figure 1.1: UV light triggers release of encapsulated molecules in cultured macrophages. A, Raw264.7 macrophages incubated with fluorescein diacetate-containing nanoparticles (FDA NP) were irradiated with UV light (365 nm, 5 min, 10 mW/cm^2) 16

Figure 1.2: Light-sensitive nanoparticles are biocompatible. A, Micrographs of H&E stained retinas 8 days after injections. Scale bar = 100 μm. B, Quantification of outer nuclear layer (ONL) thickness from histology sections 18

Figure 1.3: Irradiation required for release does not damage the eye. A, Representative optical coherence tomography scans through the retina (scale bar = 0.5 mm). B, Quantification of outer nuclear layer (ONL) thickness 19

Figure 1.4: Light-sensitive particles can release payload up to 30 weeks post-intravitreal injection. Fluorescent microscopy of retinal flat-mounts. Scale bar = 100 μm. 21

Figure 1.5: Light-triggered release of nintedanib (BIBF) post-injection inhibits CNV. A, Fluorescent microscope images of isolectin B4-Alexa Fluor 594 stained choroidal flat-mounts 2 weeks after CNV induction. 22

Figure 1.6: Gel permeation chromatography of UVSP polymer. Inset: calculated molecular weights from UV (320 nm) and light scattering (LS) detectors. 25

Figure 1.7: Nanoparticles formed by emulsion-evaporation are monodisperse. A, Size distribution of nanoparticles by dynamic light scattering (DLS). B, SEM of drop-casted nanoparticles. 26

Figure 1.8: UV light triggers release of encapsulated molecules in cultured RPSC cells. A, RPSC cells incubated with FDA-encapsulating NPs were treated with 5 min of 10 mW/cm^2 UV light. B, Quantification of fluorescence 26

Figure 1.9: UVSP is well-tolerated by Raw 264.7 mouse macrophage cells. MTT assay at 24 h of incubation (n = 3). 27

Figure 1.10: Exposure to UVSP does not affect expression of inflammatory cytokines in the retina. qRT-PCR 1 week after injection 28

Figure 1.11: Identification of benign irradiation conditions. Lenses exposed to varying intensities of UV were imaged using a gel imager (VersaDoc, Bio-Rad Laboratories) at three time points (the above image is a composite). 29
Figure 1.12: Irradiation of the eye does not cause long-term ocular tissue damage. A-B, H&E stained cornea (light pink) and lens (dark pink) tissue slices 8 weeks after procedure (A - non-irradiated eye; B - irradiated eye). Scale, 100 μm 30

Figure 2.1: Synthesis of polymer **1**. a) EDC, DMAP, DCM, (compound **2** used as the dicylohexylamine salt), 52%; b) i) TFA, DCM ii) acryloyl chloride, NEt_3, DCM, 0 °C, 49%; c) 5, 1,3-propanedithiol, NEt_3, DMSO, 42%. 36
Figure 2.2: a) Degradation scheme of polymer **1**. b) Initial rate of ketal hydrolysis at varying pH and with varying amounts of irradiation. c) ^{1}H NMR spectra of polymer samples after 23 days at pH 7.4 with 20 min UV irradiation 39
Figure 2.3: a) Quenching of fluorescence of Nile red encapsulated in nanoparticles of polymer 1 following irradiation with UV light.b) count rate of nanoparticles after irradiation 5 min (35 mW/cm^2, λ = 320-480 nm) by DLS. 41
Figure 2.4: Raw 264.7 mouse macrophage cells incubated (30 min, 37 °C) with nanoparticles a) in the absence of irradiation and b) irradiated for 5 min (10 mW/cm^2). Scale bars = 30 μm. c) Increase in FDA fluorescence; $p < 0.001$. 44
Figure 2.5: Nanoparticles of polymer **1** are well-tolerated by Raw 264.7 macrophages. MTT assay following 24 h incubation with nanoparticles, either intact or pre-irradiated for 5 min with UV light (10 mW/cm^2). 44
Figure 2.6: GPC chromatogram of polymer **1** and compound **4**. 49
Figure 2.7: Degradation of polymer **1** followed ^{1}HNMR. (A-B), ^{1}HNMR spectra of polymer **1** (A) before, (B) following 20 min irradiation (1.35 mW/cm^2), or (C) following 20 min irradiation and 1224 h incubation 51
Figure 2.8: GPC chromatograms of an a) irradiated and b) control (not irradiated) sample of polymer **1** after 0, 24, 115, and 336 h of incubation at 37 °C. 52
Figure 2.9: PDI of nanoparticles after irradiation 5 min (35 mW/cm^2, λ = 320-480 nm) by DLS. 54
Figure 2.10: MTT assay of polymer **1**. 58
Figure 2.11: MTT assay of cells incubated with particles composed of polymer 1 and irradiated for 5 min with UV light at 10 mW/cm^2. . . . 58

Figure 3.1: Visible light irradiation of particles composed of polymer 1 in aqueous media induces swelling and release of molecular cargo. Tertiary amines within the polymer backbone assist deprotonation of the aci-nitro intermediate in the hydrophobic particle ... 65
Figure 3.2: Tertiary amines modulate the photochemistry of ANBB in hydrophobic environments. (a, b) Compound 2 cleanly reacts upon irradiation with visible light (λ_{ex} = 400-500 nm, 0.18 W, 0.21 W/cm^2) in CH_2Cl_2 ($6 * 10^{-5}$ M) 69
Figure 3.3: Polymer **1** photodegrades upon irradiation with visible light in hydrophobic environment. (a) Spectral changes in the UV-Vis spectrum of polymer 1 irradiated in CH_2Cl_2 (0.04 mg/ml, 0.5 ml) with visible light 90
Figure 3.4: Visible light triggers polymer 1 photochemistry after passage through mouse skin. (a) Experimental setup. (b) Reaction progression of CH_2Cl_2solutions of polymer **1** (0.04 mg/ml, 0.5 ml) 91
Figure 3.5: Photo-triggered release of Nile red from photoexpansile polymer **1** particles (P-**1**-NR). P-**1**-NR (0.08 mg/mL, 0.5 mL, total amount Nile red per sample: 2.25 μg) in PBS (1X, pH = 7.4) .. 98
Figure 3.6: One-photon visible light photo-release of dexamethasone from an implanted depot reduces carrageenan-induced hind paw inflammation in mice. (a) Composition of P-**1**-Dex particle depot. (b) Representative IVIS image of mice implanted 99
Figure 3.7: Synthesis of polymer **1** and model compounds **2** and **3**. 99
Figure 3.8: ^{1}H NMR spectroscopic analysis of polymer **1** upon irradiation in $CDCl_3$ (3 mg/mL, 0.55 mL) reveals the initial formation of the photo-unstable nitro-alkene photoproduct, as compared to the spectra of **3a** 100
Figure 3.9: Polymer **1** becomes soluble in MeOH upon complete photoconversion (middle) in CH_2Cl_2 (6 x 10-5 M). Left, unirradiated polymer. The photoproducts are also partially soluble in water containing 1% w/v Pluronic F127 (right panel). 101
Figure 3.10: Polymer **1** photodegrades into smaller molecules upon irradiation in CH_2Cl_2. HPLC-MS analysis of MeOH-soluble material from **Figure 3.9**. Masses correspond to the mass of the smallest theoretical segment anticipated. 102
Figure 3.11: Visible light penetrates mouse skin. (a) Tissue filter (0.45 mm mouse skin between two glass coverslips). (b) Visible light irradiation through the tissue filter. 102
Figure 3.12: Representative SEM images of P-**1**-NR before (left) and after (right) 90 min of visible light irradiation. 103

Figure 3.13: Particle photolysis. (a) Changes in the UV-Vis spectra of P-**1**-NR (0.08 mg/ml, 1 ml) in water as it is irradiated with visible light (λ_{ex} = 400-500 nm, 0.18 W, 0.21 W/cm^2). (b) Changes in absorbance at 490 nm of P-**1**-NR over time 104
Figure 3.14: Representative SEM image of P-**1**-Dex and size distribution from SEM (middle graph) and DLS (right graph). 105
Figure 3.15: Distribution of NIR fluorescent depots in P-**1**-Dex+light (1 mark on tail) and P-**1**-Dex (3 marks on tail) mice (3 mice per group) over time as visualized by IVIS imaging (λ_{ex} = 780 nm, λ_{em} = 800 nm) 106
Figure 3.16: *In vivo* procedures. (a) Injection of the P-**1**-Dex depot in the hind hock. (b) Irradiation of the depot. (c) Measurement of the hind paw using a caliper. 107
Figure 3.17: Inflamed hind paw thickness over time of all experimental groups. The skin just above the left hind hock was injected subcutaneously with the indicated solution (25 μL; the P-**1**-Dex dose was 200 μg containing 2 μg Dex 108
Figure 3.18: Representative photographs of mice 24 h after injection of carrageenan. 108
Figure 3.19: Oedema in DPBS + Light mouse after light exposure for 3 h. Swelling resolved within 1 d. 109
Figure 3.20: Effects of P-**1** and polymer **1** on cell metabolism in Raw 264.7 mouse macrophages by MTT assay. (a) P-**1** before and after irradiation (90 min). (b) Polymer **1** before and after irradiation (90 min). 109

Figure 4.1: A. Schematic showing system design. B. Release of aflibercept (EY) from PSP nanoparticles in presence (black circles), and absence (white circles) of 100 mM H_2O_2 122
Figure 4.2: A. Fluorescence micrographs of flat-mounted retinas, with blood vessels stained green through a perfusion of FITC-Dextran before euthanasia. White area delineates avascular area of the flat-mount. Scale = 100 μm 124
Figure 4.3: A. In-vivo retinal fluorescence micrographs of rhodamine-labeled PSP particles injected IVT. B. Quantification of PSP particle retention from retinal micrographs in A. n = 6. Error bars represent SEM. 125
Figure 4.4: A. Heidelberg optical coherence tomographs (OCT) comparing sagittal sections of PSP- and saline-injected eyes. ETDRS grids below show quantified retinal thickness from OCT scans 126

Figure 4.5: A. Schematic representation of the experimental setup for visual acuity measurements. B. Comparison of visual acuity between healthy, PBS-injected, and PSP-injected eyes. n = 4. Error bars represent SD 127
Figure 4.6: A. Fluorescence micrographs showing stained CNV spots. Red - isolectin B4, Green - FITC-Dextran; Blue - DAPI. Scale = 100 μm. B. Quantification of CNV spot sizes between experimental groups. * $p < 0.05$; ** $p < 0.01$. Error bars represent SEM. 128
Figure 4.7: A. Dynamic light scattering intensity of formulated PLGA, and PSP nanoparticles. B. TEM micrograph of PSP particles. Scale = 200 nm. C. TEM micrograph of PLGA particles. Scale = 200 nm. 131
Figure 4.8: Release profile of VEGF-Trap from PLGA particles (black), PSP particles without peroxide (blue), and PSP particles in presence of 100 μM hydrogen peroxide (red). 131
Figure 4.9: Quantification of neovascular (A) and avascular (B) areas in ROP eyes comparing eyes treated with PSP-EY particles, and eyes co-injected with PSP-EY particles and N-acetylcysteine (PSP-EY+NAC). 132
Figure 4.10: Comparison of ERG scotopic waves in eyes of healthy eyes (WT), eyes injected with saline (PBS), and eyes injected with PSP nanoparticles (NP). Error bars represent SD. 132
Figure 4.11: A. Fluorescence micrographs showing stained CNV spots. Red - isolectin B4, Green - FITC-Dextran; Blue - DAPI. Scale = 100 μm. B. Quantification of CNV spot sizes between experimental groups. * $p < 0.05$. Error bars represent SEM. 133

LIST OF TABLES

Table 1.1: qRT-PCR primers 27

Table 3.1: Light power attenuation by glass slides and glass/mouse skin 90

Table 4.1: qRT-PCR primers 130

ACKNOWLEDGEMENTS

Foremost, I would like to express my gratitude to Prof. Adah Almutairi for her support, expertise and encouragement as my mentor and the chair of the committee. Her guidance has proven essential in my doctoral work.

I would also like to thank the rest of my committee for their scientific insight: co-chair Prof. Kang Zhang, Prof. Michael Heller, Prof. Jesse Jokerst, and Prof. Yi Chen.

I would also like to acknowledge the co-authors in my publications, including Dr. Carl-Johan Carling, Dr. Nadia Fomina, Dr. Caroline de Gracia-Lux, Sha He, Dr. Noah Johnson, Dr. Jacques Lux, Dr. Enas Mahmoud, Dr. Cathryn McFearin, and Dr. Jason Olejniczak. I am thankful to our collaborators: Dr. Kang Zhang, Dr. Jie Zhu, Dr. Jing Luo, and Dr. Jing Zhu. Without their help and guidance in work with animals, these studies would not have been possible. I would also like to thank the all the members of the Bioresposive Materials Lab: Dr. Minnie Chan, Dr. Guillaume Collet, Arnold Garcia, Dr. Alexandra Foucault-Collet, Sangeun Lee, Dr. Mathieu Lessard-Viger, Dr. Amy Moore, Jessica Moore, Wangzhong Sheng, Dr. Sophia Suarez.

Introduction, in full, is currently being prepared for submission for publication of the material. Nguyen Huu, Viet Anh; Almutairi, Adah. The dissertation/thesis author was the primary investigator and author of this material.

Chapter 1, in full, is a reformatted reprint of the material as it appears

in Journal of Controlled Release 2015. Nguyen Huu, Viet Anh; Luo, Jing; Zhu, Jie; Zhu, Jing; Patel, Sherrina; Boone, Alexander; Mahmoud, Enas; McFearin, Cathryn; Olejniczak, Jason; de Gracia Lux, Caroline; Lux, Jacques; Fomina, Nadezda; Huynh, Michelle; Zhang, Kang; Almutairi, Adah, Elsevier, 2015. The dissertation/thesis author was the primary investigator and author of this paper.

Chapter 2, in full, is a reformatted reprint of the material as it appears in Chemical Science 2016. Olejniczak, Jason; Nguyen Huu, Viet Anh; Lux, Jacques; Grossman, Madeleine; He, Sha; Almutairi, Adah, ACS Press 2015. The dissertation/thesis author was the co-author of this paper.

Chapter 3, in full, is a reformatted reprint of the material as it appears in Chemical Science 2015. Carling, Carl-Johan; Viger, Mathieu; Nguyen Huu, Viet Anh; Garcia, Arnold; Almutairi, Adah, RSC Press, 2015. The dissertation/thesis author was the co-author of this paper.

Chapter 4, in full, is currently being prepared for submission for publication of the material. Nguyen Huu, Viet Anh; Zhu, Jie; Luo, Jing; Collet, Guillaume; de Gracia Lux, Caroline; Zhang, Kang; Almutairi, Adah. The dissertation/thesis author was the primary investigator and author of this paper.

VITA

2011	Bachelor of Science, California Institute of Technology
2012	Graduate Teaching Assistant, Department of Nanoengineering, University of California, San Diego
2012	Master of Science, University of California, San Diego
2017	Doctor of Philosophy, University of California, San Diego

PUBLICATIONS

V.A. Nguyen Huu, J. Luo, J. Zhu, J. Zhu, S. Patel, A. Boone, E. Mahmoud, C. McFearin, J. Olejniczak, C. de Gracia Lux, J. Lux, N. Fomina, M. Huynh, K. Zhang, A. Almutairi. "Light-responsive nanoparticle depot to control release of a small molecule angiogenesis inhibitor in the posterior segment of the eye", *J Control Release*, **200**, 71-77 (2015)

C.J. Carling, M.L. Viger, **V.A. Nguyen Huu**, A.V. Garcia, A. Almutairi. "In vivo visible light-triggered drug release from an implanted depot", *Chem Sci*, **48** (10), 3166-3172 (2015)

J. Olejniczak, **V.A. Nguyen Huu**, J. Lux, M. Grossman, S. He, A. Almutairi. "Light-triggered chemical amplification to accelerate degradation and release from polymeric particles", *Chem Comm*, **51** (95), 16980-16983 (2015)

Z.N. Zhang, B. Freitas, H. Qian, J. Lux, A. Acab, C.A. Trujillo, R.H. Herai, **V.A. Nguyen Huu**, J.H. Wen, S. Joshi-Barr, J.V. Karpiak, A.J. Engler, X.D. Fu, A.R. Muotri, A. Almutairi. "Layered hydrogels accelerate iPSC-derived neuronal maturation and reveal migration defects caused by MeCP2 dysfunction", *PNAS*, **113** (12), 3185-3190 (2016)

N.J.J. Johnson, S. He, **V.A. Nguyen Huu**, A. Almutairi. "Compact Micellization: A Strategy for Ultra-high T1 Magnetic Resonance Contrast with Gadolinium-Based Nanocrystals." *ACS nano*, **10** (9), 8299-8307 (2016)

C.-J. Carling, J. Olejniczak, A. Foucault-Collet, G. Collet, M.L. Viger, **V.A. Nguyen Huu**, B.M. Duggan, A. Almutairi. "Efficient red light photo-uncaging of active molecules in water upon assembly into nanoparticles", *Chem Sci*, **7** (3), 2392-2398 (2016)

J. Olejniczak, G. Collet, **V.A. Nguyen Huu**, M. Chan, S. Lee, A. Almutairi. "Biorthogonal click chemistry on poly (lactic-co-glycolic acid)-polymeric particles", *Biomater. Sci.*, Advance Article (2017)

ABSTRACT OF THE DISSERTATION

Engineering Smart Drug Delivery Systems to Treat Inflammatory Disorders

by

Viet Anh Nguyen Huu
Doctor of Philosophy in Chemical Engineering

University of California San Diego, 2017

Professor Adah Almutairi, Chair
Professor Kang Zhang, Co-Chair

Drugs work best when dosed right. For maximum therapeutic efficacy, one needs to deliver the drug to the right place at the right time. This dissertation exploits the recent advances in nanotechnology and chemistry for the design smart nanoscale constructs that can be triggered to disassemble and deliver encapsulated drugs. We design and evaluate light- and inflammation-sensitive systems for treatment of inflammatory diseases in animals. In Chapter 1, we demonstrate safety and efficacy of a UV light-triggered particles for controlled delivery of anti-angiogenics to treat age-related macular degeneration. The drugs are physically entrapped in a polymeric particle comprised of a series of self-immolative quinone-methide-

based monomers protected with a light-sensitive moeity. The cleavage of these moeities results in a scission in the polymeric backbone, leading to the release of the encapsulated drugs. In Chapter 2, we explore chemical signal amplification as a strategy to improve sensitivity of the light-triggered drug delivery systems. We altered the polymer so that photocleavage unmasks acidic groups that then provide intramolecular assistance to ketal hydrolysis in the polymer backbone, resulting in significant polymer degradation upon a brief, low power trigger. Chapter 3 focuses designing a system with a longer wavelength light as the trigger for degradation. Red-shifting the actuating wavelength increases its tissue penetration and allows control over drug delivery at greater depth. In Chapter 4, we investigate if a polymer that reacts and degrades upon an increase in concentration of reactive oxygen species can be used as a drug delivery vehicle for the eye. As pathophysiology of macular degeneration involves oxidative stress, we examine the feasibility of delivering drugs using an inflammation-sensitive depot. This approach tailors release of drugs to the progression of disease, and thus will be useful in its long-term management.

Introduction

Drug delivery systems have been developed to transport pharmaceutically active agents into the body safely, with the goal of maximizing the therapeutic effect and reducing side-effects to healthy tissue.[1] This was historically achieved by changing the rate of release of the drug. Formulation of the drug with inactive excipients resulted in diffusion barriers slowing down the drug release, prolonging its bioavailability while reducing the usual "spike" in drug concentration upon ingestion.[2] More recent advances in science have resulted in the development of controlled, or "smart", drug delivery systems.[3,4] Smart drug delivery systems comprise of materials that are sensitive to external and internal signals, and interact with or are actuated by them. The resulting action of the material, e.g. swelling, degradation, eventually results in delivery of the therapeutic molecule at the site of actuation[5,6] (Figure 0.1). Their efficacy is limited, however, by our understanding of the human body, and the processes that occur in diseased and healthy tissue.

Due to their unique nanoscale properties and specific bio-functions, various nanomaterials provide benefits and new opportunities for the smart drug delivery systems. Their high surface-to-volume ratio results increase their dissolution

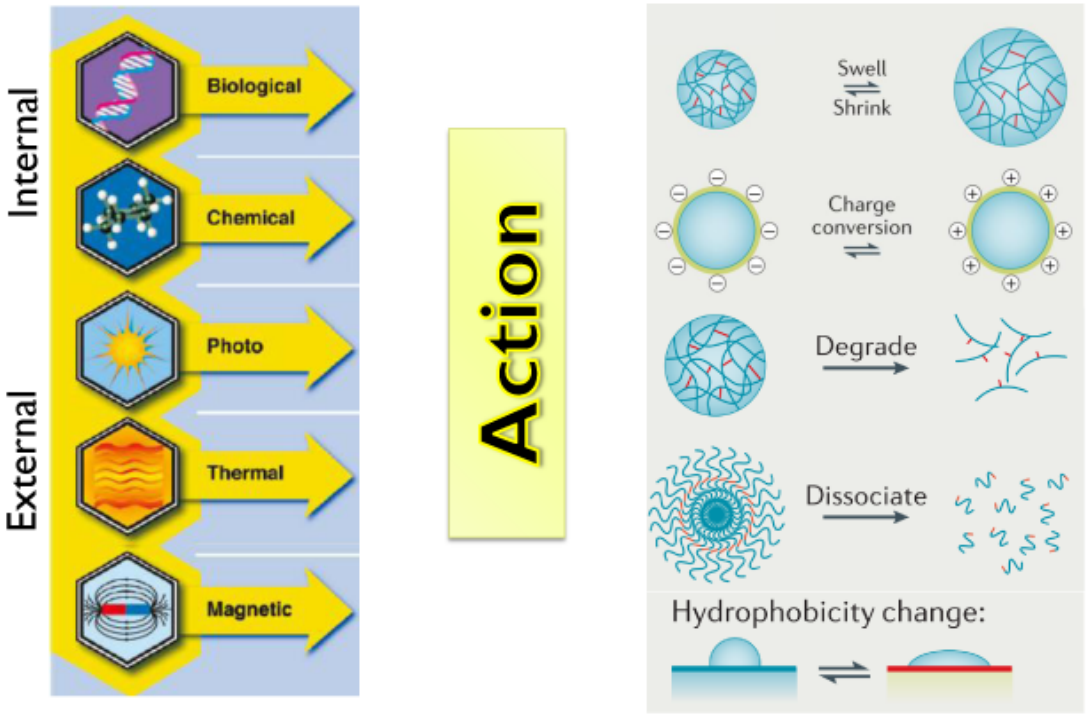

Figure 0.1: General classification of drug delivery stimuli and action modalities. Adapted from Ref[5,6] with permission from American Chemical Society and Nature Publishing Group. Copyright 2011 American Chemical Society, 2016 Nature Publishing Group.

rate, helping overcome solubility-limited bioavailability.[7] Due to their dimensions, they are able to mimic endogenous cells or biomolecules and undergo similar bio-interactions. For example, platelet-mimicking nanoparticle-based drug delivery systems can selectively accumulate and specifically bind to the blood clot sites with controlled release behavior.[8] Although recent research and reviews have devised and summarized several novel aspects for nanomaterials used as smart drug carriers, very few of them have been finally translated into clinics for real-world applications. The design of nanomaterials as drug carriers should address the follow-

ing key issues: sufficient biocompatibility and biodegradability; good stability in physiological conditions; and high drug loading and low toxicity. However, besides the primary requirement for safety and therapeutic efficacy, industrial scale-up for drug delivery systems is also a prerequisite for these systems to be commercially viable.

In this thesis, we design of smart materials capable of responding to extrinsic and intrinsic signals, and validate their efficacy in delivering drugs in preclinical animal models. Our focus is on polymeric materials, as they are very processable, with industrially-viable scale-up options. Polymeric systems can be used to physically entrap drugs through established formulation techniques, such as emulsion-evaporation, making them a platform technology that can be applied to multiple types of drug molecules. Our primary mode of action is degradation, as it leads to the polymeric vehicles disassembling into small molecules that are easily cleared from the body. We seek to test biocompatibility, physiological stability, and therapeutic efficacy of these system in diseased animals, with the goal of assessing their viability in addressing unmet medical needs.

0.1 References

(1) G. Tiwari, R. Tiwari, B. Sriwastawa, L. Bhati, S. Pandey, P. Pandey and S. K. Bannerjee, *Int J Pharm Investig*, 2012, **2**, 2–11.

(2) R. Langer and J. Folkman, *Nature*, 1976, **263**, Langer, R Folkman, J England Nature. 1976 Oct 28;263(5580):797-800., 797–800.

(3) J. Kost and R. Langer, *Advanced Drug Delivery Reviews*, 2012, **64**, 327–341.

(4) D. Liu, F. Yang, F. Xiong and N. Gu, *Theranostics*, 2016, **6**, 1306–23.

(5) A. P. Esser-Kahn, S. A. Odom, N. R. Sottos, S. R. White and J. S. Moore, *Macromolecules*, 2011, **44**, 5539–5553.

(6) Y. Lu, A. A. Aimetti, R. Langer and Z. Gu, *Nat Rev Mater*, 2016, **2**, 1–17.

(7) B. E. Rabinow, *Nature Reviews Drug Discovery*, 2004, **3**, 785–796.

(8) C. M. J. Hu, R. H. Fang, K. C. Wang, B. T. Luk, S. Thamphiwatana, D. Dehaini, P. Nguyen, P. Angsantikul, C. H. Wen, A. V. Kroll, C. Carpenter, M. Ramesh, V. Qu, S. H. Patel, J. Zhu, W. Shi, F. M. Hofman, T. C. Chen, W. W. Gao, K. Zhang, S. Chien and L. F. Zhang, *Nature*, 2015, **526**, 118.

Chapter 1

Light-responsive Nanoparticle Depot to Control Release of a Small Molecule Angiogenesis Inhibitor in the Posterior Segment of the Eye

1.1 Abstract

Therapies for macular degeneration and diabetic retinopathy require intravitreal injections every 4-8 weeks. Injections are uncomfortable, time-consuming, and carry risks of infection and retinal damage. However, drug delivery via noninvasive methods to the posterior segment of the eye has been a major challenge due to the eye's unique anatomy and physiology. Here we present a novel nanoparticle depot platform for on-demand drug delivery using a far ultraviolet (UV) light-degradable polymer, which allows noninvasively triggered drug release using brief, low-power light exposure. Nanoparticles stably retain encapsulated molecules in the vitreous, and can release cargo in response to UV exposure up to 30 weeks post-injection. Light-triggered release of nintedanib (BIBF 1120), a small molecule angiogenesis inhibitor, 10 weeks post-injection suppresses choroidal neovasculariza-

tion (CNV) in rats. Light-sensitive nanoparticles are biocompatible and cause no adverse effects on the eye as assessed by electroretinograms (ERG), corneal and retinal tomography, and histology.

1.2 Introduction

Neovascular age-related macular degeneration (AMD) is one of the most common eye disorders that impair vision and is the leading cause of blindness in the elderly.[1] The majority of treatments for AMD require monthly or bimonthly intravitreal injection of anti-angiogenic drugs, such as bevacizumab (Avastin), ranibizumab (Lucentis), and more recently, aflibercept (VEGF-Trap/Eylea).[2] Although the risk of adverse effects, such as cataracts or retinal detachment, with each injection is rare, it increases with the number of intravitreal injections.[3] Thus, strategies that reduce the frequency of injections while maintaining the therapeutic efficacy of these drugs are highly sought after. An ideal solution would also preserve ophthalmologist control over dosages to allow adjustment for each patient's response, which would maximize the efficacy of each injection.

While several systems have been developed to extend the lifetime of anti-angiogenics following intravitreal injection, including biodegradable implants,[4,5] liposomes,[6,7] micro-[8,9] and nanoparticles,[10,11] none allow ophthalmologist control over the timing of release. One of the most commonly used materials for this purpose is poly(lactic-co-glycolic acid) (PLGA), which can be tuned to release at

different rates by varying its composition and molecular weight. This reliance on a very simple and widely-used material does not take full advantage of recently developed technologies in the drug delivery field, which could allow on-demand[12,13] or disease-triggered[14,15] intravitreal release of AMD drugs. Here we propose a nanoparticulate drug delivery depot formulated from a light-degradable polymer for on-demand light-triggered release of drugs post-implantation.

To assess the efficacy of this system *in vivo*, we delivered nintedanib (BIBF 1120), a small molecule inhibitor of the receptors for VEGF, PDGF, and FGF,[16] and demonstrate that UV light-triggered release attenuates laser-induced choroidal neovascularization (CNV) in rats. To our knowledge, this is the first report of *in vivo* light-triggered release in the eye.

1.3 Methods

1.3.1 Nanoparticle formulation

Light-sensitive polymer was synthesized as previously published (MW = 7.6 kDa, PDI = 1.3 by gel permeation chromatography (Figure 1.6).[17] 10 mg polymer was dissolved in 270 μL dichloromethane, and 30 μL dimethyl sulfoxide (DMSO) containing 2 mg payload (fluorescein diacetate (FDA), calcein AM, BIBF1120) was added. The resulting solution was added to 6 mL of sterile-filtered 1% polyvinyl alcohol (PVA) in water, and probe sonicated for 4 min at 9-10 W (S-4000, Misonix Sonicators). Organic solvents were removed by evaporation under light vacuum

conditions while stirring at 600 RPM for 3 h. Remaining PVA was removed by concentrated mode tangential flow filtration (Pellicon XL, 500 kDa, Millipore) with 250 mL cell-culture grade water (HyClone) at 45 RPM. The retentiate was then freeze-dried with 100 mg trehalose as cryoprotectant. The size and distribution of particles were confirmed by dynamic light scattering (DLS, Zeta Nanosizer, Malvern Instruments), and scanning electron microscopy (SEM, FE-SEM 8500, Agilent). Loading and encapsulation efficiency were measured using UV-vis spectroscopy (UV-3600, Shimadzu) and fluorescence spectrophotometry (Jobin Yvon FL-1000, Horiba).

1.3.2 *In vitro* release studies

Raw 264.7 mouse macrophages or retinal progenitor cells were seeded at 20,000 cells/well on a 96-well plate 12 h before the experiment. Cells were washed twice with 100 ÂţL warm Dulbecco's phosphate buffered saline (DPBS) and incubated with 100 ÂţL of 2 mg/mL suspension of FDA-containing nanoparticles in media or media alone as controls for 3 h at 37 °C under 5% CO_2. Cells were again washed twice with 100 μL warm DPBS and replenished with fresh media, and free FDA was added to wells without particles as a positive control. Half of the particle-containing wells were irradiated with $8mW/cm^2$ of 365 nm UV light for 5 min (OmniCure S2000, Lumen Dynamics) to induce particle degradation. Green fluorescence from wells was measured using a plate reader (SpectraMax M5,

Molecular Devices), and images were collected using a fluorescence microscope (TS100F, Nikon).

1.3.3 UV calibration using lens explants

Adult Sprague-Dawley rats were euthanized by CO_2 asphyxiation followed by exsanguination, and their eyes were enucleated and stored at 4 °C in Belzer UW cold preservation media (Bridge to Life), supplemented with 100 μg/mL penicillin (Invitrogen), 100 μg/mL streptomycin (Invitrogen), and 200 μg/mL d-glutamine (Invitrogen) following published protocols.[18,19] Lenses were then carefully dissected from the globes and incubated in 4 mL Media 199 (Invitrogen) supplemented with 1% w/v of penicillin (100 μg/mL) and streptomycin (100 μg/mL) pre-incubated in 5% CO_2 atmosphere at 37 °C for 24 h. Non-cloudy lenses were either exposed to 10 min of UV light (365 nm, 12 mW/cm^2) or left unirradiated. The cloudiness was assessed visually and quantified through histograms in Adobe Photoshop CS2.

1.3.4 *In vivo* release of fluorescent dye

Sprague-Dawley rats (male, 4-8 weeks old) were anesthetized using 100 mg/kg ketamine and 10 mg/kg xylazine administered intraperitoneally. Both eyes were injected with 3 μL of a 200 mg/mL suspension of dry nanoparticle powder in DPBS by first piercing the inferotemporal quadrant with a 31 G insulin needle (BD Products), then inserting a 33 G syringe (Hamilton) through the puncture directly into the vitreous cavity. Both eyes were lubricated using a lubricant eye gel

(GenTeal Severe, Novartis). The irradiation protocol to induce drug release from light-sensitive nanoparticles was as follows: one eye was dilated by corneal application of 0.5% propacaine hydrochloride (ophthalmic solution, Bausch & Lomb), followed by a drop of 0.5% tropicamide (ophthalmic solution, Bausch & Lomb). After 5 min, the rat was anesthetized with ketamine/xylazine intraperitoneally, set on one side, and covered with 2 layers of nitrile gloves to protect the body from UV light. The dilated eye was irradiated for 5 min with 365 nm UV light at 8 mW/cm^2 (OmniCure S2000, Lumen Dynamics). After 45 min, rats were euthanized, and eyes were enucleated and fixed in 4% paraformaldehyde for 45 min. Retinas were then extracted, flat-mounted and imaged under a fluorescence microscope (Biorevo BZ-9000, Keyence).

1.3.5 *In vitro* cytotoxicity assay

Ultraviolet-sensitive polymer (UVSP) (5 mg) was dissolved in sterile DMSO (10 μL), and the solution was added to clear Dulbecco's Modified Eagle's Medium (DMEM) (990 μL). The resulting suspension was sonicated until uniform and further diluted to appropriate concentrations in DMEM/fetal bovine serum (FBS). Lyophilized particles containing FDA (5 mg) were resuspended in sterile media (1 mL) and half of the volume was irradiated for 5 min with UV light (10 mW/cm^2, λ_{ex} = 365 nm, OmniCure S2000 Curing System). Solutions were then diluted to appropriate concentrations in cell culture media. Raw 264.7 cells, seeded 24 h prior

to incubation on a tissue culture treated 96-well plate (Corning) at 20,000 cells/well in DMEM, were washed twice with PBS at 37 °C, incubated with polymer/particle suspensions in triplicate for 24 h at 37 °C in 5% CO_2, then washed twice again with PBS. Mitochondrial activity was then measured according to MTT assay kit instructions (Sigma-Aldrich). Triton-X (1% w/v, Sigma-Aldrich) was used as a positive apoptosis control. Absorbance at 570 nm normalized to background absorbance at 690 nm was measured using a plate reader (SpectraMax M5, Molecular Devices).

1.3.6 *In vivo* biocompatibility of materials

Sprague-Dawley rats (4-8 weeks, male) were anesthetized with ketamine and xylazine and injected intravitreously with 3 μL of a 200 mg/mL suspension of empty UVSP or PLGA nanoparticles in DPBS or 3 μL DPBS. Uninjected rats served as controls. Intraocular pressure (IOP) was measured in non-anesthetized animals at the same time of day using a veterinary tonometer (TONOVET, Icare) at 1, 5, and 7 days post-injection. Electroretinograms (ERGs) were also performed at 1 and 8 days post-injection following a previously reported protocol.[20] Briefly, rats were dark-adapted for 12 h, anesthetized, and given pupil-dilating solutions as described in the irradiation protocol above. Rats were examined within a Ganzfeld bowl (Diagnosys LLC), and electrodes were placed on each cornea, with a subcutaneously placed ground needle electrode in the tail. For scotopic ERG, the retina

was stimulated with a xenon lamp at 0.01 and 0.3 cd.s/m^2. For photopic ERG, rats were adapted to a background light of 10 cd*s/m^2, and light stimulation was set at 30 cd.s/m^2. Recordings were processed in Matlab and Excel.

1.3.7 mRNA extraction and reverse transcription

Sprague-Dawley rats (4-8 weeks, male) injected with UVSP, PLGA nanoparticles or DPBS, as well as controls (no injection) were euthanized 7 days post-injection, and their eyes were enucleated and retinas extracted. Tissue was homogenized by trituration in lysis buffer (QIAGEN), followed by centrifugation through QIAshredder homogenization columns (QIAGEN). mRNA was then extracted using an RNEasy Kit (QIAGEN). RNA concentration was determined by spectrophotometric optical density ratio (OD_{260nm}/OD_{280nm}, NanoDrop 2000, Thermo Scientific). Reverse transcription was carried out using Superscript III First-Strand Synthesis System (Invitrogen) with 800 ng RNA/reaction, primed with random hexamers.

1.3.8 Quantitative real-time polymerase chain reaction

Rat primer sequences for interleukin-1β (IL-1β), tumor necrosis factor-α (TNF-α), and glyceraldehyde 3-phosphate dehydrogenase (GAPDH) were obtained from literature,[21,22] and confirmed using Primer-BLAST (NCBI, Table 1.1). qRT-PCR was carried out using Power SYBR Green PCR Master Mix (PE Applied Biosystems) with 400 nmol/L of primers in a 7500 Fast Real-Time PCR System

(PE Applied Biosystems). Each cDNA sample was run in duplicate and quantified by comparative CT algorithm. The average of two values is reported. All gene expression levels were normalized to GAPDH.

1.3.9 Histology

Enucleated eyes were pierced at the cornea with a 27 gauge needle (BD Products) and fixed overnight in 4% PFA in PBS, followed by 24 h fixation in 30% sucrose in PBS. The ocular globe was then embedded in Tissue-Tek OCT Compound (Sakura Finetek) and stored at -80 °C until cryosectioning. Frozen sections of 20 μm thickness were cut using a microtome-cryostat and stained with hematoxylin and eosin (H&E). For paraffin sections, tissues were fixed for 24 h in 4% PFA in PBS, followed by 24 h fixation in 70% ethanol before embedding in paraffin blocks. Sections of 20 μm thickness were cut using a microtome and stained with H&E.

1.3.10 Laser-induced choroidal neovascularization (CNV)

Brown Norway rats (6-8 weeks, male) were subjected to laser-induced disruption of Bruch's membrane in both eyes using an Iridex OcuLight GL 532 nm laser photocoagulator (Iridex) with a slit lamp delivery system following pupil dilation with tropicamide eye drops and anesthesia with ketamine/xylazine. Five spots in the posterior pole of the retina were irradiated through the dilated pupil (150 mW, 75 μm spot, 0.1 s). Rats were sacrificed 2 weeks following laser photo-

coagulation, and their eyes were enucleated and fixed in 4% PFA. Choroids were then flat-mounted and stained with Alexa Fluor 594-conjugated isolectin IB4 (Life Technologies). Mounted slides were imaged by fluorescence microscopy at 10X magnification (Biorevo, Keyence), and images were analyzed in Adobe Photoshop CS2.

1.3.11 Retinal and corneal tomography

Sprague-Dawley rats were irradiated in one eye for 5 min at 8 mW/cm^2 of 365 nm light, and the contralateral eye was left as control. Corneal volume confocal tomography scans were taken with HRT3 Cornea Module (Heidelberg) before, after procedure, and followed until 6 weeks post-irradiation. Endothelial cell counts were obtained from section scans of the corneal endothelium analyzed in Heidelberg software. Retinal optical coherence tomographs (OCT) were taken using HRT3 Retina Module (Heidelberg) after procedure. The acquisition software was used to quantify outer nuclear layer (ONL) thickness. Eyes were then enucleated, cryosectioned, stained and imaged.

1.4 Results

1.4.1 Light-triggered release in cells

To test whether our UV-sensitive nanoparticles release the encapsulated molecules upon biocompatible irradiation, we formulated nanoparticles encapsu-

lating fluorescein diacetate (FDA) from the light-sensitive polymer (UVSP) using a single emulsion-evaporation procedure. FDA allows detection of release in cells because only the cleaved product, formed by hydrolytic activity of intracellular esterases, is fluorescent.[23] Particles were 178 nm, with a polydispersity index (PDI) of 0.06 measured by dynamic light scattering (DLS, Figure 1.7A); this size was confirmed by scanning electron microscopy (SEM, Figure 1.7B). Particles contained 0.5 μg FDA/ mg lyophilized powder as determined by dissolution in dichloromethane (DCM) and fluorescence measurements of the hydrolyzed FDA extracted into 0.1 N NaOH.

Raw 264.7 mouse macrophage cells were incubated with FDA-containing nanoparticles suspended in growth media. To eliminate the contribution of FDA released upon resuspension, cells were incubated with the nanoparticle suspension for 3 h, as fluorescein's fluorescence lasts a shorter period. Cells were then either irradiated with 365 nm UV light for 5 min at 8 mW/cm^2 or left untreated and incubated 30 min. Fluorescence increased over the incubation period only in irradiated cells, suggesting that FDA was released upon light exposure, allowing esterase activation of the dye (Figure 1.1A). The difference in fluorescence between irradiated and non-irradiated wells containing cells and FDA nanoparticles was 16 $\pm$ 2.7 fold as quantified by a plate reader (Figure 1.1B). Results in non-phagocytosing retinal progenitor cell lines were also consistent with light-triggered release; fluorescence in irradiated cells was 2.5-fold greater than in non-irradiated (Figure 1.8).

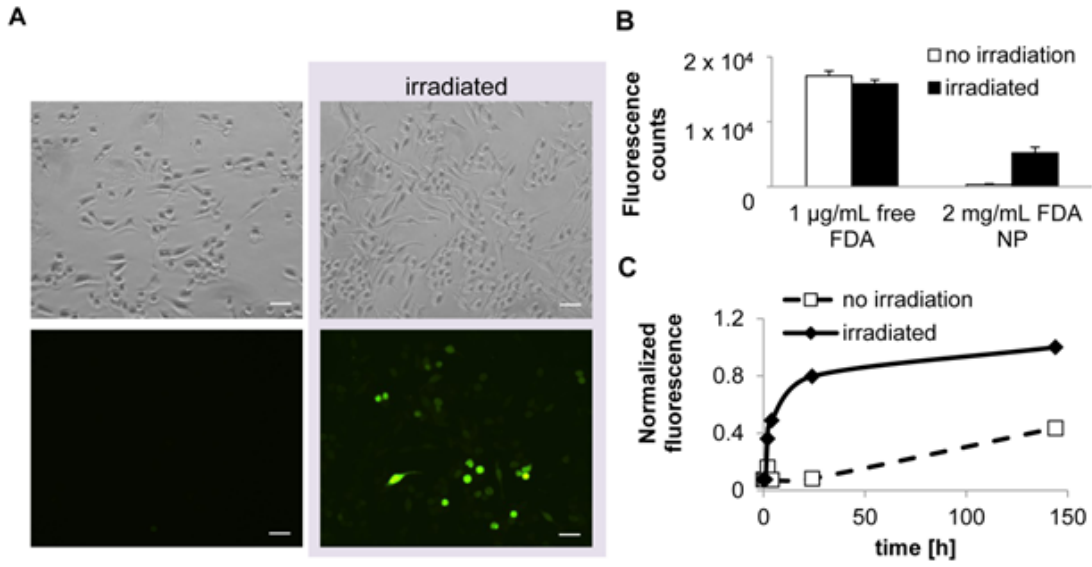

Figure 1.1: UV light triggers release of encapsulated molecules in cultured macrophages. A, Raw264.7 macrophages incubated with fluorescein diacetate-containing nanoparticles (FDA NP) were irradiated with UV light (365 nm, 5 min, 10 mW/cm^2). Scale bar = 100 μm. B, Quantification of fluorescence (n= 3 wells, $p < 0.001$). C. FDA release in phosphate buffer at 37 °C measured by fluorescence upon irradiation (Ex/Em = 490/514 nm).

1.4.2 Light-sensitive nanoparticles are biocompatible

To evaluate the safety of light-sensitive nanoparticles for use in live animals, we first examined the effect of irradiated and non-irradiated polymer and nanoparticles on mitochondrial activity by MTT assay. All materials were well-tolerated by Raw 264.7 cells at concentrations up to 500 μg/mL (Figure 1.9). We then tested their safety in the eye in live Sprague-Dawley rats by assessing their effects on intraocular pressure (IOP), retinal activity (by electroretinogram (ERG)), and retinal ONL (outer nuclear layer) thickness using the commonly used polymer PLGA as a standard for safety and PBS as a negative control (Figure 1.2).

To assess effects of acute exposurelight-sensitive nanoparticles, we analyzed retinal thickness a week after injection with light-sensitive nanoparticleslight-sensitive nanoparticles. Tissue histology sections stained with hematoxylin and eosin (H&E) reveal no difference in outer nuclear layer (ONL) thickness between eyes injected with light-sensitive nanoparticles compared to PBS and PLGA (Figure 1.2A, B). Nanoparticles caused no significant change in IOP compared to healthy animals either directly after injection with nanoparticles or a week after the procedure, similar to the effect of PBS (Figure 1.2C). Similarly, the effects of light-sensitive nanoparticles on ERG activity were similar to those of PLGA and PBS (Figure 1.2D); all injections caused a procedural drop in the ERG scotopic b-wave in both experimental and control groups, but all readings returned to normal within a week. Finally, we examined whether light-sensitive nanoparticles trigger an inflammatory response in the eye by measuring the expression of the inflammatory cytokines IL-1β and TNF-α post-injection by quantitative real-time polymerase chain reaction (qRT-PCR). No change in expression of any of these cytokines was detected; this lack of effect was similar to that of PBS and PLGA (Figure 1.10).

1.4.3 Irradiation required for release does not damage the eye

To address likely concerns about the light necessary to release drugs from our system, preliminary studies on irradiation conditions were carried out using cultured explanted rat lenses. By starting with 1 min at 40 mW/cm^2, and stepwise

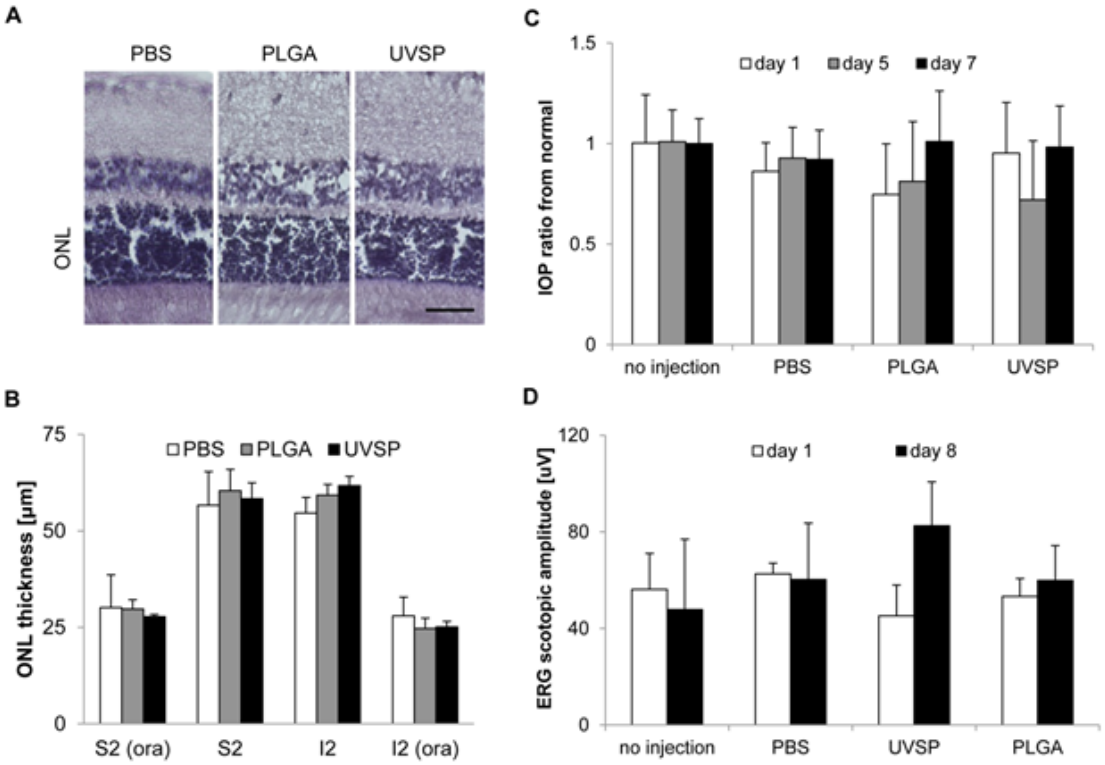

Figure 1.2: Light-sensitive nanoparticles are biocompatible. A, Micrographs of H&E stained retinas 8 days after injections. Scale bar = 100 μm. B, Quantification of outer nuclear layer (ONL) thickness from histology sections (S2 - superior quadrant, I2 - inferior quadrant, ora - vicinity of ora serrata). C, Intraocular pressure measurements following the injection of nanoparticles. D, Electroretinograms (ERG) of rod scotopic response after injection of nanoparticles (n = 3).

decreasing the irradiance, we found that exposing Sprague-Dawley rat lenses to 10 min of 365 nm UV light at 12 mW/cm^2 does not cause cloudiness within 48 h of exposure (Figure 1.11). To ensure that we were well within the safety threshold for lenses, *in vivo* experiments all employed irradiation of 5 min at 8 mW/cm^2. Optical coherence tomography revealed no acute effects of irradiation on the retina (Figure 1.3A, B). Moreover, comparison of corneal tomography scans of irradiated and non-irradiated eyes showed no significant effect of irradiation on endothelial cell count

(Figure 1.3C, E). The central corneal stroma thickness in the experimental animals did not differ from that in controls. No abnormalities such as corneal clouding or signs of cataracts were observed. Analysis of H&E-stained sections of whole eyes 8 weeks post-irradiation reveals no damage to the corneal endothelium, lens, or photoreceptor layers (Figure 1.12).

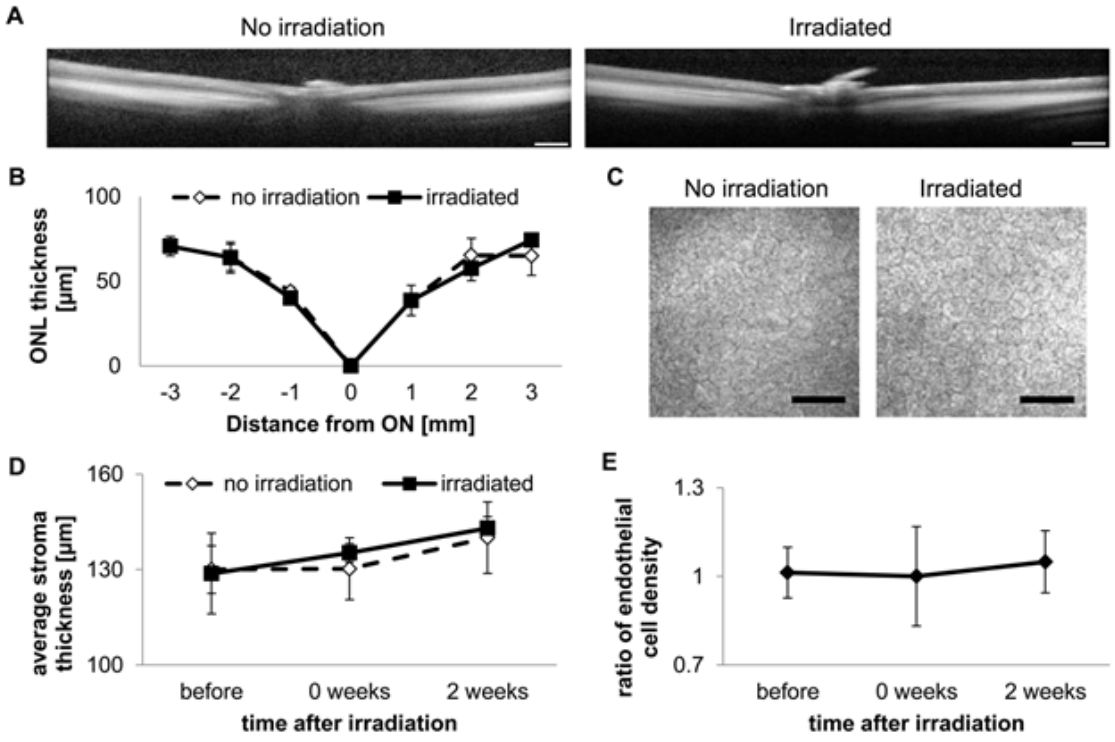

Figure 1.3: Irradiation required for release does not damage the eye. A, Representative optical coherence tomography (OCT) scans through the retina (scale bar = 0.5 mm). B, Quantification of outer nuclear layer (ONL) thickness (ON - optical nerve, positive - towards temporal quadrant, negative - towards nasal quadrant; n = 3). C, Representative confocal tomographs of the corneal endothelium 2 weeks post-irradiation (scale bar = 50 μm). D, Quantification of stromal thickness from volume cornea tomographs (n = 4). E, Quantification of endothelial cell count ratio (n = 4).

1.4.4 Light-triggered release *in vivo*

To determine whether the brief, low-power UV irradiation protocol developed above could trigger release of cargo in the eye, anesthetized Sprague-Dawley rats were injected in both eyes with FDA-containing nanoparticles. One eye of each rat was irradiated 3 h later (to allow fluorescence from FDA released upon resuspension of particles to fade) with UV light (365 nm, 8 mW/cm^2) and retinas were collected 45 min later and flat-mounted. Green fluorescence was significantly greater in irradiated eyes than non-irradiated controls, indicating light-triggered release and activation of FDA upon entering retinal cells (Figure 1.4A).

To determine the lifetime of non-irradiated particles in the eye, we used the same assay. Fortuitously, because FDA within nanoparticles is hydrolyzed after an extended period of time to form non-cell permeable fluorescein, non-irradiated eyes exhibit a positive, particulate fluorescence signal. Irradiation would thus release fluorescein, which is removed during flat-mounting. Particulate fluorescence that could be turned off upon irradiation was observed up to 7 months after injection (Figure 1.4 B,C).

1.4.5 Light-released nintedanib inhibits CNV

To explore the potential of light-sensitive nanoparticles as a delivery vehicle for therapeutic compounds, nanoparticles encapsulating the small molecule angiogenesis inhibitor nintedanib[16] were injected intravitreally into Brown Norway rats

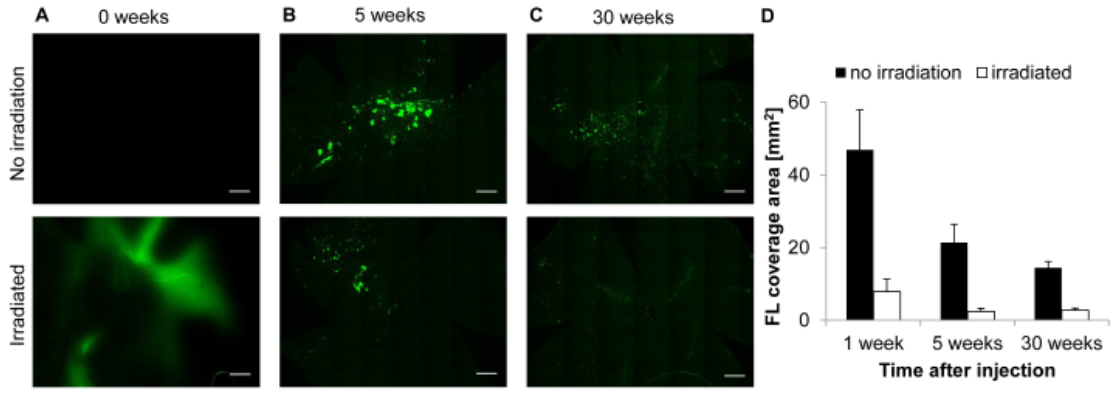

Figure 1.4: Light-sensitive particles can release payload up to 30 weeks post-intravitreal injection. Fluorescent microscopy of retinal flat-mounts. Scale bar = 100 μm.

prior to laser induction of choroidal neovascularization. Inhibition of vessel growth was compared to rats receiving PLGA particles containing nintedanib, free drug, or saline. To assess the stability of nintedanib encapsulation, CNV was induced in the animals either immediately or 10 weeks after injections. Light-released nintedanib inhibited angiogenesis significantly (as assessed by isolectin staining; $p = 0.012$), as observed in rats treated with free nintedanib ($p = 0.009$; Figure 1.5A, B). Importantly, CNV areas in rats receiving UV light-released nintedanib were significantly smaller than those in rats receiving PLGA-encapsulated nintedanib ($p = 0.028$), suggesting that light-triggered release delivers drug more effectively than slowly hydrolyzing PLGA nanoparticles. Importantly, UVSP nanoparticles retained their ability to release drug and inhibit angiogenesis when CNV was induced 10 weeks after the implantation. CNV areas following light-triggered release were significantly smaller than in rats receiving PLGA-encapsuated nintedanib (Figure 1.5C,

D).

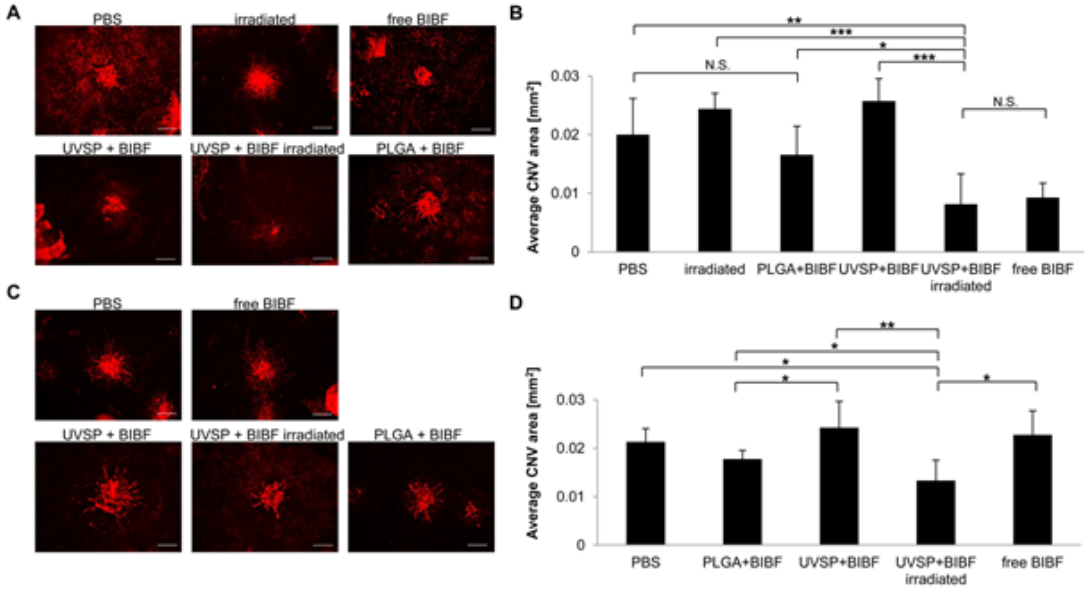

Figure 1.5: Light-triggered release of nintedanib (BIBF) post-injection inhibits CNV. A, Fluorescent microscope images of isolectin B4-Alexa Fluor 594 stained choroidal flat-mounts 2 weeks after CNV induction. Eyes were irradiated immediately post-injection (scale bar = 100 μm). B, Quantification of CNV spot size (n = 4-6). C, Choroidal flat-mounts from eyes irradiated 10 weeks post-injection, 2 weeks after CNV induction (scale bar = 100 μm). D, Quantification of CNV spot size (n = 4-6).

1.5 Discussion

Because most current anti-angiogenics are administered monthly (Avastin, Lucentis) or bimonthly (Eylea), delivery systems for these drugs must allow drug release at time points later than two months post-injection to offer a clinical advantage. The light-sensitive nanoparticles employed here retain and release therapeutically relevant amounts of drug after 10 weeks in the eye. Further, despite

polymer hydrolysis, both nanoparticles and encapsulated dye are present in the intravitreous space 30 weeks after injection. Our system therefore has potential to improve both of the above approaches by allowing noninvasive dosing long after injection.

The requirement for UV irradiation will likely raise concerns about the safety of our approach to control anti-angiogenic dosing, as UV causes both acute and prolonged adverse effects in the cornea (where it is primarily absorbed) as well as in the lens and retina.[24] A major concern is damage to the corneal endothelium, which cannot repair itself.[25,26] The UV wavelength used in our studies is 365 nm, which is in the lower energy end of UVA, close to the visible spectrum and within the range of ambient UV radiation. The effect of this wavelength of light on the eye has been extensively studied as cornea crosslinking (CXL) treatments for keratoconus require 30 min of irradiation at 3 mW/cm^2 of 365 nm light.[25,27] Though CXL therapy can cause cytotoxic effects in rabbits with thin corneas, and therefore in patients with advanced keratoconus,[28] without the UV absorber the dose cytotoxic to the endothelium has been reported to be 42.5 J/cm^2 at the surface of the cornea, equivalent to 270 min irradiation at 3 mW/cm^2, or 90 min irradiation at 8 mW/cm^2.[29,30] In contrast, the total energy density delivered by our light trigger is 2.4 J/cm^2 over 5 min, which is well within the reported safety regime for this wavelength, and is well-tolerated by the rat endothelium over 4 weeks post-irradiation. Our studies also show that 10 min exposure to UVA at 12 mW/cm^2, equivalent to

7.2 J/cm^2, is safe for the lens as it is well within the reported damage threshold of >70 J/cm^2.[29] Therefore, the irradiation protocol employed here is within the safety thresholds for the eye.

1.6 Conclusions

To our knowledge, this is the first report of *in vivo* light-triggered release of drug in the eye. The period for which carriers and encapsulated drug remain present in the intravitreous space and retain their ability to degrade upon irradiation, up to 30 weeks, is the longest yet reported for a nanoparticulate depot and far exceeds the usual 4-8 week interval between injections of anti-angiogenics. These results, combined with our demonstration of therapeutic efficacy following light-triggered release at 10 weeks post-injection and the safety of the light trigger, promise clinical relevance of this platform for intravitreal drug delivery. We are currently examining whether light can trigger release of multiple therapeutic doses of BIBF1120.

1.7 Acknowledgements

NMR spectra were collected at the UCSD Skaggs School of Pharmacy and Pharmaceutical Sciences NMR Facility. OCT and HRT tomographs were acquired at UCSD School of Medicine Core Imaging Facility, supported by the National Eye Institute (P30EY022589). This work was supported by an NIH New Innova-

tor Award (DP 2OD006499) and King Abdulaziz City for Science and Technology (through the KACST-UCSD Center for Excellence in Nanomedicine and Engineering).

Chapter 1, in full, is a reformatted reprint of the material as it appears in Journal of Controlled Release 2015. Nguyen Huu, Viet Anh; Luo, Jing; Zhu, Jie; Zhu, Jing; Patel, Sherrina; Boone, Alexander; Mahmoud, Enas; McFearin, Cathryn; Olejniczak, Jason; de Gracia Lux, Caroline; Lux, Jacques; Fomina, Nadezda; Huynh, Michelle; Zhang, Kang; Almutairi, Adah., Elsevier, 2015. The dissertation/thesis author was the primary investigator and author of this paper.

1.8 Supporting Information

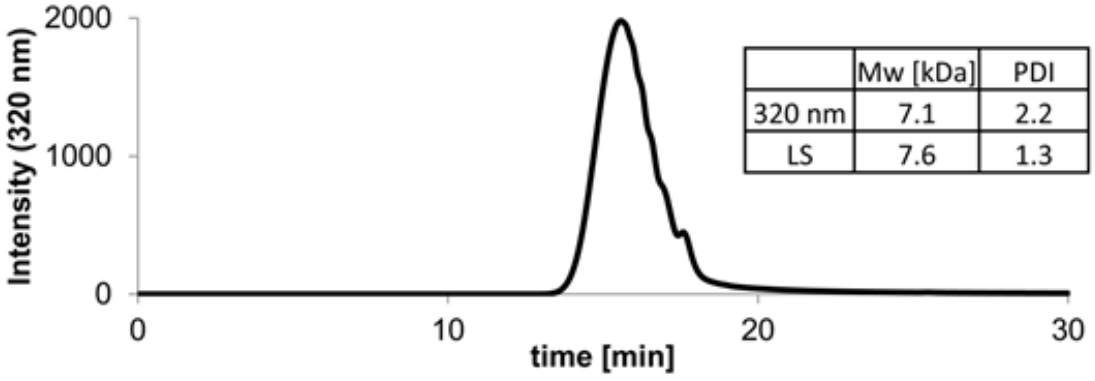

Figure 1.6: Gel permeation chromatography of UVSP polymer. Inset: calculated molecular weights from UV (320 nm) and light scattering (LS) detectors.

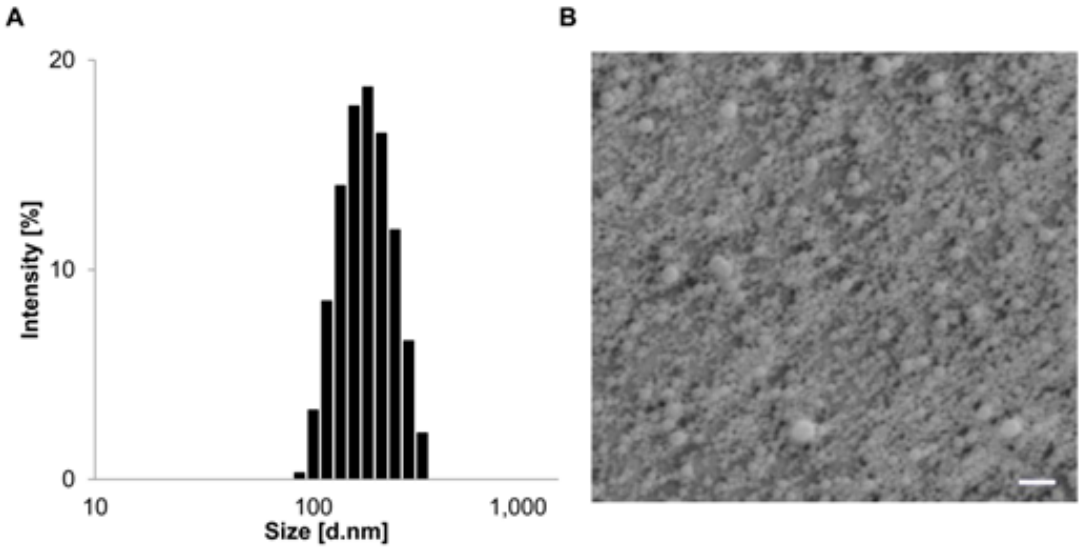

Figure 1.7: Nanoparticles formed by emulsion-evaporation are monodisperse. A, Size distribution of nanoparticles by dynamic light scattering (DLS). B, SEM of drop-casted nanoparticles.

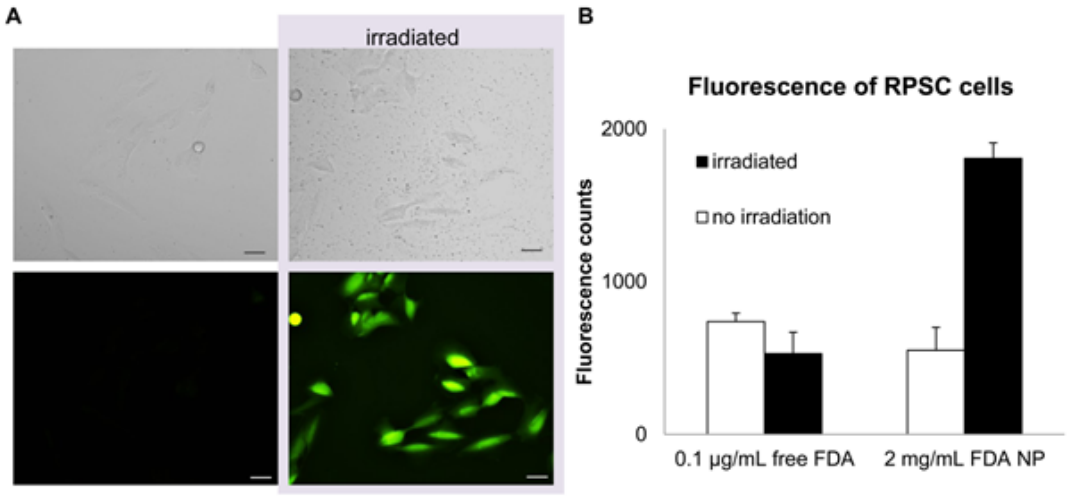

Figure 1.8: UV light triggers release of encapsulated molecules in cultured RPSC cells. A, RPSC cells incubated with FDA-encapsulating NPs were treated with 5 min of 10 mW/cm^2 UV light. B, Quantification of fluorescence (n = 6, p $<$ 0.001 for irradiated vs. non-irradiated cells).

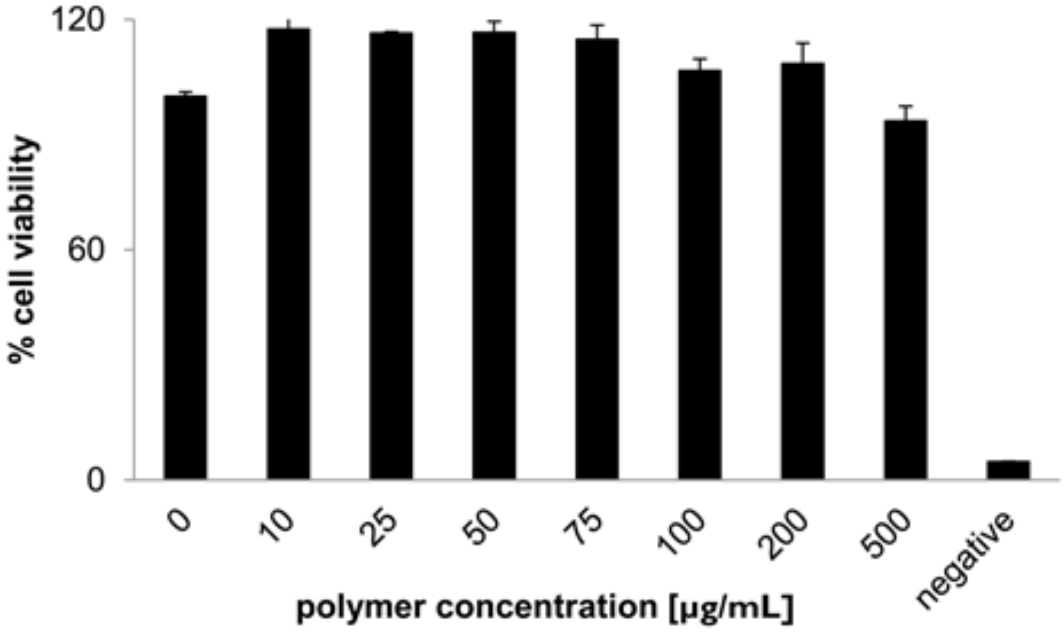

Figure 1.9: UVSP is well-tolerated by Raw 264.7 mouse macrophage cells. MTT assay at 24 h of incubation (n = 3).

Table 1.1: qRT-PCR primers

Primer	sequence (5' − > 3')
rGAPDH-F	TAAAGGGCATCCTGGGCTACACT
rGAPDH-R	TTACTCCTTGGAGGCCATGTAGG
rIL-1β-F	CACCTCTCAAGCAGAGCACAG
rIL-1β-R	GGGTTCCATGGTGAAGTCAAC
rTNFα-F	CCAGGAGAAAGTCAGCCTCCT
rTNFα-R	TCATACCAGGGCTTGAGCTCA

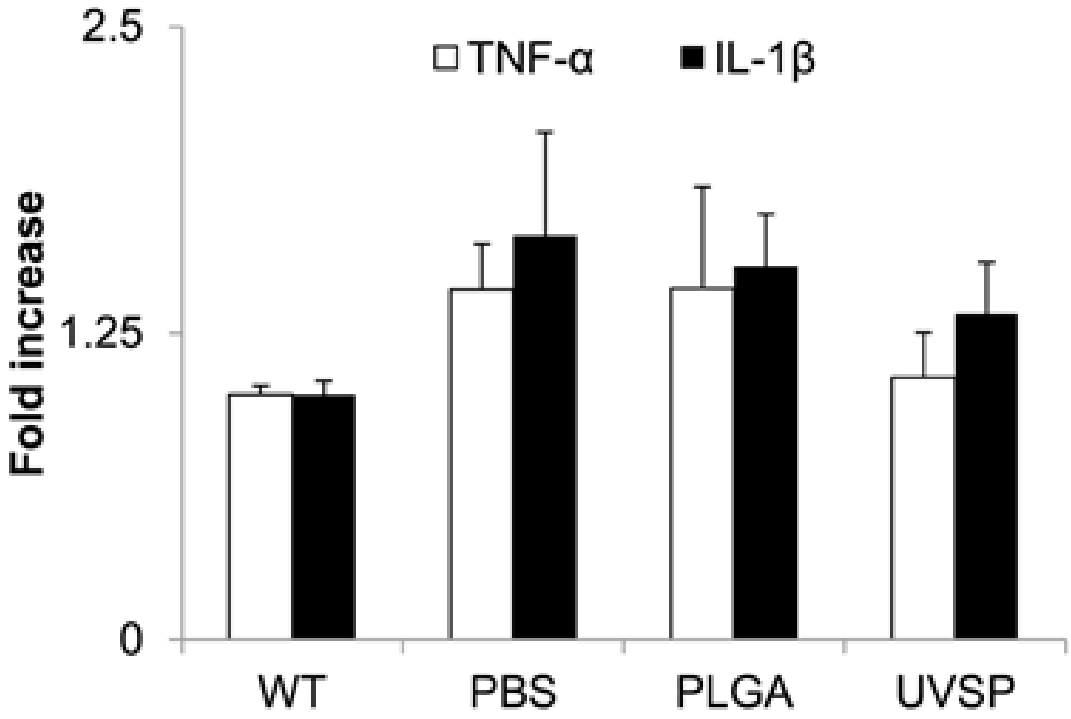

Figure 1.10: Exposure to UVSP does not affect expression of inflammatory cytokines in the retina. qRT-PCR 1 week after injection

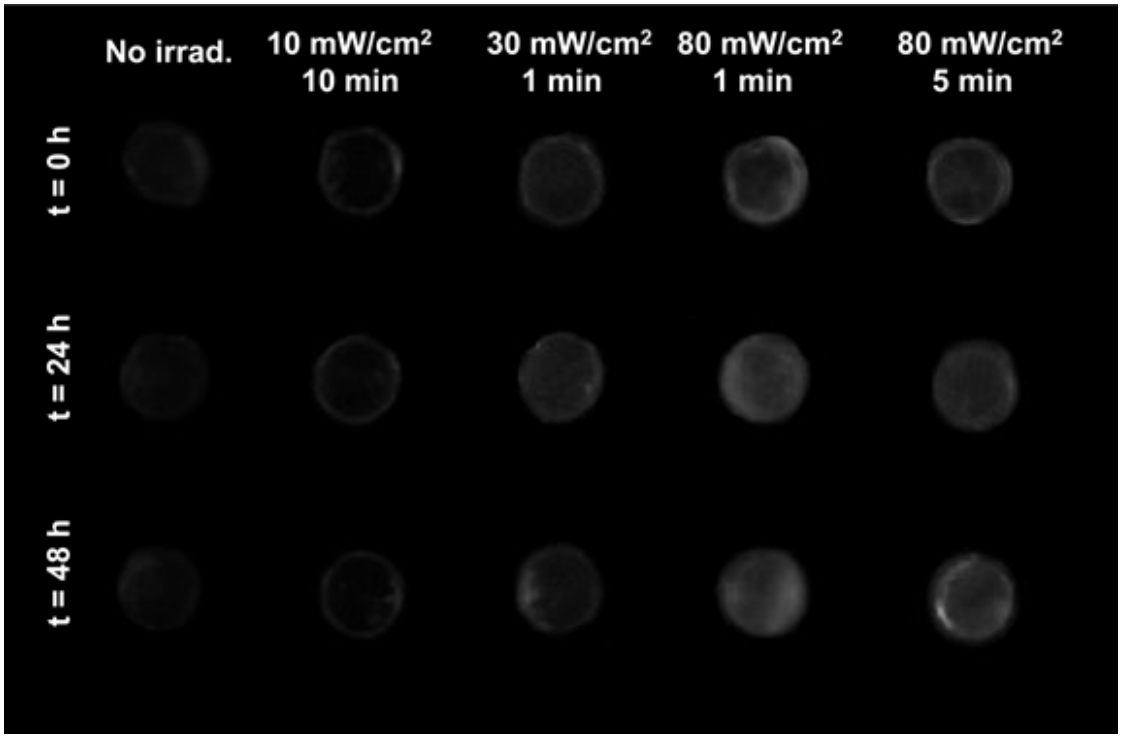

Figure 1.11: Identification of benign irradiation conditions. Lenses exposed to varying intensities of UV were imaged using a gel imager (VersaDoc, Bio-Rad Laboratories) at three time points (the above image is a composite). 10 mW/cm^2 causes no clouding and was thus used for later in vivo studies.

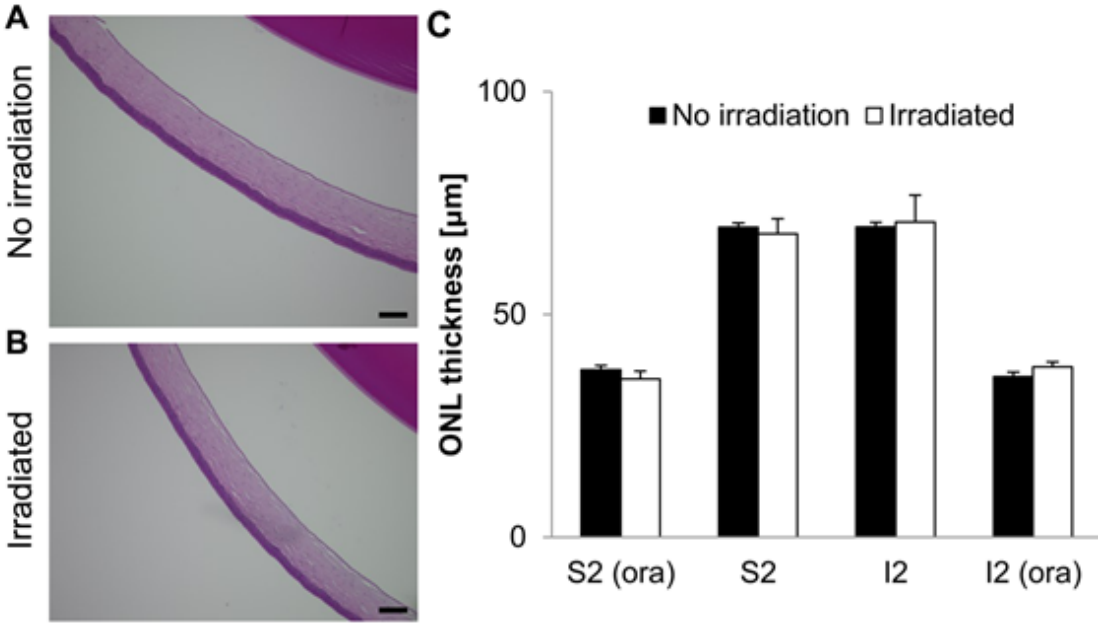

Figure 1.12: Irradiation of the eye does not cause long-term ocular tissue damage. A-B, H&E stained cornea (light pink) and lens (dark pink) tissue slices 8 weeks after procedure (A - non-irradiated eye; B - irradiated eye). Scale, 100 μm. C, Quantification of outer nuclear layer (ONL) thickness from histology sections (S2 - superior quadrant, I2 - inferior quadrant, ora - vicinity of ora serrata).

1.9 References

(1) K. Zhang, L. Zhang and R. N. Weinreb, *Nat Rev Drug Discov*, 2012, **11**, 541–59.

(2) D. H. Nguyen, J. Luo, K. Zhang and M. Zhang, *Discov Med*, 2013, **15**, 343–8.

(3) R. Herrero-Vanrell and M. F. Refojo, *Adv Drug Deliv Rev*, 2001, **52**, 5–16.

(4) J. L. Bourges, C. Bloquel, A. Thomas, F. Froussart, A. Bochot, F. Azan, R. Gurny, D. BenEzra and F. Behar-Cohen, *Adv Drug Deliv Rev*, 2006, **58**, 1182–202.

(5) Y. Ali and K. Lehmussaari, *Adv Drug Deliv Rev*, 2006, **58**, 1258–68.

(6) M. Honda, T. Asai, T. Umemoto, Y. Araki, N. Oku and M. Tanaka, *Archives of Ophthalmology*, 2011, **129**, 317–321.

(7) J.-l. Wang, Y.-l. Liu, Y. Li, W.-b. Dai, Z.-m. Guo, Z.-h. Wang and Q. Zhang, *Invest Ophthalmol Vis Sci*, 2012, **53**, 7348–7357.

(8) A. C. Amrite, S. P. Ayalasomayajula, N. P. Cheruvu and U. B. Kompella, *Invest Ophthalmol Vis Sci*, 2006, **47**, 1149–60.

(9) F. Paganelli, J. A. Cardillo, A. R. Dare, J. Melo, L. A., D. R. Lucena, J. Silva, A. A., A. G. Oliveira, A. C. Pizzolitto, D. Lavinsky, M. Skaf, A. A. Souza-Filho, A. L. Hofling-Lima, Q. D. Nguyen, B. D. Kuppermann, R. Herrero-Vanrell, J. Belfort, R., P. Brazilian Ocular and G. Pharmaceutical Technology Research, *Expert Opin Drug Deliv*, 2010, **7**, 955–65.

(10) A. C. Amrite and U. B. Kompella, *J Pharm Pharmacol*, 2005, **57**, 1555–63.

(11) T. Iwase, J. Fu, T. Yoshida, D. Muramatsu, A. Miki, N. Hashida, L. Lu, B. Oveson, R. Lima e Silva, C. Seidel, M. Yang, S. Connelly, J. Shen, B. Han, M. Wu, G. L. Semenza, J. Hanes and P. A. Campochiaro, *J Control Release*, 2013, **172**, 625–33.

(12) N. Fomina, J. Sankaranarayanan and A. Almutairi, *Adv Drug Deliv Rev*, 2012, **64**, 1005–1020.

(13) B. P. Timko and D. S. Kohane, *Clin Ther*, 2012, **34**, S25–35.

(14) S. Joshi-Barr, C. de Gracia Lux, E. Mahmoud and A. Almutairi, *Antioxid Redox Signal*, 2014, **21**, 730–54.

(15) J. Kost and R. Langer, *Adv Drug Deliv Rev*, 2012, **64**, 327–341.

(16) N. Fomina, C. McFearin, M. Sermsakdi, O. Edigin and A. Almutairi, *J Am Chem Soc*, 2010, **132**, 9540–2.

(17) A. Ringvold, M. Davanger and E. G. Olsen, *Acta Ophthalmologica*, 1982, **60**, 41–53.

(18) S. Sampath, L. A. McLean, C. Buono, P. Moulin, A. Wolf, S. D. Chibout, F. Pognan, S. Busch, N. Shangari, E. Cruz, M. Gurnani, P. Patel and A. Reising, *Toxicol Sci*, 2012, **126**, 128–39.

(19) M. D. Aleo, C. M. Doshna and K. A. Navetta, *J Pharmacol Exp Ther*, 2005, **312**, 1027–33.

(20) J. Luo, P. Baranov, S. Patel, H. Ouyang, J. Quach, F. Wu, A. Qiu, H. Luo, C. Hicks, J. Zeng, J. Zhu, J. Lu, N. Sfeir, C. Wen, M. Zhang, V. Reade, S. Patel, J. Sinden, X. Sun, P. Shaw, M. Young and K. Zhang, *J Biol Chem*, 2014, **289**, 6362–71.

(21) R. Berti, A. J. Williams, J. R. Moffett, S. L. Hale, L. C. Velarde, P. J. Elliott, C. P. Yao, J. R. Dave and F. C. Tortella, *Journal of Cerebral Blood Flow and Metabolism*, 2002, **22**, 1068–1079.

(22) K. Kobayashi, H. Utsumi, M. Okada, T. Sakairi, I. Ikeda, M. Kusakabe and S. Takagi, *Journal of Veterinary Medical Science*, 2003, **65**, 917–919.

(23) F. Hilberg, G. J. Roth, M. Krssak, S. Kautschitsch, W. Sommergruber, U. Tontsch-Grunt, P. Garin-Chesa, G. Bader, A. Zoephel, J. Quant, A. Heckel and W. J. Rettig, *Cancer Res*, 2008, **68**, 4774–82.

(24) J. M. Clarke, M. R. Gillings, N. Altavilla and A. J. Beattie, *J Microbiol Methods*, 2001, **46**, 261–7.

(25) A. R. Young, *Prog Biophys Mol Biol*, 2006, **92**, 80–5.

(26) G. Wollensak, E. Sporl and T. Seiler, *Ophthalmologe*, 2003, **100**, 44–9.

(27) J. Zavala, G. R. L. Jaime, C. A. R. Barrientos and J. Valdez-Garcia, *Eye (Lond)*, 2013, **27**, 579–588.

(28) G. Wollensak, *Curr Opin Ophthalmol*, 2006, **17**, 356–360.

(29) G. Wollensak, E. Spoerl, M. Wilsch and T. Seiler, *Journal of Cataract and Refractive Surgery*, 2003, **29**, 1786–1790.

(30) D. G. Pitts, A. P. Cullen and P. D. Hacker, *American Journal of Optometry and Physiological Optics*, 1977, **54**, 542–549.

Chapter 2

Light-Triggered Chemical Amplification to Accelerate Degradation and Release from Polymeric Particles

2.1 Abstract

Herein, we describe a means of chemical amplification to accelerate triggered degradation of a polymer and particles composed thereof. We designed a light-degradable random copolymer containing both carboxylic acids masked by photolabile groups and ketals. Cleavage of the photocages allows the unmasked acidic groups in the polymer backbone to accelerate ketal hydrolysis, through intramolecular acid catalysis, even at neutral pH. Whereas triggered release using most light-degradable polymers requires lengthy irradiation times that may damage biological systems, release of cargo from nanoparticles composed of this polymer requires only a few minutes of low-power irradiation.

2.2 Introduction

On-demand or environmentally triggered disassembly of polymers is a widely sought-after goal, as such materials would be tremendously useful in a broad range of industries, including healthcare, cosmetics, agriculture, and electronics.[1,2] Despite this, few synthetic polymers degrade with high sensitivity in response to specific stimuli. Most current degradable materials are unresponsive to the often subtle changes found in biological systems or, in the case of photodegradable polymers, require long, intense irradiation that may not be biologically compatible. This limitation results from the fact that most of these materials convert each signaling event to only one chemical change, such as a single break in the polymer backbone[3–5] or a change in hydrophobicity of one monomeric unit.[6,7]

Self-immolative polymers can amplify responses to stimuli via head-to-tail depolymerization and have thus been developed to circumvent this limitation.[8–10] However, most of these materials rely on slow intramolecular rearrangements to degrade their backbone,[11–15] ultimately slowing down depolymerization. Alternatively, self-immolative polymers containing more labile bonds have also been developed,[16,17] but these bonds are likely not resilient enough to escape degradation in a physiological setting, even in the absence of the intended stimulus. Here, we have designed a polymer in which photocleavage unmasks acidic groups in the polymer backbone that then provide intramolecular assistance to ketal hydroly-

sis[18] so that minimal signal, in this case brief, low-power UV irradiation, triggers significant polymer degradation. This strategy should allow faster release with less irradiation than existing light-degradable polymers.[19–21]

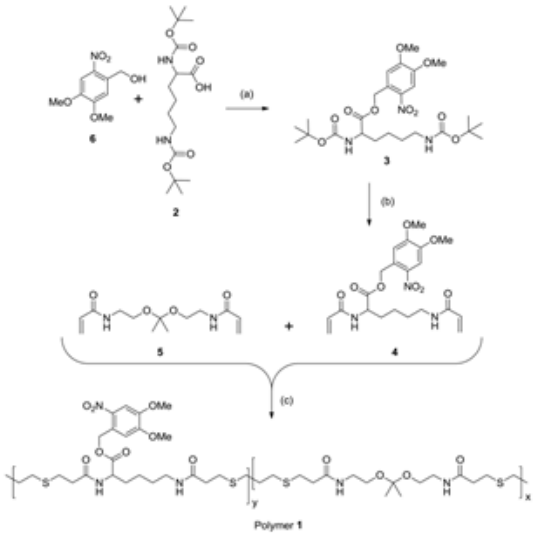

Figure 2.1: Synthesis of polymer **1**. a) EDC, DMAP, DCM, (compound **2** used as the dicylohexylamine salt), 52%; b) i) TFA, DCM ii) acryloyl chloride, NEt_3, DCM, 0 °C, 49%; c) 5, 1,3-propanedithiol, NEt_3, DMSO, 42%.

Our design was inspired by the extensive literature on rates and mechanisms of ketal hydrolysis,[21,22] degradation rates of polyketals,[22] and disassembly of ketal-modified polymeric particles.[23–27] Ketal hydrolysis rates are known to vary with hydrophilicity,[28,29] and water accessibility affects the kinetics of disassembly and degradation of particle assemblies containing ketals either within the backbone[30,31] or as pendant groups.[32] These findings inspired hydrophobic-hydrophilic switching mechanisms to exert further control over particle disassembly and/or degradation.[30] More recently, our group applied intramolecular assistance of acids, to accelerate the degradation of polyketals,[2-33] the degradation occurred much

more rapidly (in hours) than in comparable hydrophilic polymers (in days)[22] at the same buffered pH but containing no intramolecular acids. Here we employ the same concept to a light-degradable particle. We incorporate photoacids as pendant groups into a polyketal backbone, from which we formulate particles. Cleavage of the photocage upon UV irradiation unmasks a carboxylic acid. This both releases acid groups in the vicinity of the backbone ketals (not necessarily adjacent along the backbone; polymer entanglement in a nanoparticle would juxtapose groups that would be distant from one another in dilute solution), and makes the polymer more hydrophilic, both of which facilitate ketal hydrolysis. We then formulated the polymer into nanoparticles to examine whether this strategy allows nanoparticle disassembly and cargo release in response to brief, low power irradiation.

2.3 Experimental Data

To synthesize a polymer containing both ketal moieties and protected acid functions, we prepared two monomers that could then be copolymerized (Figure 2.1). The ketal monomer **5** was synthesized using established methods.[22] To prepare the monomer bearing a protected acid, the di-Boc derivative of lysine **2** was esterified by EDC coupling with 4,5-dimethoxy-2-nitrobenzyl alcohol **6** to form lysine derivative **3**. *Ortho*-nitrobenzyl alcohol **6** was chosen as a photolabile protecting group due to its commercial availability, relatively high tolerance to subsequent reactions, and its well-characterized photochemistry.[33,34] Though the

low tissue penetration of UV light required for photolysis of this protecting group limits biological relevance, here we are interested in demonstrating the concept of triggered chemically amplified degradation of a polymer backbone and showing its utility in the degradation of polymeric particles. TFA-mediated deprotection of the Boc groups of **3** and subsequent acrylation using acryloyl chloride afforded **4** in 49% yield over two steps. The two monomers in equal proportions were then copolymerized using a Michael addition with 1,3-propanedithiol to yield polymer **1** with a molecular weight of 12,700 Da and polydispersity index (PDI) of 1.98 as characterized by gel permeation chromatography (GPC) relative to poly(methyl methacrylate) standards (Figure 2.6) with 42% yield. The monomers were incorporated with equal efficiency as seen by ^{1}H NMR spectroscopy (Figure 2.7 A), yielding a polymer with a 1:1 ratio of hydrolyzable ketals to protected acids. Michael addition proved to be an ideal means of polymerization due to its relatively mild conditions, a necessity to avoid degradation of the ketal.

We monitored polymer degradation using ^{1}H NMR spectroscopy by following hydrolysis of the ketal (degradation scheme, Figure 2.2a). Polymer **1** was dissolved in a 9:1 mixture of deuterated DMSO and deuterated phosphate buffer at pH 7.4 and phosphate solution at pH 5 and irradiated for times ranging from 0 to 20 minutes with UV light (1.35 mW/cm^2). Though the high proportion of organic solvent slows ketal hydrolysis by orders of magnitude,[35,36] DMSO was required to solubilize the polymer prior to irradiation. Following irradiation substantial

amounts of the light-sensitive protecting groups still appeared intact; by ^{1}H NMR only half the acids were exposed even after 20 min of irradiation (Figure 2.8). The samples were then monitored by ^{1}H NMR spectroscopy at various time points throughout incubation at 37 °C. Although the ketal peak diminished and the acetone peak grew (Figure 2c), the percentage of hydrolyzed ketal over time could not be accurately determined because of signal overlap. Ketal hydrolysis was instead followed by conversion of the methylene protons (Figure 2a, protons A) vicinal to the ketal into protons vicinal to an alcohol. The initial rate of ketal hydrolysis was determined for each condition (Figure 2b).

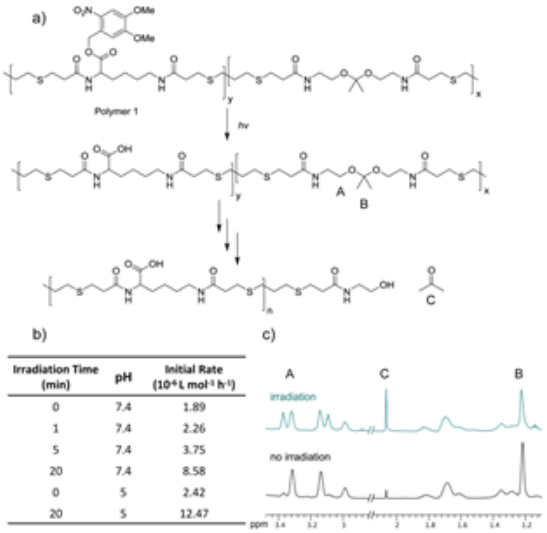

Irradiation Time (min)	pH	Initial Rate (10^{-6} L mol^{-1} h^{-1})
0	7.4	1.89
1	7.4	2.26
5	7.4	3.75
20	7.4	8.58
0	5	2.42
20	5	12.47

Figure 2.2: a) Degradation scheme of polymer **1**. b) Initial rate of ketal hydrolysis at varying pH and with varying amounts of irradiation. c) ^{1}H NMR spectra of polymer samples after 23 days at pH 7.4 with 20 min UV irradiation (top teal) or without irradiation (bottom black). Rates and ^{1}H NMR spectra were obtained in a 9:1 mixture of DMSO to aqueous solution.

The initial rate of hydrolysis at pH 7.4 increased with longer irradiation times, becoming four times faster after 20 minutes of irradiation than with no

irradiation. Even irradiation for just five minutes led to a doubling of the initial hydrolysis rate. Importantly, irradiation for only one min increased the ketal hydrolysis rates at pH 7.4 to those of pH 5.0 without irradiation. Finally, irradiation for only 5 min caused the pH 7.4 degradation kinetics to be 55% faster than the pH 5.0 degradation kinetics without irradiation. Thus, intramolecular acid-assisted hydrolysis overcomes the requirement of acidic pH for polyketal degradation. The fastest degradation occurred in the sample irradiated for 20 min at pH 5. Comparable polymers containing the same ketal moiety have a half-life of roughly 1 h at pH 5 in solutions with a smaller proportion of organic solvents, suggesting that this polymer would degrade even more rapidly in biological settings.[22]

Polymer degradation was also assessed by GPC (Figure 2.8). While a shift towards longer retention times would normally indicate a decrease in molecular weight, the immediate shift observed upon irradiation of samples of polymer **1** is too rapid to indicate degradation. Instead, it likely results from a change in hydrophilicity caused by release of acids, increasing interaction with the column material. Shifts towards longer retention times in subsequent time points do support polymer degradation.

To examine whether this degradation strategy allows rapid light-triggered release, we formulated nanoparticles of polymer **1** by single emulsion encapsulating the model payloads fluorescein diacetate (FDA) or Nile red (size = 192.7 nm, PDI = 0.06). Particle degradation was assessed following irradiation and subsequent

incubation at 37 °C by dynamic light scattering (DLS) with fixed attenuation. Upon UV irradiation, count rate decreased substantially and the PDI increased within 4 h, indicating substantial changes in particle morphology and possible degradation. Particles remained relatively stable in the absence of irradiation. After 48 h, the count rate of irradiated particles was too low to be measured. The underlying morphological changes were examined by transmission electron microscopy (TEM) (Figure 2.3c). After irradiation, subsequent incubation for 4 h, and then drying at room temperature, particles appeared to disintegrate (Figure 2.3d).

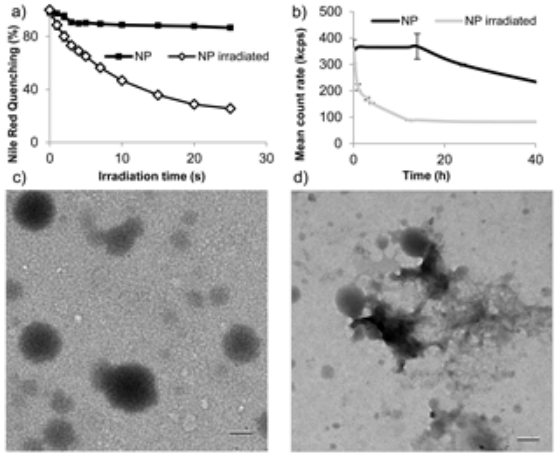

Figure 2.3: a) Quenching of fluorescence of Nile red encapsulated in nanoparticles of polymer 1 following irradiation with UV light.b) count rate of nanoparticles after irradiation 5 min (35 mW/cm^2, λ = 320-480 nm) by DLS. c) representative TEM micrographs of particles prior to irradiation and d) post-irradiation 5 min (35 mW/cm^2, λ = 320-480 nm) and incubation at 37 °C for 4 h (scale bars = 200 nm).

We then examined light-triggered release by measuring fluorescence quenching of nanoparticle-encapsulated Nile red. Nile red is fluorescent in the hydrophobic

environment of nanoparticles, but its fluorescence is quenched in aqueous environments. Rapid fluorescence quenching was observed upon irradiation of particles suspended in pH 8.0 Tris buffer (Figure 2.3a). This quenching is indicative of substantial morphological changes, allowing Nile red escape or entry of water into the particles. To confirm that payload is released from the nanoparticles, Raw 264.7 mouse macrophage cells were incubated with particles containing FDA and irradiated for 5 min with UV light (10 mW/cm^2) (Figure 4b). This is a comparable power and shorter irradiation time than has been used with materials incorporating this photocage in cellular experiments,38,39 possibly suggesting high light sensitivity of the particles and tolerance by cells of this level of irradiation, differences in formulation prevent direct comparisons. FDA is a non-fluorescent molecule hydrolyzed by intracellular esterases to form the fluorescent compound fluorescein; only released FDA would encounter these esterases. UV irradiation led to high intensity cellular fluorescence, while non-irradiated cells did not fluoresce appreciably (Figure 2.4a). This result shows that nanoparticles composed of polymer **1** release cargo upon irradiation in the presence of cells without changing cellular morphology under irradiation conditions that have minimal impact on cellular viability (Figure 2.11).

Finally, we assessed cellular compatibility by MTT assay in Raw 264.7 mouse macrophage cells after treatment with empty nanoparticles irradiated prior to treatment (Figure 5), irradiated after incubation with cells (Figure S6) not

irradiated and polymer **1** (Figure 2.10). Neither nanoparticles nor polymer significantly impacted mitochondrial activity up to 200 μg/mL, suggesting this material has potential as a drug delivery vehicle. Nanoparticle degradation products also appear to have less effect on cellular viability than intact nanoparticles.

2.4 Conclusions

Herein we have demonstrated that unmasking of acids in the polymer backbone to accelerate the hydrolysis of ketals at neutral pH is a viable strategy to accelerate polymer and particle degradation. This strategy allows significant polymer degradation upon low-power irradiation. Rapid light-triggered release from polymer **1** nanoparticles demonstrates the potential of this strategy for triggered degradation in general; other chemical groups could be employed to confer responsiveness to other stimuli. Alternative photocages that exploit the tunable sensitivity of this backbone are currently being explored.

2.5 Acknowledgements

The authors gratefully acknowledge the King Abdulaziz City for Science and Technology (through the KACST-UCSD Center for Excellence in Nanomedicine and Engineering) and the NIH New Innovator Award (DP2OD006499) for funding. NMR spectra were acquired at the UCSD Skaggs School of Pharmacy and Pharmaceutical Sciences NMR facility. High-resolution mass spectroscopic data was

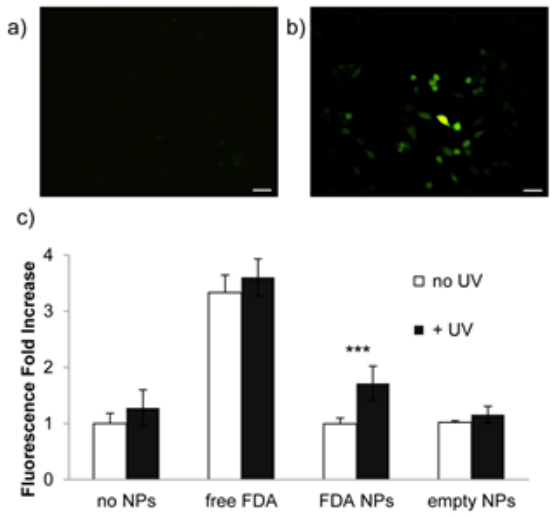

Figure 2.4: Raw 264.7 mouse macrophage cells incubated (30 min, 37 °C) with nanoparticles a) in the absence of irradiation and b) irradiated for 5 min (10 mW/cm^2). Scale bars = 30 μm. c) Increase in FDA fluorescence; $p < 0.001$.

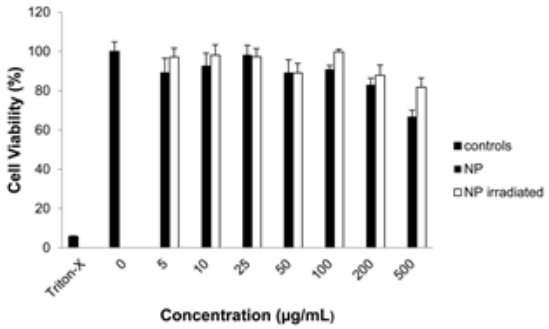

Figure 2.5: Nanoparticles of polymer **1** are well-tolerated by Raw 264.7 macrophages. MTT assay following 24 h incubation with nanoparticles, either intact or pre-irradiated for 5 min with UV light (10 mW/cm^2).

measured at the UCSD Biomolecular and Proteomics Mass Spectrometry Facility. The authors would also like to thank Jessica Moore, Minnie Chan, Amy Moore, Carl-Johan Carling and Brendan Duggan for their insight and technical expertise.

Chapter 2, in full, is a reformatted reprint of the material as it appears in Chemical Science 2016. Olejniczak, Jason; Nguyen Huu, Viet Anh; Lux, Jacques; Grossman, Madeleine; He, Sha; Almutairi, Adah., ACS Press 2015. The dissertation/thesis author was the co-author of this paper.

2.6 Supporting Information

2.6.1 General methods and instrumentation

All chemicals and solvents were purchased from Sigma-Aldrich and used as received unless specified. Anhydrous solvents were acquired from a solvent purification system (LC Technology Solutions Inc., SP-1). Silica gel flash column chromatography was performed using an automated CombiFlash Rf 200 system. Polymer **1** was analyzed by GPC using a Agilent 1100 Series HPLC system equipped with RI, Agilent 1260 Light Scattering and PDA detectors and a Waters Styragel HR 2 size-exclusion 22 column with 0.1% LiBr/DMF as eluent and flow rate of 1 mL/min at 37 °C. Monodisperse poly(methylmethacrylate) (PMMA) standards were used to determine the molecular weight and PDI of polymer **1**. ^{1}H NMR and ^{13}C NMR spectra were acquired using a Varian spectrometer working at 600 MHz and 150 MHz respectively. Chemical shifts (δ) are reported in ppm rela-

tive to TMS, and coupling constants (J) are reported in hertz. High-resolution mass spectra were acquired using an Agilent 6230 ESI-TOFMS in positive ion mode. Irradiation with UV light was done with a Luzchem LZC-ORG photoreactor equipped with 8 UV-A lamps with a power of 1.35 mW/cm^2 and a 10 mW/cm^2, λ_{ex} = 320-480 nm, OmniCure S2000 Curing System. Particles were formulated using a Qsonica Sonicator 4000 and purifiedby tangential flow filtration Millipore Pellicon XL, 500 kDa. Particles were characterized by DLS, Malvern Instruments Nanosizer, scanning electron microscopy (SEM, Agilent 8500 FE-SEM), and transmission electron microscopy (TEM, Tecnai FEI Spirit). Fluorescence was measured using a Horiba Jobin Yvon FL-1000 fluorimeter and in cells a Molecular Devices SpectraMax M5 plate reader. Fluorescence microscopy images were acquired with a Nikon TS100F.

2.6.2 Abbreviations

EDC = 1-ethyl-3-(3-dimethylaminopropyl)carbodiimide, DMSO = dimethyl sulfoxide, DMAP = 4-dimethylaminopyridine, TFA = trifluoroacetic acid, NEt_3 = triethylamine, FDA = fluorescein diacetate, DMF = dimethylformamide, TEM = transmission electron microscopy, PDI = polydispersity index, UV = ultraviolet, DLS = dynamic light scattering, GPC = gel permeation chromatography, HPLC = high pressure liquid chromatography, RI = refractive index, PDA = photodiode array.

2.6.3 Synthesis of polymer 1

Compound 3. Compound **6** (1.00 g, 4.7 mmol), compound **2**. dicyclohexylamine (3.25 g, 6.2 mmol) and DMAP (1.15 g, 9.38 mmol) were dissolved in DCM (48 mL). EDC (1.46 g, 9.4 mmol) was added to the solution dropwise and the mixture was allowed to react for 14 hrs. The reaction mixture was diluted with DCM and extracted 3 times with 1 M HCl. The organic layer was dried over $MgSO_4$ and concentrated. The resulting yellow oil was purified by silica column (3:7 Ethyl Acetate/Hexane) to yield compound 3 as a yellow solid (1.32 g, 52 %).

HRMS: composition: C_{25} H_{39} N_3 O_{10}; measured mass 564.2527; theoretical mass 564.2528.

^{1}H NMR (600 MHz, CDCl3) δ 7.70 (s, 1H), 7.04 (s, 1H), 5.60 (d, J = 14.9 Hz, 1H), 5.51 (d, J = 14.9 Hz, 1H), 5.21-5.12 (m, 1H), 4.62 (bs, 1H), 4.36-4.28 (m, 1H), 4.00 (s, 3H), 3.94 (s, 3H), 3.15-3.01 (m, 2H), 1.94 âĂŞ 1.79 (m, 2H), 1.77 âĂŞ 1.64 (m, 2H), 1.53-1.44 (m, 2H), 1.43 (s, 9H), 1.40 (s, 9H). 13C NMR (151 MHz, CDCl3) δ 172.7, 156.3, 155.76, 153.9, 148.4, 139.8, 127.1, 110.5, 108.4, 80.1, 79.3, 64.0, 56.8, 56.5, 53.8, 40.0, 34.0, 29.8, 28.5, 28.4, 22.6.

Compound 4. Compound **3** (2.071 g, 3.82 mmol) was dissolved in DCM (5 mL) and TFA (5 mL) and stirred for 1 hr. The reaction mixture was concentrated. The resulting yellow oil was dissolved in DCM and concentrated 3 more times. The yellow oil was then dissolved in DCM (18.5 mL) and DMF (18.5 mL) and chilled to 0 °C. NEt_3 (3.19 mL, 22.9 mmol) was dripped into the solution slowly. Acryloyl

chloride (0.68 mL, 8.41 mmol) was dripped into the reaction mixture over a period of 10 min. The reaction was quenched after 1 hr by addition of 0.05 M HCl. The mixture was extracted 3 times with DCM. The combined organic was dried over $MgSO_4$ and concentrated. The resulting yellow oil was purified by silica column (3% MeOH in DCM) to yield compound **4** as a yellow solid (0.837 g, 48.5 %).

HRMS: composition: C_{21} H_{27} N_3 O_8; measured mass 472.1692; theoretical mass 472.1690.

^{1}H NMR (600 MHz, DMSO) δ 8.58 (d, J = 7.1 Hz, 1H), 8.07 (t, J = 5.5 Hz, 1H), 7.71 (s, 1H), 7.19 (s, 1H), 6.32 (dd, J = 17.1, 10.2 Hz, 1H), 6.18 (dd, J = 17.1, 10.2 Hz, 1H), 6.11 (dd, J = 17.1, 2.0 Hz, 1H), 6.05 (dd, J = 17.1, 2.2 Hz, 1H), 5.65 (dd, J = 10.2, 2.0 Hz, 1H), 5.55 (dd, J = 10.2, 2.2 Hz, 1H), 5.48 âĂŞ 5.41 (m, 2H), 4.42 âĂŞ 4.34 (m, 1H), 3.93 (s, 3H), 3.87 (s, 3H), 3.16 âĂŞ 3.06 (m, 2H), 1.83 âĂŞ 1.75 (m, 1H), 1.74-1.65 (m, 1H), 1.51 âĂŞ 1.40 (m, 2H), 1.39-1.30 (m, 2H).

^{13}C NMR (151 MHz, DMSO) δ 171.8, 164.9, 164.4, 153.4 147.86, 139.34, 131.82, 130.9, 126.4, 124.7, 110.7, 108.2, 99.5, 63.0, 56.3, 56.1, 52.3, 38.1, 30.3, 28.6, 22.8.

Polymer 1. Compound **4** (150 mg, 0.33 mmol) and Compound **5** (90 mg, 0.33 mmol) were dissolved in DMSO (0.9 mL). Triethylamine (0.28 mL, 2.00 mmol) then 1,3-propanedithiol (72 mg, 0.67 mmol) were added to the solution dropwise. The reaction was stirred at room temperature for 140 hrs. The reaction mixture

was quenched by crashing into cold ether. The polymer was further purified by dissolving in DCM and crashing into cold ether three times to yield yellow polymer (131 mg, 42 %). Molecular weight of 13900 Da, PDI of 1.71 (characterized by GPC relative to poly(methyl methacrylate) standards).

^{1}H NMR (600 MHz, d^6 DMSO) δ 8.39-8.34 (m 1H), 7.97-7.90 (m, 2H), 7.85 (s, 1H), 7.70 (s, 1H), 7.19 (s, 1H), 5.42 (s, 2H), 4.29 (m, 1H), 3.94 (s, 3H), 3.866 (s, 3H),3.40-3.30 (m, 4H), 3.19-3.13 (m, 4H), 3.05-2.97 (m, 2H), 2.81-2.61 (m, 8H), 2.61-2.51 (m, 8H), 2.47-2.27 (m, 8H), 1.91-1.60 (m, 6H), 1.46-1.29 (m, 4H), 1.28-1.23 (s,6H).

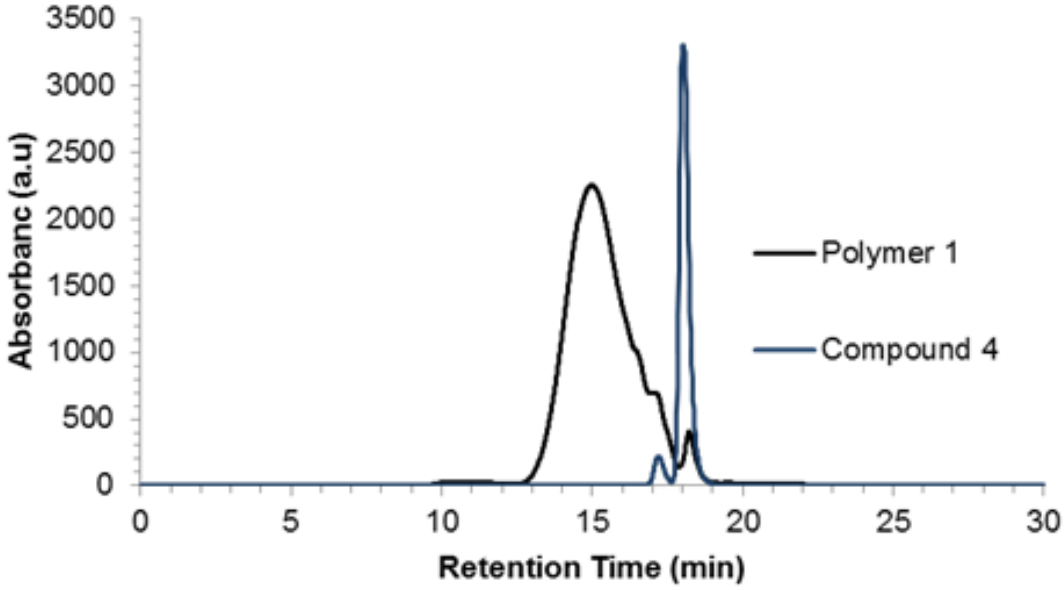

Figure 2.6: GPC chromatogram of polymer **1** and compound **4**.

2.6.4 Degradation of polymer 1

Degradation of polymer **1** followed ^{1}HNMR. A concentrated solution of polymer **1** (12.5 mg/ mL) was prepared in d_6-DMSO. The DMSO stock was divided and an appropriate amount of deuterated sodium phosphate buffer at pH 7.4 (0.1M) and sodium phosphate solution at pH 5 were added to make 9:1 solutions of d_6-DMSO:PBS. The solution was irradiated for 1 to 20 min in a 1.7 mm Bruker NMR tube in a Luzchem photoreactor. The samples were then incubated at 37 °C for the specified times. Spectra were taken on a 600 MHz Bruker spectrometer after the prescribed incubation times.

Degradation of polymer **1** followed GPC. Polymer **1** was dissolved in a mixture of acetonitrile and PBS 90:10. Two solutions were prepared with pH 7.4 (0.1M) PBS. One of the samples with PBS pH 7.4 was irradiated in a Luzchem photoreactor for 20 min. The samples were incubated at 37 °C for the 0, 24, 115, and 336 hrs. At the given times the samples were concentrated at 30 oC, dissolved in DMF with 0.01% LiBr, and analyzed by gel permeation chromatography monitoring at 320 nm.

2.6.5 Particle formulation and characterization

Particle formulation. Polymer **1** (10 mg) was dissolved in DCM (270 μL), and combined with fluorescein diacetate (FDA, 2mg) in DMSO (30 μL), or Nile Red (NR, 1 mg) in DCM (30 μL). The resulting solution was added to sterile-filtered

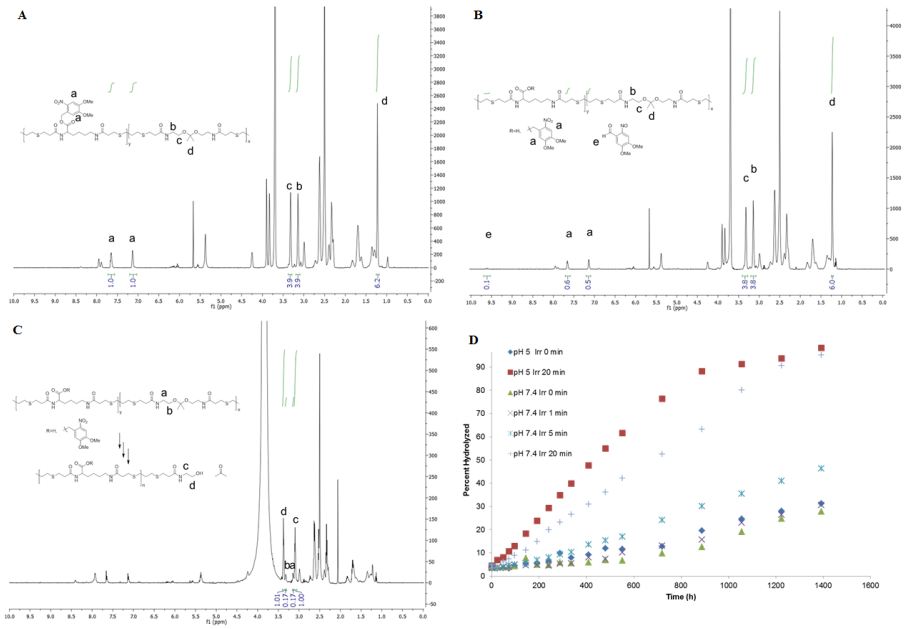

Figure 2.7: Degradation of polymer **1** followed ^{1}HNMR. (A-B), ^{1}HNMR spectra of polymer **1** (A) before, (B) following 20 min irradiation (1.35 mW/cm^2), or (C) following 20 min irradiation and 1224 h incubation in 9:1 solutions of d_6-DMSO:deuterated PBS pH 7.4. (D) Percent hydrolysis of the polymer following the indicated periods of irradiation and incubation.

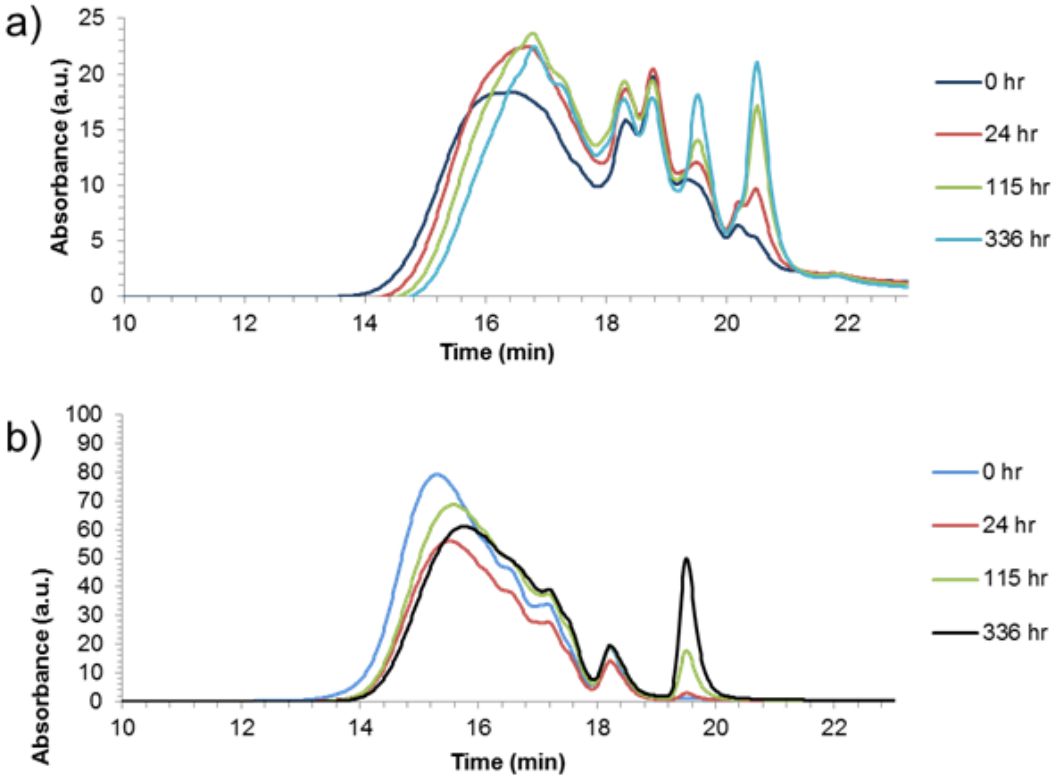

Figure 2.8: GPC chromatograms of an a) irradiated and b) control (not irradiated) sample of polymer **1** after 0, 24, 115, and 336 h of incubation at 37 °C.

polyvinyl alcohol (PVA, 1% w/v) in 10 mM Tris pH 8.0 buffer (6 mL), and probe sonicated for 4 min at 9-10W (Qsonica Sonicator 4000). DCM was then removed by stirring at 600 RPM under house vacuum for 3 h. Remaining PVA was removed by tangential flow filtration (Millipore Pellicon XL, 500 kDa) using 10 mM Tris pH 8.0 buffer (250 mL) at 45 RPM. The retentiate was freeze-dried with 100 mg trehalose as cryoprotectant. The size and distribution of particles were determined by dynamic light scattering (DLS, Malvern Instruments Nanosizer), scanning electron microscopy (SEM, Agilent 8500 FE-SEM), and transmission electron microscopy (TEM, Tecnai FEI Spirit). Loading and encapsulation efficiency was assessed by dissolving lyophilized powder in DCM, extracting FDA into NaOH (0.1 N) and measuring fluorescence of the aqueous phase against a calibration curve in 0.1 N NaOH (Horiba Jobin Yvon FL-1000).

Particle degradation. Freeze-dried particle powder was re-suspended in Tris pH 7.4 buffer and irradiated for 5 min (35 mW/cm^2, λ_{ex} = 320-480 nm, Lumen Dynamics Omnicure S2000 Curing System). Particle degradation was assessed by DLS, SEM, and TEM at different timepoints compared to the non-irradiated sample.

2.6.6 *In vitro* release from particles

Release in 264.7 Raw cells. Raw 264.7 mouse macrophage cells were seeded at 20000 cells/well in DMEM (Corning) supplemented with 10% Fetal Bovine

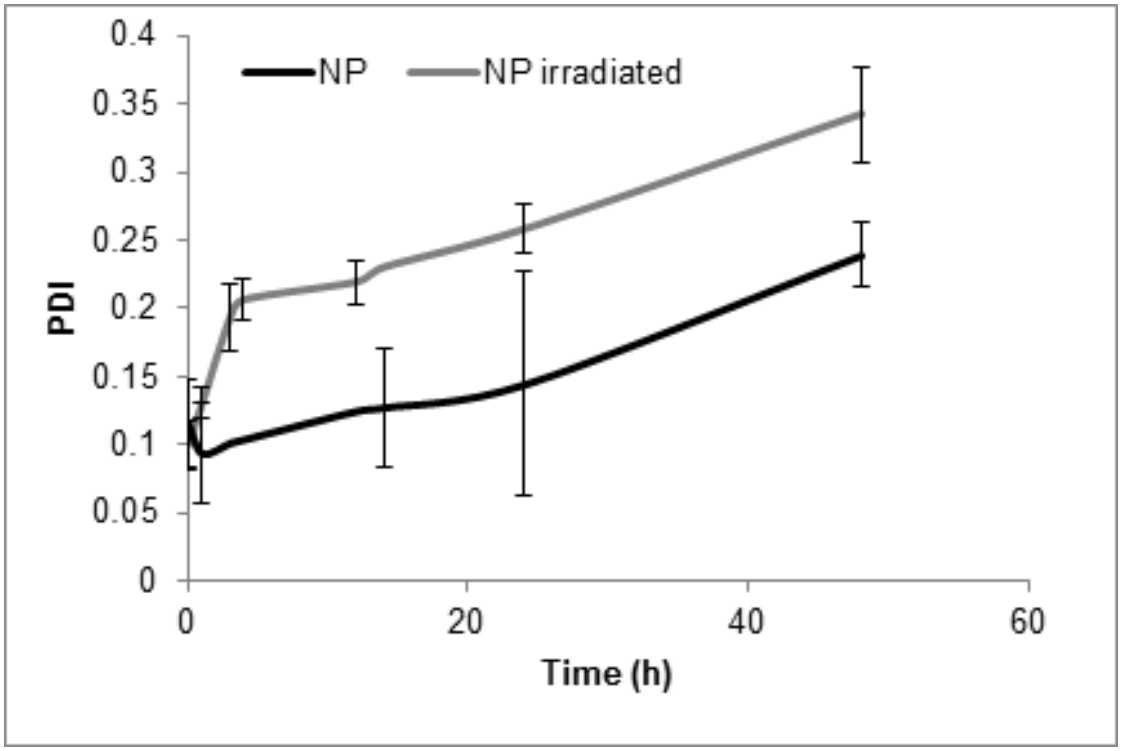

Figure 2.9: PDI of nanoparticles after irradiation 5 min (35 mW/cm^2, λ = 320-480 nm) by DLS.

Serum (FBS, HyClone) and 1% penicillin-streptomycin (Invitrogen) on a 96-well tissue culture-treated plate (Corning) overnight prior to the experiment. Freeze dried FDA-containing particles (10 mg) were resuspended in clear DMEM/FBS (1 mL, no phenol red, Corning). The cells were double washed with warm PBS (100 μL twice) and the particle suspensions in media were added (100 μL). Free FDA (0.1 mg/mL) and empty particles were used as controls. After 3 h incubation at 37 °C, in 5% CO_2 atmosphere, the cells were again double washed with warm PBS (100 μL twice) and clear media (100 μL) was added to each well. Half of the plate was then irradiated for 5 min (10 mW/cm^2, λ_{ex} = 320-480 nm) using the Omnicure. Following a 30 min incubation at 37 °C, in 5% CO_2, the release of FDA was measured by fluorescence measurement (λ_{ex} = 495 nm, λ_{em} = 514 nm) using a plate reader (Molecular Devices SpectraMax M5). To confirm release, fluorescence microscopy images of cells were acquired (Nikon TS100F).

2.6.7 Cytotoxicity assays

Polymer Cytotoxicity. Polymer **1** (5 mg) was dissolved in sterile DMSO (10 μL), and the solution was subsequently added to clear DMEM (990 μL). The resulting suspension was sonicated until uniform and then further diluted to appropriate concentrations in DMEM/FBS media. Lyophilized particles containing FDA (5 mg) were resuspended in sterile media (1 mL) and half of the volume was irradiated for 5 min with UV light (10 mW/cm^2, λ_{ex} = 320-480 nm, OmniCure S2000

Curing System). The solutions were then diluted to appropriate concentrations in cell culture media. 24 hours prior to incubation, Raw 264.7 cells were seeded on a tissue culture treated 96-well plate (Corning) at a density of 20000 cells/well in DMEM media. The cells were washed twice with 100 μL PBS at 37 °, and then incubated with the polymer/particle suspensions in triplicates for 24 h at 37 °C, in 5% CO_2. Following incubation with particles, cells were again washed twice with 100 μL PBS. Following the MTT assay kit instructions, the cells were then incubated at 37 °C, in 5% CO2 for 3 h in 100 μL DMEM containing 0.5 mg/mL 3-[4,5-dimethylthiazol-2-yl]-2,5-diphenyl tetrazolium bromide (MTT agent, Sigma-Aldrich, USA). Triton-X (1% w/v, Sigma-Aldrich) was used as a positive apoptosis control. After the incubation, 100 μL of MTT solution (Sigma-Aldrich) was added to each well and the solution was thoroughly triturated to fully solubilize formazan crystals. To quantify mitochondrial activity, absorbance at 570 nm normalized to background absorbance at 690 nm was measured using a plate reader (Molecular Devices SpectraMax M5).

Particle Cytotoxicity. Lyophilized empty polymer **1** nanoparticles were re-suspended in sterile DMEM/FBS media (1 mL) and diluted to appropriate concentrations in cell culture media. 24 hours prior to incubation, Raw 264.7 cells were seeded on a tissue culture treated 96-well plate (Corning) at a density of 20000 cells/well in DMEM media. The cells were washed twice with 100 μL PBS at 37 °C, and then incubated with the particle suspensions in triplicates for 3 h

at 37 °C, in 5% CO_2. Following incubation with particles, half of the plate was irradiated for 5 min with UV light (10 mW/cm^2, λ_{ex} = 320-480 nm, OmniCure S2000 Curing System). Cells were then incubated for an additional 24h at 37 °C, in 5% CO2. Subsequently, cells were washed twice with 100 μL PBS. Following the MTT assay kit instructions, the cells were then incubated at 37 °C, in 5% CO2 for 3 h in 100 μL DMEM containing 0.5 mg/mL 3-[4,5-dimethylthiazol-2-yl]-2,5-diphenyl tetrazolium bromide (MTT agent, Sigma-Aldrich, USA). Triton-X (1% w/v, Sigma-Aldrich) was used as a positive apoptosis control. After the incubation, 100 μL of MTT solution (Sigma-Aldrich) was added to each well and the solution was thoroughly triturated to fully solubilize formazan crystals. To quantify mitochondrial activity, absorbance at 570 nm normalized to background absorbance at 690 nm was measured using a plate reader (Molecular Devices SpectraMax M5).

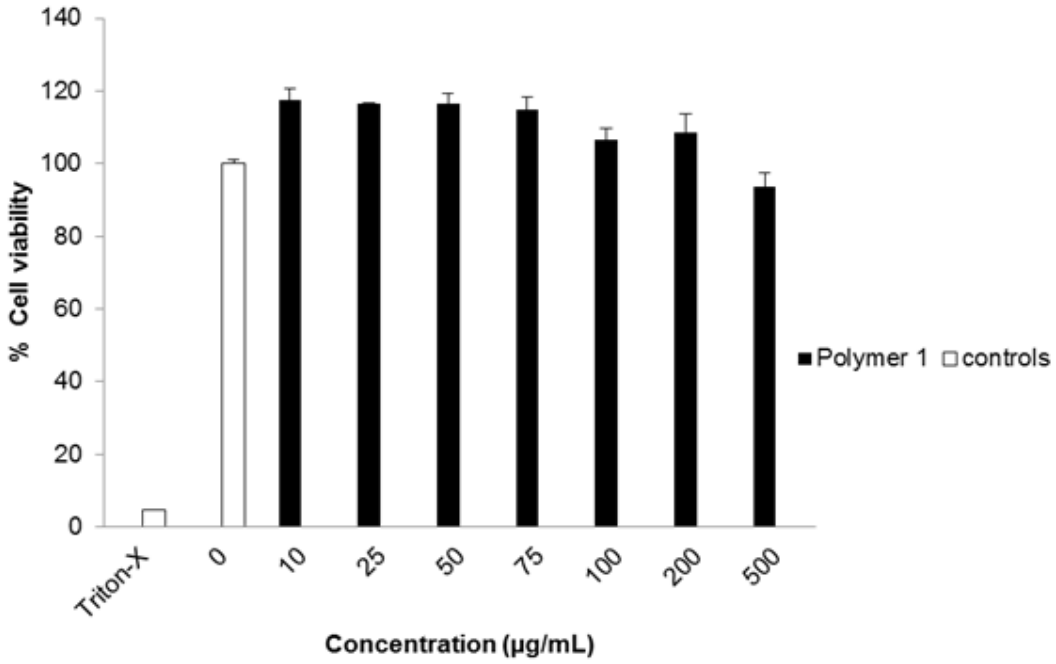

Figure 2.10: MTT assay of polymer **1**.

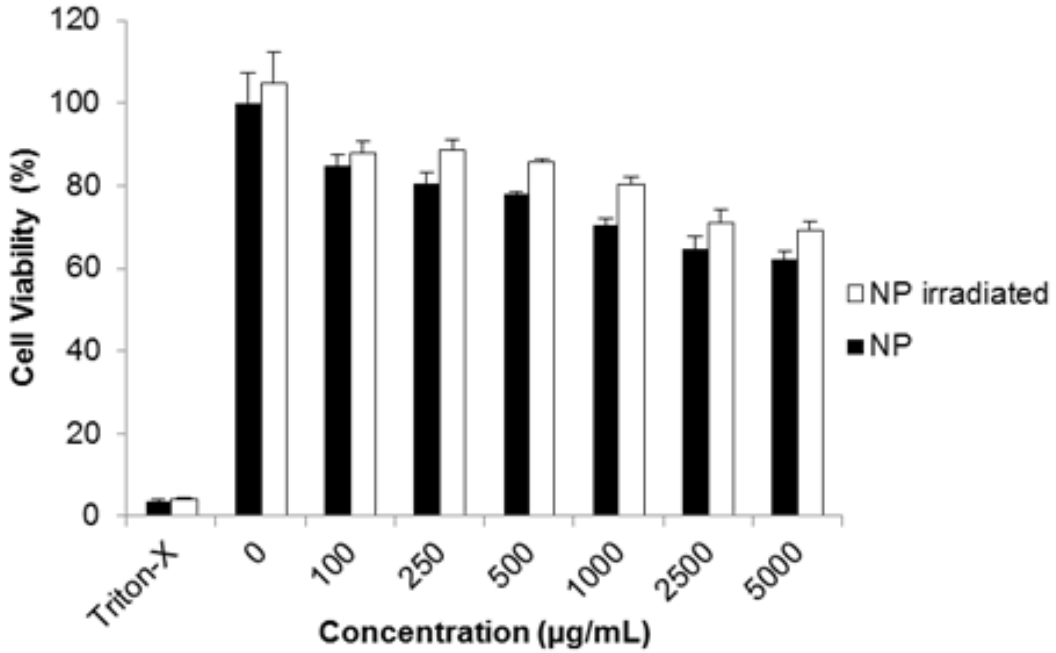

Figure 2.11: MTT assay of cells incubated with particles composed of polymer 1 and irradiated for 5 min with UV light at 10 mW/cm^2.

2.7 References

(1) B. Jeong and A. Gutowska, *Trends in Biotechnology*, 2002, **20**, 305–311.

(2) E. S. Gil and S. M. Hudson, *Progress in Polymer Science*, 2004, **29**, 1173–1222.

(3) J. S. Mejia and E. R. Gillies, *Polymer Chemistry*, 2013, **4**, 1969–1982.

(4) E. Cabane, V. Malinova and W. Meier, *Macromolecular Chemistry and Physics*, 2010, **211**, 1847–1856.

(5) M. W. Tibbitt, B. W. Han, A. M. Kloxin and K. S. Anseth, *Journal of Biomedical Materials Research Part A*, 2012, **100A**, 1647–1654.

(6) K. E. Broaders, S. Grandhe and J. M. Frechet, *Journal of the American Chemical Society*, 2011, **133**, 756–8.

(7) J. Q. Jiang, X. Tong, D. Morris and Y. Zhao, *Macromolecules*, 2006, **39**, 4633–4640.

(8) G. I. Peterson, M. B. Larsen and A. J. Boydston, *Macromolecules*, 2012, **45**, 7317–7328.

(9) A. D. Wong, M. A. DeWit and E. R. Gillies, *Advanced Drug Delivery Reviews*, 2012, **64**, 1031–1045.

(10) S. T. Phillips and A. M. DiLauro, *ACS Macro Lett*, 2014, **3**, 298–304.

(11) A. Sagi, R. Weinstain, N. Karton and D. Shabat, *Journal of the American Chemical Society*, 2008, **130**, 5434–+.

(12) A. P. Esser-Kahn, N. R. Sottos, S. R. White and J. S. Moore, *Journal of the American Chemical Society*, 2010, **132**, 10266–10268.

(13) E. Schopf, J. Sankaranarayanan, M. N. Chan, R. Mattrey and A. Almutairi, *Molecular Pharmaceutics*, 2012, **9**, 1911–1918.

(14) M. A. Dewit and E. R. Gillies, *Journal of the American Chemical Society*, 2009, **131**, 18327–18334.

(15) L. J. Zhang, X. X. Deng, F. S. Du and Z. C. Li, *Macromolecules*, 2013, **46**, 9554–9562.

(16) J. A. Kaitz and J. S. Moore, *Macromolecules*, 2013, **46**, 608–612.

(17) A. M. DiLauro, A. Abbaspourrad, D. A. Weitz and S. T. Phillips, *Macromolecules*, 2013, **46**, 3309–3313.

(18) T. C. Bruice and Piszkiew.D, *Journal of the American Chemical Society*, 1967, **89**, 3568–&.

(19) N. Fomina, J. Sankaranarayanan and A. Almutairi, *Advanced Drug Delivery Reviews*, 2012, **64**, 1005–1020.

(20) N. Fomina, C. McFearin, M. Sermsakdi, O. Edigin and A. Almutairi, *Journal of the American Chemical Society*, 2010, **132**, 9540–9542.

(21) C. C. Zhu, C. Ninh and C. J. Bettinger, *Biomacromolecules*, 2014, **15**, 3474–3494.

(22) R. Jain, S. M. Standley and J. M. J. Frechet, *Macromolecules*, 2007, **40**, 452–457.

(23) N. Murthy, M. C. Xu, S. Schuck, J. Kunisawa, N. Shastri and J. M. J. Frechet, *Proceedings of the National Academy of Sciences of the United States of America*, 2003, **100**, 4995–5000.

(24) N. Murthy, Y. X. Thng, S. Schuck, M. C. Xu and J. M. J. Frechet, *Journal of the American Chemical Society*, 2002, **124**, 12398–12399.

(25) Y. J. Kwon, S. M. Standley, A. P. Goodwin, E. R. Gillies and J. M. J. Frechet, *Molecular Pharmaceutics*, 2005, **2**, 83–91.

(26) M. J. Heffernan and N. Murthy, *Bioconjugate Chemistry*, 2005, **16**, 1340–1342.

(27) J. C. Sy, G. Seshadri, S. C. Yang, M. Brown, T. Oh, S. Dikalov, N. Murthy and M. E. Davis, *Nature Materials*, 2008, **7**, 863–869.

(28) S. E. Paramonov, E. M. Bachelder, T. T. Beaudette, S. M. Standley, C. C. Lee, J. Dashe and J. M. J. Frechet, *Bioconjugate Chemistry*, 2008, **19**, 911–919.

(29) S. C. Yang, M. Bhide, I. N. Crispe, R. H. Pierce and N. Murthy, *Bioconjugate Chemistry*, 2008, **19**, 1164–1169.

(30) J. Sankaranarayanan, E. A. Mahmoud, G. Kim, J. M. Morachis and A. Almutairi, *Acs Nano*, 2010, **4**, 5930–5936.

(31) M. Chan, E. Schopf, J. Sankaranarayanan and A. Almutairi, *Analytical Chemistry*, 2012, **84**, 7779–7784.

(32) C. C. Song, C. C. Su, J. Cheng, F. S. Du, D. H. Liang and Z. C. Li, *Macromolecules*, 2013, **46**, 1093–1100.

(33) Patchorn.A, B. Amit and R. B. Woodward, *Journal of the American Chemical Society*, 1970, **92**, 6333–&.

(34) A. Blanc and C. G. Bochet, *Journal of the American Chemical Society*, 2004, **126**, 7174–7175.

(35) R. K. Wolford and R. G. Bates, *Journal of Physical Chemistry*, 1962, **66**, 1496–&.

(36) R. K. Wolford, *Journal of Physical Chemistry*, 1963, **67**, 632–&.

Chapter 3

In Vivo Visible Light-Triggered Drug Release From an Implanted Depot

3.1 Abstract

Controlling chemistry in space and time has offered scientists and engineers tools for research and technology. For example, on-demand photo-triggered activation of neurotransmitters has revolutionized neuroscience. Non-invasive control of the availability of bioactive molecules in living organisms will undoubtedly lead to major advances; however, this requires the development of photosystems that efficiently respond to regions of the electromagnetic spectrum that innocuously penetrate tissue. To this end, we have developed a polymer that photochemically degrades upon absorption of one-photon visible light and demonstrated its potential for medical applications. Particles formulated from this polymer release molecular cargo in vitro and in vivo upon irradiation with blue visible light through a photoexpansile swelling mechanism.

3.2 Introduction

Controlling chemistry in space and time with light has proven enormously useful in biological research. For example, optogenetics is considered the breakthrough of the decade and has revolutionized neuroscience.[1] However, current means of controlling cellular processes using light require tedious synthetic or genetic development of tools specific to each target. On the other hand, light-responsive nanocarriers[2] can be used to control the activity of any encapsulated bioactive molecule, including proteins and nucleic acids, without the need for chemical modification. Such versatile tools have enormous potential to advance fundamental understanding of physiological, developmental, and disease processes. Externally triggered release of drugs from nanomaterials may also have exciting applications in the treatment of disease, as it could allow precise coordination with biological rhythms or disease activity. Since particles can be injected within the tissue of interest and remain localized in a depot-like manner, the pharmacokinetic profile of the encapsulated biologics can be altered, which is not possible with small molecules. Such an approach would minimize injections and harmful side effects while maximizing therapeutic outcome.

Light-responsive technologies useful in vivo must be highly efficient and capable of responding to electromagnetic radiation that can innocuously penetrate into tissue. To date most photochemical systems do not meet such physiological

requirements, as the majority rely on UV light activation,[23] which is both damaging to cells and does not appreciably penetrate tissues. Systems making use of near-infrared (NIR) laser light by multi-photon approaches, which include two-photon excitation[4] and upconverted UV light,[5,6] have been developed to sidestep these limitations. Unfortunately, achieving sufficient photocleavage of polymer to induce release from nanoparticles by these approaches currently requires extended irradiation at high laser powers, which could lead to heat-induced damage of biological tissues.[7]

The development of one-photon visible light-responsive carriers[8–11] represents an attractive alternative to both one-photon UV- and two-photon NIR-responsive carriers for in vivo applications because it is several orders of magnitude more efficient than two-photon excitation,[12] requiring much shorter irradiation times at lower powers, and is less harmful to cells than UV light.

Inspired by recent developments in the photo-uncaging field, we synthesized a polymer that degrades upon one-photon absorption of blue visible light (polymer **1, Figure 3.1, Figure 3.7**) by incorporating a recently developed red-shifted photocage developed by Donato et al.[12] and used it to formulate particles encapsulating various payloads. Advantages of this photocage over existing systems[3] such as coumarin, nitroveratryls, ruthenium complexes and perylene are the intense visible light absorption up to 500 nm and photo-reactivity in hydrophobic environments, a crucial requirement as most polymer-based delivery vehicles have

a hydrophobic interior.

The results presented in this study highlight the practical utility of one-photon visible light photochemistry for applications in dense, non-transparent mammalian tissues. In an in vivo mouse model we demonstrate light-triggered drug release from a subcutaneously implanted polymer **1** particle depot with blue visible light.

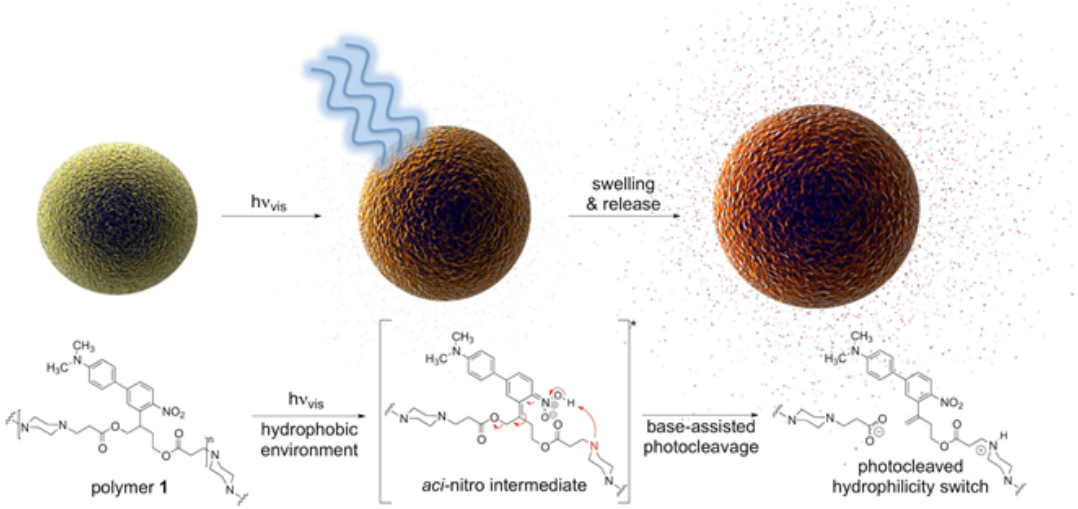

Figure 3.1: Visible light irradiation of particles composed of polymer 1 in aqueous media induces swelling and release of molecular cargo. Tertiary amines within the polymer backbone assist deprotonation of the aci-nitro intermediate in the hydrophobic particle microenvironment leading to β-elimination and photocleavage in favour of photorearrangement.

3.3 Results and discussion

3.3.1 Design, light response and degradation mechanism

In this work, the propyloxy chain of the previously reported ANBP 8 (2-(4âĂŹ-(N,N-dimethylamino)-4-nitro-[1,1âĂŹ-biphenyl]-3-yl)propyl carbonyl) photocage was elongated to yield the butane-diol derivative 2-(4'-N-dimethylamino-4-nitro-[1,1'-biphenyl]-3-yl)butane-1,4-diyl dicarbonyl (ANBB, **Figure 3.1, 3.2, 3.7**). This modification facilitates polymerization and enhances the kinetics of photodegradation by placing the photolabile bond directly in the polymer backbone (**Figure 3.1**).[10,13] Like ANBP, ANBB is photochemically active in hydrophobic environments, a crucial requirement for polymer-based drug delivery vehicles as the particle microenvironment is inherently hydrophobic.

As previously reported, the photochemistry of this class of photoresponsive molecules is strongly dependent on solvent and basicity.[14] In water, the photo-induced aci-nitro intermediate (**Figure 3.1**) is deprotonated, causing the compound to undergo photocleavage by a β-elimination pathway to yield a nitro-alkene derivative.[12] However, in hydrophobic non-basic environments, these molecules photorearrange to a hydroxy-nitroso isomer[14] (**Figure 3.2**). To increase the release efficiency from corresponding particles and potentially enhance metabolism and excretion of the photodegraded carrier material, we reasoned that the introduction of basic tertiary amines in the polymer **1** backbone would assist deprotonation

of the photo-induced aci-nitro intermediate in the hydrophobic particle microenvironment in favour of photorearrangement (**Figure 3.1, 3.2c-d**). To inform the design of our polymer, we examined the photoreactions of model compounds **2** (no tertiary amines) and **3** (tertiary amines) in hydrophobic solvent to mimic the particle microenvironment (**Figure 3.2, Figure 3.7**). As revealed by HPLC-MS, the non-basic compound **2** yielded only the photostable photorearranged nitroso-hydroxy isomer **2a** upon irradiation with visible light (λ_{ex} = 400-500 nm) in CH_2Cl_2 (**Figure 3.2a-b**), whereas the basic compound **3** underwent a much more complex photoreaction (**Figure 3.2c-d**). Analysis of the photoreaction of compound **3** revealed that the major reaction product was indeed the photocleaved nitro-alkene derivative **3a**, which was isolated and identified by ^{1}H NMR spectroscopy (**Figure 3.8**) and high-resolution mass spectroscopy. However, compound **3** was also observed to directly generate the photorearranged hydroxy-nitroso minor product **3b**, alongside a photocleaved minor product **3c** upon irradiation (**Figure 3.2c-d**). Furthermore, as has been previously observed with similar compounds,10 the photocleaved nitro-alkene product **3a** is not photostable and undergoes multiple subsequent photochemical transformations upon prolonged irradiation (**Figure 3.2c-d**). Despite considerable efforts, secondary photoproducts (**3c**, **3d**, **3e** and minor products) could not be identified. The observed photochemical behavior of compound **3** confirms that the introduction of tertiary amines indeed promotes photocleavage in hydrophobic environments, such as the interior of a polymeric

particle.

The photoresponsive polymer **1** (Mw = 31.7 kDa, PDI = 2.7) was synthesized in five steps at 17% overall yield starting from a previously reported compound8 (see supplementary information and **Figure 3.7** for synthetic details). Upon irradiation of polymer **1** in CH_2Cl_2 with visible light (λ_{ex} = 400-500 nm), the long-wavelength absorption peak at λ_{max} = 398 nm decreases as a new absorption peak at λ_{max} = 458 nm increases, resulting in a visually recognizable color change from yellow to orange (**Figure 3.3a** inset). The substantial increase in the GPC retention time of polymer **1** after irradiation in CH_2Cl_2 indicates amine-assisted photocleavage upon irradiation and the formation of smaller segments (**Figure 3.3b**). The greater solubility of the photoproducts of polymer **1** in methanol and in water containing 1% w/v Pluronic F127 further indicates photodegradation into smaller, more polar segments (**Figure 3.9**).

HPLC-MS analysis of the methanol-soluble photodegraded material revealed a complex mixture of photoproducts, including peaks with masses corresponding to the smallest photocleaved products anticipated (**Figure 3.10**). We also studied the photochemistry of polymer **1** in $CDCl_3$ by ^{1}H NMR spectroscopy. Peaks corresponding to the photocleaved nitro-alkene product were observed upon irradiation by comparing the spectrum of irradiated polymer **1** to that of **3a** (**Figure 3.8**). However, since the photocleaved nitro-alkene product was quickly consumed by secondary photoreactions and the product precipitated (likely be-

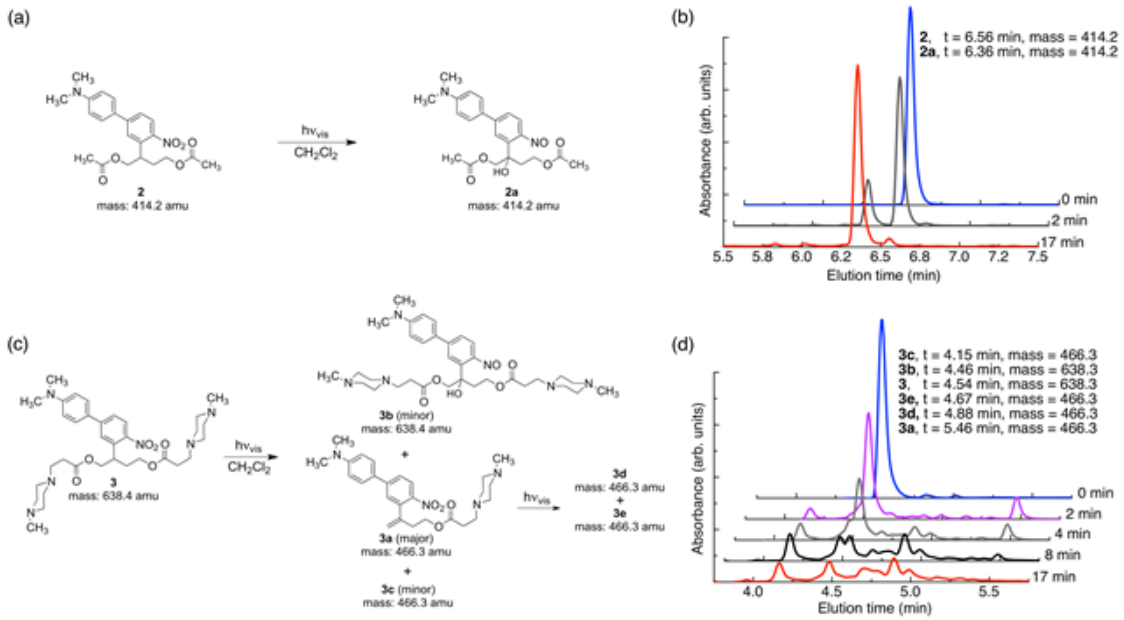

Figure 3.2: Tertiary amines modulate the photochemistry of ANBB in hydrophobic environments. (a, b) Compound 2 cleanly reacts upon irradiation with visible light (λ_{ex} = 400-500 nm, 0.18 W, 0.21 W/cm^2) in CH_2Cl_2 ($6 * 10^{-5}$ M) to yield photorearranged hydroxy-nitroso product **2a**. (c, d) Compound **3** has more complex photochemistry and yields photocleaved **3a** (major product), photorearranged **3b** (minor product) and photocleaved **3c** (minor product) upon irradiation with visible light in CH_2Cl_2. 3a is not photostable and reacts further upon prolonged irradiation to yield major photoproducts **3d** and **3e**. The exact mass calculated (**2**, **2a**, **3**, **3a** and **3c**) and measured (**2**, **2a**, **3a**, **3b**, **3c**, **3d** and **3e** (mass of protons subtracted)) is indicated.

cause of high polarity), line broadening and decreased peak heights thwarted detailed analysis. Attenuation of visible light by dermal tissue does not prevent polymer photocleavage.

To test the practical utility of one-photon visible light driven photochemistry for in vivo applications, we examined the efficiency of photochemistry after passage of light through hairless mouse skin (thickness: 0.45 mm) sandwiched between two glass slides (**Figure 3.4a**, **3.11**). Polymer **1** solutions were irradiated with and without this tissue filter in the beam path and the photoreaction kinetics were measured by UV-Vis absorption spectroscopy (**Figure 3.4b**). Under direct blue light excitation (λ_{ex} = 400-500 nm, 0.18 W), the photoreaction reached 100% completion after only 10 min (**Figure 3.4b**, open circles), whereas under skin-attenuated irradiation, the photoreaction reached 22% completion within the same irradiation time (**Figure 3.4b**, solid circles). As the optical power reaching the sample after passage through the glass/skin tissue filter was attenuated by 82% (glass/skin = 0.03 W, skin alone = 0.06 W, **Table 3.1**), this reduction indicates a linear correlation between optical power and reactivity of one-photon absorption, since the rate constant and reaction completion was reduced by 79% and 78%, respectively. These results thus highlight the utility of delivery systems that respond efficiently to one-photon visible light.

3.3.2 Formulation of Nile red-loaded polymeric particles and photo-induced release

As our ultimate goal is light-triggered drug delivery, we next examined release of cargo *in vitro* using Nile red as a model drug. As the traditional Nile red release method of measuring the decrease in Nile red fluorescence as it is increasingly exposed to the surrounding aqueous solution cannot distinguish between an increase in particle hydrophilicity and cargo release, we employed a distinct approach. So that release of dye would correspond with an increase in fluorescence, we sought to encapsulate a high concentration of dye to quench its fluorescence inside the particle. For this purpose, polymer **1** was formulated into particles by electrospray[15] (see supplementary information for experimental details). This convenient formulation method produces dense, solid polymer particles in a one-step process with unrivalled payload encapsulation efficiencies, a highly desirable feature for therapeutic applications. Representative scanning electron microscopic (SEM) images of the particles are shown in **Figure 3.12**. We studied the kinetics of light-induced release of Nile red from polymer **1** particles (P-**1**-NR, size: 1.1 $\pm$ 0.3 μm (SEM), dye loading: 5.6% w/w) by directly monitoring changes in fluorescence intensity of the aqueous particle suspensions containing 1% w/v Pluronic F127 upon irradiation with visible light. When P-**1**-NR was irradiated with blue visible light, a substantial increase in fluorescence intensity, indicative of photo-triggered release, was observed (**Figure 3.5a**, solid circles). In contrast,

the fluorescence intensity did not change significantly for particles not exposed to visible light (**Figure 3.5a**, open circles). We further quantitatively measured the Nile red released from the particles into solution by separating the particles from the solution by centrifugation. We found that while only 2.0 ± 0.7% Nile red was released from non-irradiated controls, samples irradiated for 90 min released 57 ± 5% of the encapsulated Nile red, which corresponds to 1.3 ± 0.1 μg (**Figure 3.5b**). Light-triggered release from the P-**1**-NR particles can also be followed with the naked eye, as the supernatant of centrifuged irradiated samples becomes pink, whereas non-irradiated controls display colourless supernatant as the dye is well retained in the particles without light stimulation (**Figure 5c**). We also investigated whether release of Nile red could continue after shorter irradiation times in order to minimize irradiation time, however we did not observe continued release under these conditions. The kinetics of P-**1**-NR particles' photolysis was measured by UV-Vis spectroscopy. We observed photochemical changes in P-**1**-NR particles over 60 min of irradiation, which matches well with the Nile red release kinetics (**Figure 3.5a**, **3.13a-b**). When further comparing the absorption and rate of photolysis between polymer **1**, P-**1**-NR and empty polymer **1** particles (P-**1**), significant differences were observed. First, the absorbance of P-**1**-NR (λ_{max} = 475 nm) and P-**1** (λ_{max} = 438 nm) was red-shifted compared to polymer **1** in CH_2Cl_2 (λ_{max} = 398 nm). Second, photolysis rates differed considerably, that is, photolysis was complete at 10, 15 and 60 min, for polymer **1**, P-**1** and P-**1**-NR

respectively (**Figure 3.4b**, **3.14**). Although the particles absorb more visible light than polymer **1** in CH_2Cl_2, it appears that particle formulation decreases the photochemical efficiency of polymer **1**. This decrease may result from water quenching and/or close proximity of the photocages in the particle, leading to self-quenching. Furthermore, it appears that Nile red reduces the rate of photolysis, either due to inner filter effect or energy transfer from the photocages to Nile red molecules.

To examine the physical changes underlying release, the morphology, size, and structure of the particles before and after irradiation were studied by particle size analyser (Multisizer) and SEM. Upon prolonged irradiation, we observed a progressive increase in particle diameter from 1.03 $\pm$ 0.02 to 1.35 $\pm$ 0.04 μm after 90 min of irradiation (**Figure 3.5d**). This expansion likely results from hydrophobic-to-hydrophilic photoswitching within the particles, which leads to influx of water. Interestingly, we did not observe evidence of particle degradation/breaking apart by SEM (**Figure 3.12**), which may indicate ionic and hydrogen bonding between the photodegraded segments and/or insufficient water solubility of the photoproducts. Based on these observations, release appears to occur through increased hydrophilicity and fluidity of the particles upon amine-assisted photocleavage and photorearrangement of the polymer.

3.3.3 Photorelease of dexamethasone from implanted depot

On-demand visible light-triggered release of biologically active agents from an implanted depot would allow local self-administration while minimizing invasive injections and systemic side effects. Furthermore, a particle depot alters the pharmacokinetic behaviour of the encapsulated cargo, allowing it to remain localized at the injection site for much longer than small molecules. Upon irradiation the cargo is released locally and on demand. To assess the viability of the technology in animals, we examined the effect of subcutaneous light-triggered release of dexamethasone (Dex), a well-characterized anti-inflammatory drug,[16] on carrageenan-induced hind paw inflammation, a favoured model to assess the anti-inflammatory properties of potential therapeutic agents.[17]

Carrageenan, a linear sulfated polysaccharide that triggers the release of inflammatory and proinflammatory mediators, was injected into the left hind footpad of the mouse; the right hind footpad was injected with DulbeccoâĂŹs phosphate buffered saline (DPBS, 25 μL) as an internal control. Using electrospray, we encapsulated Dex in photoresponsive polymer **1** particles (P-**1**-Dex, Dex loading: 1% w/w, size by SEM: 0.42 $\pm$ 0.07 μm, hydrodynamic size by dynamic light scattering (DLS): 0.95 $\pm$ 0.5 μm, **Figure 3.14**) along with the NIR fluorescent probe IR780 (0.1% w/w) to allow *in vivo* monitoring of the depot distribution in real time (**Figure 3.6a-b, 3.15**).

One hour prior to induction of inflammation by carrageenan, P-**1**-Dex depots were injected subcutaneously in the left hind hock. Depots were then irradiated at the injection site with blue light for 40 minutes between hind paw thickness measurements (**Figure 3.6c**, **3.16**). IR780 labelling allowed tracking of the depot location by an in vivo imaging system (IVIS) before and after irradiation of the particles (**Figure 3.6b**, **3.15**). Controls included non-irradiated P-**1**-Dex depot, DPBS with and without light exposure, free Dex, empty particles (P-**1**) and pre-irradiated P-**1** particles (**Figure 3.17**). Hind paws of mice injected with DPBS (**Figure 3.6d**, **3.17**) increased from 0.28 ± 0.1 mm (t = 0.1 h after carrageenan injection) to a maximum of 0.71 ± 0.1 mm thicker than untreated paws (t = 5 h), while swelling in those treated with free Dex (**Figure 3.6d**) was slightly but statistically insignificantly (p = 0.5) lower, with a maximal difference in thickness of 0.63 ± 0.2 mm greater than control paws (t = 5 h). In contrast, irradiation of the P-**1**-Dex particle depot (**Figure 3.6d**), led to considerably and statistically significantly (p = 0.02) less swelling at maximal inflammation, i.e., 0.44 ± 0.1 mm (t = 5 h). We hypothesize that the lower therapeutic efficacy associated with free Dex compared to P-**1**-Dex + Light results from the rapid diffusion of free Dex dose into the systemic circulation. In comparison, the sustained light-triggered release of Dex from the implanted P-**1**-Dex depot makes it more available over time because the depot remained stationary during the experiment, as monitored by IVIS (**Figure 3.15**).

As we did not observe any statistically significant reduction in inflammation associated with the non-irradiated P-**1**-Dex group (t = 5 h, paw thickness = 0.72 ± 0.08 mm, p = 0.9) (**Figure 3.6d**), we can assume that Dex stays well retained within the drug carrier. Treatment with light alone, empty P-**1** particles, or pre-irradiated P-**1** particles resulted in similar paw inflammation as in mice given DPBS (**Figure 3.17**), ruling out therapeutic effects by either light or the carrier material.

We observed no gross changes to the color or texture of the skin following irradiation (**Figure 3.18**). However, we observed a slight swelling (oedema) of the thigh in a few cases (**Figure 3.19**) that appeared to result from prolonged irradiation, which resorbed the day after light exposure. Furthermore, no signs of adverse effects from the carrier material in non-irradiated mice were apparent (**Figure 3.18**), in agreement with the cytotoxicity data (MTT assay) obtained for empty P-**1** particles, which showed excellent tolerance by Raw 264.7 mouse macrophage cells at concentrations up to 400 μg/mL (400 μg/mL = 115 ± 7% viability) (**Figure 3.20a**). However, irradiated P-**1** particles were less tolerated above concentrations of 100 μg/mL (400 μg/mL = 65 ± 30% viability) (**Figure 3.20a**). The free polymer **1** before and after irradiation was less tolerated compared to the particles, which demonstrate that particle formulation mitigates the toxicity (**Figure 3.20b**). In conclusion, we demonstrated on-demand one-photon visible light-triggered release of an anti-inflammatory agent *in vivo*, which reduced

local hind paw inflammation more efficiently than free Dex (**Figure 3.6d**). Greater therapeutic effects might be possible with more hydrophobic drugs, which would allow higher loading efficiency.

3.4 Conclusions

This report introduces a polymer that degrades upon one-photon absorption of blue visible light, which we show enables *in vivo* photorelease of dexamethasone from a subcutaneously implanted depot of polymeric particles. Due to the altered pharmacokinetics of the implanted depot, compared to the free drug, the photoreleased Dex lowered inflammation with greater efficiency than the free drug, which rapidly diffused from the site of injection. The release mechanism appears to involve expansion of the polymeric matrix by photoinduced photodegradation and hydrophilicity switching, as demonstrated by size measurements.

The *in vivo* model used in this work demonstrates the practical utility of one-photon visible light for on-demand subcutaneous release of biological effectors. Visible light-responsive polymers and materials could become an important tool to enable light-mediated release in a multitude of animal research models.

Materials that respond to long-wavelength one-photon visible light, which is more suited for deeper tissue *in vivo* photorelease applications because of lower absorption of these wavelengths relative to the blue light used here, are currently under development.

3.5 Acknowledgements

The authors acknowledge the NIH New Innovator Award (DP 2OD006499) and King Abdulaziz City for Science and Technology (through the KACST-UCSD Center for Excellence in Nanomedicine and Engineering) for funding. NMR spectra were acquired at UCSD Skaggs School of Pharmacy and Pharmaceutical Sciences NMR facility. High-resolution mass spectroscopic data was measured at the UCSD Biomolecular and Proteomics Mass Spectrometry Facility. The authors are grateful to Dr. Jacques Lux, Jessica Moore, Marlene Arredondo, Jason Olejniczak, Dr. Caroline de Gracia Lux, Dr. Amy Moore, Dr. Shivanjali Joshi-Barr and Dr. Brendan Duggan for insightful and technical help.

Chapter 3, in full, is a reformatted reprint of the material as it appears in Chemical Science 2015. Carling, Carl-Johan; Viger, Mathieu; Nguyen Huu, Viet Anh; Garcia, Arnold; Almutairi, Adah, RSC Press, 2015. The dissertation/thesis author was the co-author of this paper.

3.6 Supporting Information

3.6.1 General methods and instrumentation

All chemicals and solvents were purchased from Sigma-Aldrich and used as received unless specified. Compound **4** was synthesized according to a published procedure. Anhydrous solvents were acquired from a solvent purification

system (LC Technology Solutions Inc., SP-1). Silica gel flash column chromatography was performed using an automated CombiFlash Rf 200 system. Polymer **1** was analyzed by GPC using a Waters e2196 Series HPLC system equipped with RI and PDA detectors and a Waters Styragel HR 2 size-exclusion column with 0.1% LiBr/DMF as eluent and flow rate of 1 mL/min at 37 °C. Monodisperse poly(methyl methacrylate) (PMMA) standards were used to determine the molecular weight and PDI of polymer **1**. ^{1}H NMR and ^{13}C NMR spectra were acquired using a Varian spectrometer working at 600 MHz and 150 MHz respectively. Chemical shifts (δ) are reported in ppm relative to TMS, and coupling constants (J) are reported in hertz. High-resolution mass spectra were acquired using an Agilent 6230 ESI-TOFMS in positive ion mode. Low-resolution HPLC-MS chromatograms of model compounds **2** and **3** and corresponding irradiated samples and irradiated samples of polymer **1** were acquired on an Agilent Technologies 1260/1290 Infinity HPLC-MS equipped with a ZORBAX 1.8 μm (2.1 x 50 mm) SB-C18 column and 6120 Quadrapole detector and run in a gradient of water and acetonitrile with 0.1% formic acid. UV-visible absorption spectra were collected using a Shimadzu UV-3600 UV-Vis spectrophotometer. Fluorescence spectra were acquired using a Horiba Jobin Yvon spectrofluorometer. Particles were imaged using an Agilent 8500FE scanning electron microscope. Changes in particle diameter were measured using a Multisizer 4 Coulter counter. Polymer **1**, model compounds **2** and **3** and particle samples P-**1**-NR, P-**1**-Dex and P-**1** were irradiated with visible light

using a high pressure 200 W Mercury vapor short arc lamp in an OmniCure S2000 system filtered through a 400-500 nm bandpass filter. The output power of the OmniCure system was set to 10% and the light beam was focused on the sample via a light guide. The light power was measured using a Newport 1936-R optical power meter.

3.6.2 Synthesis of 5

An oven-dried round-bottom flask under argon was charged with compound **4** (10.89 g, 34.44 mmol, 1 eq.), Bu_4NBr (2.22 g, 6.89 mmol, 0.2 eq.) and anhydrous K_2CO_3 (14.28 g, 103.33 mmol, 3 eq.). The system was evacuated and backfilled with argon twice. Anhydrous CH_3CN (300 mL) was added and the reaction heated to 84 °C. The solution gradually turned dark purple. After 10 min, tert-butyl-bromoacetate (10.17 mL, 68.89 mmol, 2 eq.) was added. The reaction promptly changed color to light yellow. The reaction was refluxed overnight, the light yellow suspension was allowed to cool. The suspension was vacuum filtered and the light yellow solid was washed several times with EtOAc. The filtrate was subsequently concentrated to yield an oil. The title compound 5 was purified by silica gel column chromatography (220 g column, 5% EtOAc in hexanes) to yield a viscous light yellow oil (10.27 g, 23.86 mmol, 69% yield). The compound was stored at room temperature.

^{1}H NMR (600 MHz, $CDCl_3$) δ 7.86 (d, J: 8.6 Hz, 1H), 7.60 (d, J: 1.9 Hz,

1H), 7.56 (dd, J: 1.9, 8.6 Hz, 1H), 4.51 (t, J: 7.2 Hz, 1H), 3.14 (dd, J: 7.4, 16.6 Hz, 1H), 2.74 (dd, J: 7.0, 16.6 Hz, 1H), 1.40 (s, 9H), 1.39 (s, 9H)

^{13}C NMR (150 MHz, $CDCl_3$) δ 170.19, 147.90 169.94, 135.79, 134.00, 131.55, 128.13, 126.76, 82.58, 81.49, 45.12, 38.12, 28.12, 27.92

HRMS (ESI-TOFMS) calc. mass ($C_{18}H_{24}BrNO_6Na$)+ $[M+Na]^+$ 452.0679 g/mol, experimental mass $[M+Na]^+$ 452.0680 g/mol, delta ppm: 0.2

3.6.3 Synthesis of 6

An oven-dried round bottom flask and drop funnel under argon was charged with compound **5** (5.6 g, 13.01 mmol, 1 eq.) in anhydrous THF (4 mL). Anhydrous THF (100 mL) was added and the resulting solution was cooled to 0 °C. DIBAL-H (91.1 mL, 91.1 mmol, 7 eq., 1M in THF) was added dropwise to the reaction over 30 min. The reaction was stirred at 0 °C for 3.5 h. The reaction mixture was poured into water, which led to gas and heat evolution. The resulting sludge was extracted with EtOAc (4 x 200 mL) and the combined organic extracts were dried over $MgSO_4$, vacuum-filtered and concentrated to a light yellow solid. The title compound 6 was purified by silica gel column chromatography (80 g column, gradient 20% $\rightarrow$ 50% EtOAc in hexanes) to yield a light yellow solid (1.65 g, 5.69 mmol, 44% yield). The mono-reduced isomer was also isolated as a light yellow oil (1.85 g, 5.13 mmol, 39% yield). The compounds were stored at ambient temperature in a foil-wrapped vial.

Melting point: 120-122 °C

^{1}H NMR (600 MHz, CD_3OD) δ 7.79 (d, J: 2.1 Hz, 1H), 7.70 (d, J: 8.6 Hz, 1H), 7.60 (dd, J: 2.1, 8.6 Hz, 1H), 3.75 (d, J: 6.7 Hz, 2H), 3.54-3.42 (m, 3H), 2.09-2.04 (m, 1H), 1.92-1.86 (m, 1H)

^{13}C NMR (150 MHz, CD_3OD) δ 151.35, 141.00, 133.20, 131.09, 126.92, 126.30, 66.10, 60.44, 40.07, 35.79

HRMS (ESI-TOFMS) calc. mass ($C_{10}H_{22}BrNO_4Na$)+ $[M+Na]^+$ 311.984 g/mol, experimental mass $[M+Na]^+$ 311.9844 g/mol, delta ppm: 0.6

3.6.4 Synthesis of 7

A two-neck round bottom flask equipped with a condenser was charged with **6** (447 mg, 1.54 mmol, 1 eq.), 4-Dimethylaminophenylboronic acid (267 mg, 1.67 mmol, 1.05 eq.), Na_2CO_3 (1.63 g, 15.4 mmol, 10 eq.), Toluene (8 mL), EtOH (1.5 mL) and H2O (2.6 mL). The resulting dispersion was deoxygenated by bubbling argon over 25 min. $Pd(PPh_3)_4$ (89 mg, 0.077 mmol, 0.05 eq.) was added, the system purged, wrapped in foil and heated to 90 °C in an oil bath. After 18.5 h the reaction was cooled and diluted with H_2O and EtOAc. The phases were separated and the aqueous phase extracted with EtOAc (3 x 50 mL). The combined organic extracts were dried over $MgSO_4$, vacuum-filtered and concentrated to an orange solid. The title compound **7** was purified by silica gel column chromatography (40 g column, gradient 40% $\rightarrow$ 60% EtOAc in hexanes) to yield an orange solid (490.5

mg, 1.48 mmol, 96% yield). The compound was stored at ambient temperature in a foil-wrapped vial.

Melting point: 149-151 °C

^{1}H NMR (600 MHz, $CDCl_3$) δ 7.85 (d, J: 8.8 Hz, 1H), 7.61 (d, J: 1.3 Hz, 1H), 7.52-7.50 (m, 3H), 6.82 (bs, 2H), 3.91 (d, J: 6.2 Hz, 2H), 3.76-3.73 (m, 1H), 3.68-3.63 (m, 2H), 3.03 (s, 6H), 2.18-2.12 (m, 1H), 2.04-1.98 (m, 1H)

^{13}C NMR (150 MHz, $CDCl_3$) δ 150.9, 148.6, 148.6, 146.2, 138.2, 128.7, 126.2, 125.8, 125.0, 113.2, 67.4, 61.6, 40.9, 40.2, 36.4

HRMS (ESI-TOFMS) calc. mass ($C_{18}H_{23}N_2O_4$)+ $[M+H]^+$ 331.1652 g/mol, experimental mass $[M+H]^+$ 311.1652 g/mol, delta ppm: 1.8

3.6.5 Synthesis of 8

An oven-dried round bottom flask under argon was charged with **7** (332 mg, 1.0 mmol, 1 eq.). **7** was first dissolved in anhydrous DMF (3 mL) and then diluted with anhydrous CH_2Cl_2 (13 mL). The resulting orange solution was wrapped in foil and cooled to 0 °C. Et_3N (0.42 mL, 3.01 mmol, 3 eq.) was added and acroyl chloride (0.18 mL, 2.21 mmol, 2.2 eq.) was added dropwise over 3 min. The reaction was removed from the cold bath and stirred over night, then poured into H_2O and extracted with CH_2Cl_2 (5 x 50 mL). The combined organic extracts were dried over $MgSO_4$, vacuum-filtered and concentrated to an orange oil. The title compound **8** was purified twice by silica gel column chromatography (40 g

column, 1st: 20%, 2nd: 10% EtOAc in hexanes) to yield an orange solid (335.9 mg, 0.77 mmol, 77% yield). The compound was stored at ambient temperature in a foil-wrapped vial.

Melting point: 96-98 °C

^{1}H NMR (600 MHz, $CDCl_3$) δ 7.87 (d, J: 8.5 Hz, 1H), 7.58 (d, J: 1.9 Hz, 1H), 7.53 (dd, J: 1.9, 8.2 Hz, 1H), 7.49 (d, J: 8.9 Hz, 2H), 6.79 (d, J: 8.9 Hz, 2H), 6.34 (dt, J: 1.2, 17.0 Hz, 2H), 6.10-6.01 (m, 2H), 5.82-5.78 (m, 2H), 4.48-4.45 (m, 1H), 4.41-4.39 (m, 1H), 4.23-4.21 (m, 1H), 4.12-4.09 (m, 1H), 4.01-4.00 (m, 1H), 3.03 (s, 6H), 2.30-2.24 (m, 1H), 2.22-2.16 (m, 1H)

^{13}C NMR (150 MHz, $CDCl_3$) δ 166.3, 166.2, 151.1, 148.7, 148.7, 146.4, 136.2, 131.7, 128.6, 126.2, 126.1, 125.5, 113.1, 68.0, 62.5, 40.9, 36.1, 31.6 (Peak at 148.7 is 2 distinct carbons as revealed by HSQC and HMBC)

HRMS (ESI-TOFMS) calc. mass ($C_{24}H_{27}N_2O_6$)+ $[M+H]^+$ 439.1864 g/mol, experimental mass $[M+H]^+$ 439.1866 g/mol, delta ppm: 0.5

3.6.6 Synthesis of polymer 1

A 4-dram vial equipped with a stir bar was charged with **7** (161 mg, 0.367 mmol, 1 eq.) and piperazine (31.6 mg, 0.367 mmol, 1 eq.). Acetone (2 mL) was added and the resulting suspension was sonicated until all solids were solubilized. The vial was wrapped in foil, charged with Et_3N (0.25 mL, 1.835 mmol, 5 eq.), capped and purged with argon. The reaction was stirred at ambient temperature

for 4 d, at which point the orange dispersion was concentrated under reduced pressure, taken up in CH_2Cl_2 (1 mL) and crashed into ice-cold EtOH (10 mL). The suspension was centrifuged (5250 rpm, 15 min, 4 °C) and the light yellow supernatant was discarded. The orange pellet was dissolved in CH_2Cl_2 (1 mL) and the purification procedure was repeated thrice more. The purified polymer **1** was obtained as an orange solid (148 mg, 75% yield, Mw: 31.7 kDa (PMMA standard), PDI: 2.7).

^{1}H NMR (600 MHz, $CDCl_3$) δ 7.84 (bd, J: 8.4 Hz, 1H), 7.54 (s, 1H), 7.52-7.48 (m, 3H), 6.78 (bd, J: 7.7 Hz, 2H), 4.37-4.35 (m, 1H), 4.31-4.29 (m, 1H), 4.10-4.07 (m, 1H), 4.02-3.98 (m, 1H), 3.93-3.88 (m, 1H), 3.01 (s, 6H), 2.60-2.49 (m, 4H), 2.43-2.35 (m, 8H), 2.16-2.10 (m, 2H)

3.6.7 Synthesis of 2

An oven-dried round bottom flask under argon was charged with **7** (44.5 mg, 0.135 mmol, 1 eq.) and DMAP (49.4 mg, 0.404 mmol, 3 eq.). Anhydrous THF (8 mL) was added and the solution cooled to 0 °C. Acetic anhydride (38.2 μL, 0.404 mmol, 3 eq.) was added and the reaction was removed from the cold bath and stirred for 2 h. The reaction was concentrated and the crude material was taken up in CH_2Cl_2 and concentrated onto silica. The title compound **2** was purified by silica gel column chromatography (12 g column, 20% EtOAc in Hexanes) to yield an orange oil (53.2 mg, 0.128 mmol, 95% yield). The compound was stored at

ambient temperature wrapped in foil.

^{1}H NMR (600 MHz, $CDCl_3$) δ 7.85 (d, J: 8.5 Hz, 1H), 7.55 (d, J: 2.0 Hz, 1H), 7.52 (dd, J: 2.0, 8.5 Hz, 1H), 7.51 (d, 9.3 Hz, 2H), 6.83 (bs, 2H), 4.39-4.36 (m, 1H), 4.29-4.26 (m, 1H), 4.09-4.07 (m, 1H), 4.00-3.98 (m, 1H), 3.97-3.92 (m, 1H), 3.04 (s, 6H), 2.22-2.16 (m, 1H), 2.13-2.07 (m, 1H), 2.02 (s, 3H), 1.98 (s, 3H)

^{13}C NMR (150 MHz, CD_3OD) δ 171.2, 171.1, 151.1, 148.8, 146.3, 136.1, 128.5, 126.1, 126.0, 125.4, 113.1, 67.9, 62.3, 40.7, 35.7, 31.6, 21.3, 21.1

HRMS (ESI-TOFMS) calc. mass ($C_{22}H_{27}N_2O_6$)+ $[M+H]^+$ 415.1864 g/mol, experimental mass $[M+H]^+$ 418.1867 g/mol, delta ppm: 0.7

3.6.8 Synthesis of 3

A 4-dram vial equipped with a stir bar was charged with **8** (58.2 mg, 0.133 mmol, 1 eq.). Acetone (2 mL), Et_3N (0.092 mL, 0.664 mmol, 5 eq.) and methyl piperazine (0.044 mL, 0.398 mmol, 3 eq.) was added. The vial was capped, purged with argon, wrapped in foil and stirred at ambient temperature during 2 days at which point the reaction mixture was poured into sat. $NaHCO_3$ and extracted with EtOAc (4 x 20 mL). The combined organic extracts were dried over $MgSO_4$, vacuum filtered and concentrated to an orange oil. The crude material was taken up in CH_2Cl_2 and concentrated onto silica. The title compound **3** was purified by silica gel column chromatography (12 g column, gradient 10% $\rightarrow$ 30% MeOH in CH_2Cl_2) to yield a viscous orange oil (76.1 mg, 0.12 mmol, 90% yield). The

compound was stored at ambient temperature wrapped in foil.

^{1}H NMR (600 MHz, $CDCl_3$) δ 7.84 (d, J: 8.5 Hz, 1H), 7.54 (s, 1H), 7.52 (d, J: 8.5 Hz, 1H), 7.49 (d, J: 8.9 Hz, 2H), 6.79 (d, J: 8.9 Hz, 2H), 4.39-4.36 (m, 1H), 4.32-4.29 (m, 1H), 4.13-4.09 (m, 1H), 4.02-3.98 (m, 1H), 3.94-3.91 (m, 1H), 3.03 (s, 6H), 2.63 (t, J: 7.3 Hz, 4H), 2.58 (t, J: 7.3 Hz, 4H), 2.49-2.35 (m, 16H), 2.26 (s, 3H), 2.24 (s, 3H), 2.21-2.15 (m, 1H), 2.13-2.08 (m, 1H)

^{13}C NMR (150 MHz, $CDCl_3$) δ 172.3, 151.1, 148.6, 146.1, 135.9, 128.2, 126.0, 125.7, 125.5, 125.1, 112.7, 67.4, 62.1, 55.3, 53.5, 52.9, 46.2, 40.5, 35.7, 32.3, 31.2

HRMS (ESI-TOFMS) calc. mass ($C_{34}H_{51}N_6O_6$)+ $[M+H]^+$ 639.3865 g/mol, experimental mass $[M+H]^+$ 639.3868 g/mol, delta ppm: 0.5

3.6.9 Photochemical synthesis of 3a

A round bottom flask was charged with **3** (8.7 mg, 0.0136 mmol) and dissolved in CH_2Cl_2 (6 x 10-5 M). The flask was wrapped in foil and the light was directed into the flask from the top via a light guide. The solution was irradiated with visible light (λ_{ex} = 400-500 nm, 0.18 W, 0.21 W/cm^2) for 2 h and 20 min, at which point the orange solution was concentrated. The crude orange oil was purified by silica gel column chromatography (4 g column, gradient 50% $\rightarrow$ 100% MeOH in CH_2Cl_2) to yield the title compound **3a** as yellow/orange oil (1 mg, 0.0021 mmol, 15%) along with unreacted starting material 3 (1.2 mg, 0.0019

mmol, 14%). Orange material, likely **3b**, remained on the column.

^{1}H NMR (600 MHz, $CDCl_3$) (3a) δ 8.03 (d, J: 8.6 Hz, 1H), 7.58 (dd, J: 2.1, 8.6 Hz, 1H), 7.53 (d, J: 8.9 Hz, 2H), 7.42 (d, J: 2.1 Hz, 1H), 6.78 (d, J: 8.9 Hz, 2H), 5.26 (s, 1H), 5.10 (s, 1H), 4.22 (t, J: 6.6 Hz, 2H), 3.03 (s, 6H), 2.76 (t, J: 6.6 Hz, 2H), 2.63 (t, J: 7.3 Hz, 2H), 2.42 (t, J: 7.3 Hz, 2H), 2.48-2.38 (m, 8H), 2.25 (s, 3H)

HRMS (ESI-TOFMS) calc. mass ($C_{26}H_{35}N_4O_4$)+ $[M+H]^+$ 467.2653 g/mol, experimental mass $[M+H]^+$ 467.2656 g/mol, delta ppm: 0.6

3.6.10 Hairless mouse skin preparation

Hair removal cream (Nair) was spread over the entire dorsal and ventral area of the mouse (Balb/C). After 5 min the cream/hair was gently removed using a paper towel. The mouse was euthanized by CO_2 asphyxiation followed by cervical dislocation. To remove the skin, a superficial longitudinal cut was made along the ventral side from the posterior to the anterior end, and the skin was peeled down to the tail and subsequently cut off the mouse and placed in a 50 mL polypropylene tube filled with PBS until it was mounted (**Figure 3.10**). The skin was mounted on the same day of skin removal. A glass objective cover slip (Fisher Brand #1.5, 24 x 60 x 0.17 mm) was taped into a cardboard frame (cut to fit: 51 x 79 mm, with a 20 x 53 mm window). Hairless mouse skin was cut to fit a cover slip using a razor blade and placed on top of the cover slip previously wetted with PBS. The

mouse skin was further wetted with PBS and a second coverslip was placed over the skin. The edges were dried with a paper towel and the cover slip was taped into using paper tape. Air bubbles were pressed out before the sample was completely sealed. Irradiation experiments using the mouse skin tissue filter were performed on the same day as tissue collection.

3.6.11 Irradiation studies of polymer 1 through mouse skin tissue filter

Aliquots of a solution of polymer **1** in CH_2Cl_2 (0.04 mg/mL, 10 mL) were transferred to a quartz micro cuvette (0.04 mg/mL, 0.5 mL) and used for the corresponding experiment. The initial absorbances of the polymer **1** samples were measured by UV-vis spectroscopy. The samples were subsequently irradiated directly or through the tissue filter for 15 min with visible light (λ_{ex} = 400-500 nm, 0.18 W, 0.21 W/cm^2) and the changes in absorbance were monitored at regular intervals over time. The tissue filter was attached to the cuvette holder using tape and the light beam was focused on the cuvette (**Figure 3.11**). To quantify reaction completion, those samples that did not reach completion were further irradiated directly with visible light. Irradiation power was measured before and after passage through glass and the glass/mouse skin tissue filter (**Table 3.1**).

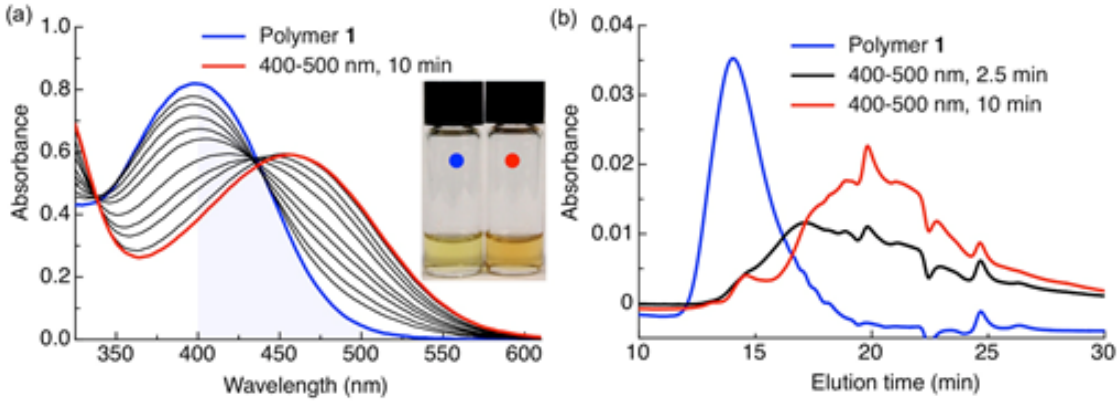

Figure 3.3: Polymer **1** photodegrades upon irradiation with visible light in hydrophobic environment. (a) Spectral changes in the UV-Vis spectrum of polymer 1 irradiated in CH_2Cl_2 (0.04 mg/ml, 0.5 ml) with visible light (λ_{ex} = 400-500 nm, 0.18 W, 0.21 W/cm^2). The blue shaded area highlights visible light absorption. Inset: color change following complete photoconversion. (b) GPC chromatogram of polymer **1** before (blue trace, Mw = 31.7 kDa, PDI = 2.7, PMMA standard) and after irradiation in CH_2Cl_2 (0.04 mg/ml, 0.5 ml) with visible light (λ_{ex} = 400-500 nm, 0.18 W, 0.21 W/cm^2) for 2.5 min (black trace) and 10 min (red trace). Absorbance sampled at 300 nm; peak at 24 min is the toluene internal standard.

Table 3.1: Light power attenuation by glass slides and glass/mouse skin

Wavelengths	Initial power	Power after penetrating two glass cover slips	Power after penetrating glass and mouse skin
400-500 nm	0.18 W	0.15 W	0.03 W

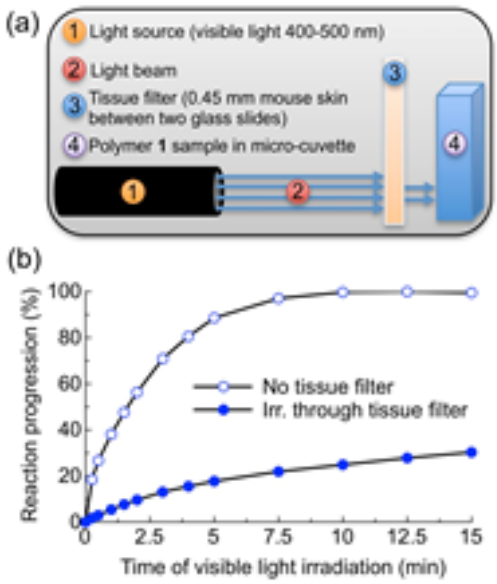

Figure 3.4: Visible light triggers polymer 1 photochemistry after passage through mouse skin. (a) Experimental setup. (b) Reaction progression of CH_2Cl_2solutions of polymer **1** (0.04 mg/ml, 0.5 ml) as they are irradiated directly (open circles) or through mouse skin (solid circles) with visible light (λ_{ex} = 400-500 nm, 0.18 W, 0.21 W/cm^2). The photoreactions were monitored by UV-Vis spectroscopy; the skin-attenuated reaction was further irradiated directly to fully react the polymer. Reaction progression (RP) was calculated by the following formula: $RP = ((A - A_{min})/(A_{max} - A_{min})) * 100\%$, where A is the absorption at 490 nm, Amin the absorbance at 0 min, and Amax the maximum absorbance after complete photoreaction.

3.6.12 Formulation of P-1-NR by electrospray

Polymer **1** (10 mg) and Nile red (1 mg, 10% w/w) were dissolved in $CHCl_3$ (0.200 mL) and diluted with DMF (0.05 mL). The resulting solutions were taken up in a 1 mL syringe equipped with a Teflon tube and a 25-gauge blunt needle, which was then placed in a syringe pump (KD Scientific) and connected to a high voltage power supply (Gamma High Voltage, ES30). The mixture was electrosprayed at 25 kV at a flow rate of 0.2 mL/hr. Samples were collected onto glass slides on an aluminum foil-covered aluminum plate collector connected to the power supply (ground) at a distance of 25 cm from the needle. Particles (0.8-1 mg/slide) were removed from the slides by scraping with a spatula into PBS containing 1% w/v Pluronic F127 (50 mL, 37 °C) followed by sonication. Particles were centrifuged (5250 rpm, 15 min), supernatant (45 mL) was removed, and particles were re-dispersed in new solvent by sonication. This washing procedure was repeated twice more to finally disperse the particles in 5 mL of solvent. The glass slide was weighed before and after removal of particles to calculate the mass of particles collected. Particle morphology was examined by SEM and release behavior was examined by fluorescence spectroscopy and by centrifuging the particles after irradiation to quantify release. Characteristic SEMs of the electrosprayed Nile red-loaded particles before and after irradiation are shown in **Figure 3.12**.

3.6.13 Encapsulation efficiency of Nile red

The amount of Nile red incorporated into the particle samples was determined using UV-vis spectroscopy. Two samples of P-**1**-NR (0.22 mg/ml, 0.25 ml) were concentrated, dried, and dissolved in $CHCl_3$ (1 mL). The absorbances at 542 nm of the two samples were measured and the dye concentration was quantified by linear calibration against solutions of known Nile red concentration (Y = 33613X, $R^2 = 0.998$). The concentration of Nile red in the photoresponsive particle P-**1**-NR was determined to be 5.6% w/w.

3.6.14 Nile red release experiments from P-1-NR

Six samples of P-**1**-NR (0.08 mg/ml, 0.5 ml) in PBS (1X, pH = 7.4) containing 1% w/v Pluronic F127 were prepared in plastic UV-vis cuvettes that were capped and subsequently sealed with parafilm. Fluorescence spectra of all samples were recorded before irradiation ($\lambda_{ex} = 550 \pm 1.5$ nm). Following irradiation with visible light (λ_{ex} = 400-500 nm, 0.18 W, 0.21 W/cm^2), fluorescence was recorded at regular intervals, as was that of control samples stored at ambient temperature wrapped in foil. After 90 min of irradiation, samples and controls were transferred to 1.5 mL centrifuge tubes and centrifuged (13500 rpm, 15 min) to separate particles from solvent and released payload. Supernatants and pellets were concentrated, dried overnight under vacuum, dissolved in $CHCl_3$ (0.5 mL), and the fluorescence of each sample was measured in a micro quartz cuvette. To compare

the relative amount of released Nile red versus the amount retained inside particles, the fluorescence intensity at 588 nm of both the pellet and supernatant for each sample was measured and the percentage of Nile red released or retained was calculated by the following formula: released Nile red = ($F_{supernatant}$/($F_{supernatant}$+ F_{pellet}))*100.

Formulation of P-**1**-Dex by electrospray

Polymer **1** (10 mg) particles containing dexamethasone (2 mg, 20% w/w) and IR780 (0.01 mg, 0.1% w/w) were formulated as above, with the following variations: $CHCl_3$ (0.200 mL)-dissolved samples were diluted with DMSO (0.075 mL), voltage was 28 kV, and the flow rate was 0.1 mL/hr. Characteristic SEM of the electrosprayed Dex-loaded particles (P-**1**-Dex) is shown in **Figure 3.13**. The volume of the particle dispersion was subsequently adjusted by centrifugation to yield a final concentration of 8 mg/mL for use in animal experiments. Freshly suspended particles were used for each experiment.

3.6.15 Encapsulation efficiency of dexamethasone by HPLC

The amount of dexamethasone incorporated into particles was determined using HPLC-MS chromatography. A P-**1**-Dex sample (0.8 mg) was dispersed in PBS (40 mL) by sonication and centrifuged (5250 rpm, 15 min). The pellet was washed three times in PBS (40 mL) and dissolved in $CHCl_3$ (5 mL, 0.16 mg/mL). An aliquot (1.5 mL) was dried and dissolved in MeOH (0.5 mL) (requiring son-

ication, heating in a water bath and a second sonication, as polymer **1** does not dissolve appreciably). The MeOH dispersion was spun through a 3k spin-filter (13.4 krpm, 15 min) and an HPLC filter and run on the HPLC (5 μL injection). The absorbance of dexamethasone at 254 nm was compared to known concentrations of dexamethasone and the loading was determined to be 1% w/w.

3.6.16 *In vivo* release of dexamethasone

The protocol was approved by the IACUC committee at the University of California San Diego. C57BL/6 male mice (purchased from Harlan Sprague Dawley, San Diego, CA, USA) weighing 25-30 g were housed according to NIH guidelines for 3 d prior to experiments to acclimatize to laboratory conditions. Animals were randomly divided into 7 groups: P-**1**-Dex+light (200 μg, 2 μg Dex), P-**1**-Dex (200 μg, 2 μg Dex), DPBS, DPBS+light, Dex (2 μg), P-**1** (200 μg) and pre-irradiated P-**1** (200 μg); n=3 for each group except DPBS, for which n=6. Formulations in 25 μL DPBS were injected in the skin area subcutaneously just above the hock of the left hind paw 1 h before carrageenan injection (see Figure S9a). Injections were performed in lightly anesthetized (isoflurane) animals using a 50 μL gas-tight Hamilton syringe (#705) with a 31-gauge needle.

Acute inflammation was produced by injecting 25 μL of 2% (w/v) carrageenan (lambda form) solution in DPBS into the sub-plantar region (3 mm deep) of the left hind paw 1 h after administration of polymeric particles or con-

trol formulations. The right control hind paw footpad was injected with 25 μL DPBS. After carrageenan injection, treated paws of mice in the P-**1**-Dex+light and DPBS+light groups were exposed to light while mice were under light anesthetia (isoflurane) for 40 min (see **Figure 3.16b**). Light exposures were alternated with 20 min of free activity where the mouse was allowed to move around the cage and eat and drink.

For all groups, hind paw thickness was measured at 0, 1, 2, 3, 4, 5, 6, 7 and 8 h with a digital caliper (No. 547-526, Mitutoyo) (see **Figure 3.16c**). Each paw was measured 4 consecutive times at each time point and these values were then averaged to ensure accurate data. Paw thickness increases were calculated by subtracting the thickness of the right non-inflamed control paws. Hind paw thickness measurements were performed on the conscious mouse.

3.6.17 Cytotoxicity assay

P-**1** and pre-irradiated P-**1** (irr. 90 min in DPBS) in DPBS (4 mg/mL) and polymer 1 and pre-irradiated polymer 1 (irr. 90 min in CH_2Cl_2) in sterile DMSO (4 mg/mL) was prepared. The stock samples were diluted to the indicated concentrations in Dulbecco's modified eagle serum (DMEM) media without phenol red (990 μL, Invitrogen) supplemented with 10% fetal bovine serum (FBS, HyClone). Raw 264.7 cells were seeded on a tissue culture-treated 96-well plate

(Corning, USA) at a density of 20,000 cells/well in DMEM media. The cells were washed twice with 100 μL PBS at 37 °C using a multichannel pipette and incubated with the polymer suspensions in triplicate for 24 h at 37 °C and 5% CO_2, and again washed twice with 100 μL PBS. Cells were then incubated with the MTT reagent for 3 h and formazan crystals were solubilized according to the assay instructions (Life Technologies). 1% Triton-X was used as a positive apoptosis control. To quantify mitochondrial activity, absorbance at 570 nm normalized to background absorbance at 690 nm was measured using a SpectraMax M5 plate reader (Molecular Devices).

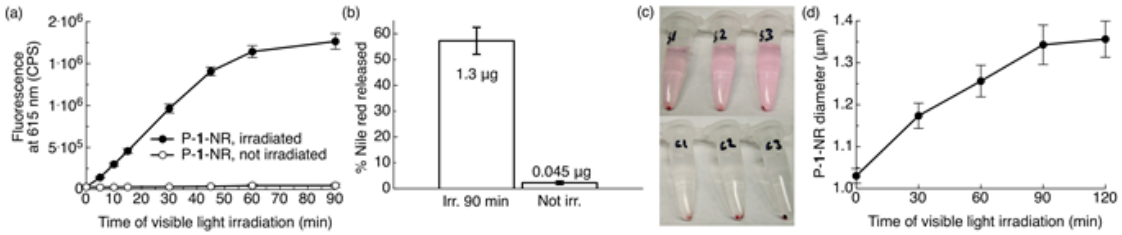

Figure 3.5: Photo-triggered release of Nile red from photoexpansile polymer **1** particles (P-**1**-NR). P-**1**-NR (0.08 mg/mL, 0.5 mL, total amount Nile red per sample: 2.25 μg) in PBS (1X, pH = 7.4) containing 1% w/v Pluronic F127 were irradiated in ambient temperature with visible light (λ_{ex} = 400-500 nm, 0.18 W, 0.21 W/cm^2) or kept in the dark for the same time. (a) Changes in fluorescence intensity at 615 nm (n=3). (b) Relative and actual amount of Nile red released from the same samples after 90 min of visible light irradiation (see supplementary information for calculation). (c) Photographs illustrating Nile red (pink) release from the samples/controls in (a, b) after 90 min of irradiation and after centrifugation (S1-3 = irradiated samples, C1-3 = non-irradiated controls kept in the dark). (d) Changes in particle diameter upon irradiation with visible light (Multisizer; n=3).

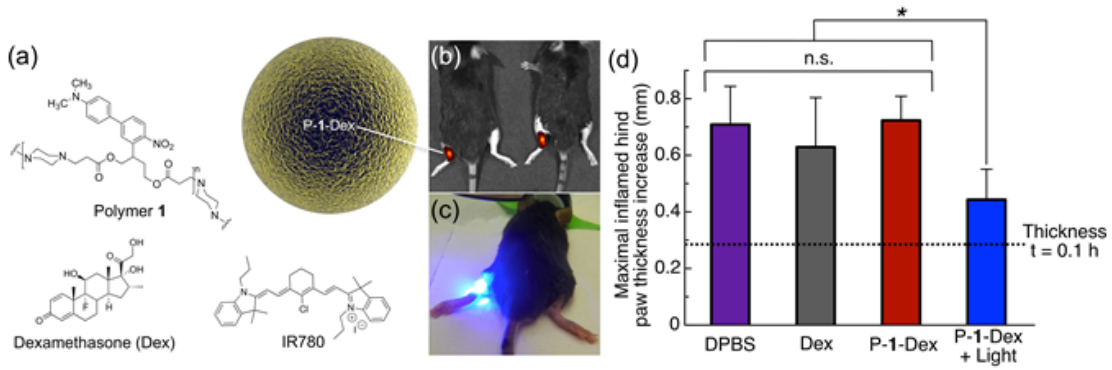

Figure 3.6: One-photon visible light photo-release of dexamethasone from an implanted depot reduces carrageenan-induced hind paw inflammation in mice. (a) Composition of P-**1**-Dex particle depot. (b) Representative IVIS image of mice implanted with NIR fluorescent P-**1**-Dex depot before irradiation. (c) Photograph illustrating irradiation of the P-**1**-Dex depot with blue visible light (λ_{ex} = 400-500 nm, 0.18 W, 0.21 W/cm^2, 432 J/h). (d) Maximal inflamed hind paw thickness increase at t = 5 h after carrageenan injection. The P-**1**-Dex dose was 200 μg containing 2 μg Dex; free Dex dose was 2 μg; all mice were injected with a total of 25 μL of solution. n=3 for all groups except DPBS, for which n=6. Drug depots were injected in the left hind hock 1 h before inflammation was induced with carrageenan (2% w/v in 25 μL DPBS) in the left hind footpad. Hind paw thickness was measured using a caliper (see **Figure 3.16**) and the results are plotted relative to the non-inflamed right hind paw (injected at the same time with DPBS). Error bars are standard error of mean; *p = 0.02, n.s. = not statistically significant.

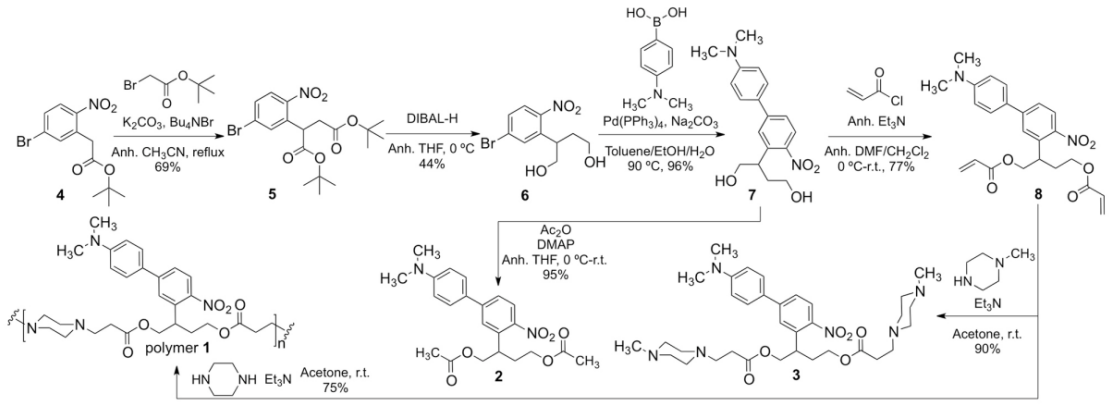

Figure 3.7: Synthesis of polymer **1** and model compounds **2** and **3**.

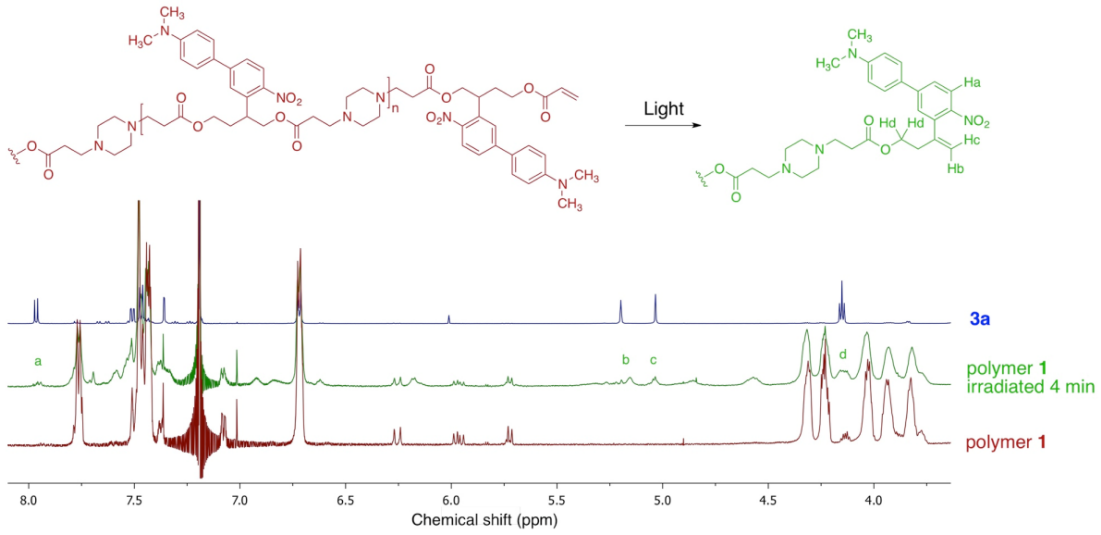

Figure 3.8: ^{1}H NMR spectroscopic analysis of polymer **1** upon irradiation in $CDCl_3$ (3 mg/mL, 0.55 mL) reveals the initial formation of the photo-unstable nitro-alkene photoproduct, as compared to the spectra of **3a**. Upon prolonged irradiation a precipitate was formed in the NMR tube, which is why the peaks decrease in intensity and broaden. Secondary photoproducts are also produced due to the photo-instability of the nitro-alkene photoproduct and competing photoreactions (see **Figure 3.2c-d**).

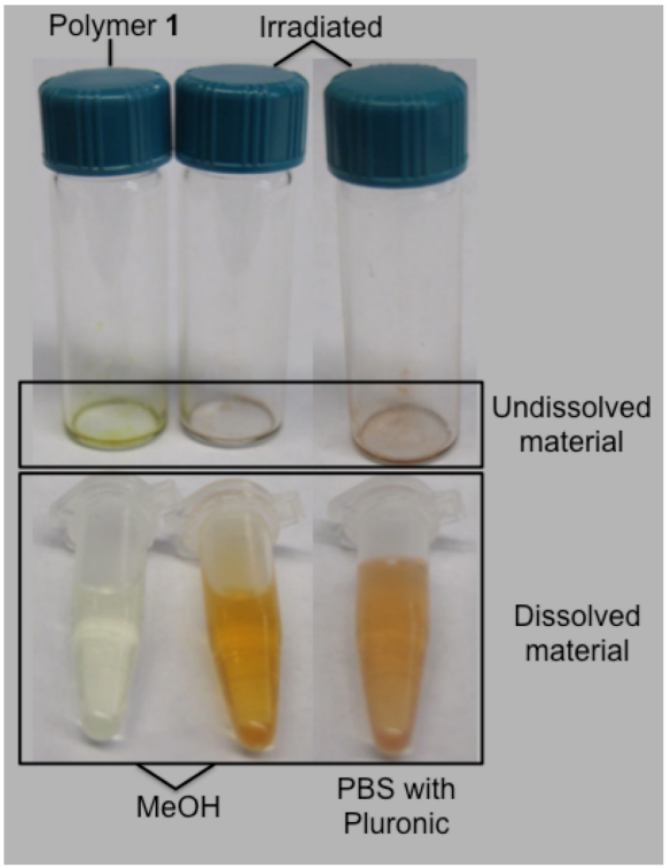

Figure 3.9: Polymer **1** becomes soluble in MeOH upon complete photoconversion (middle) in CH_2Cl_2 (6 x 10-5 M). Left, unirradiated polymer. The photoproducts are also partially soluble in water containing 1% w/v Pluronic F127 (right panel).

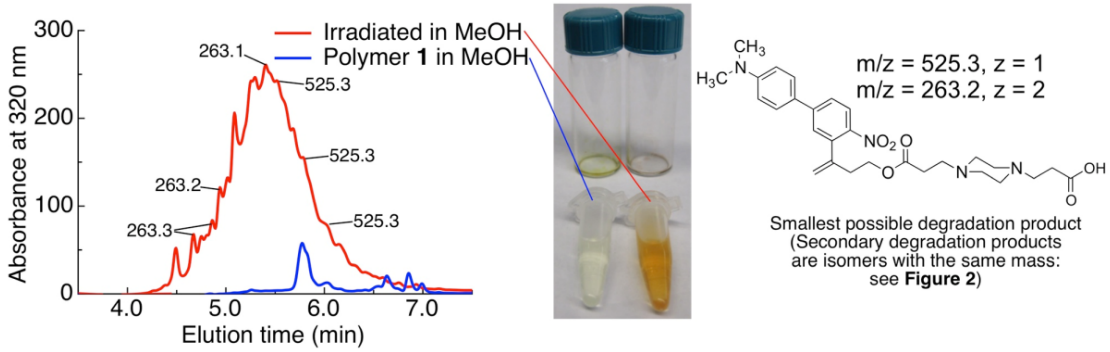

Figure 3.10: Polymer **1** photodegrades into smaller molecules upon irradiation in CH_2Cl_2. HPLC-MS analysis of MeOH-soluble material from **Figure 3.9**. Masses correspond to the mass of the smallest theoretical segment anticipated. However, the peaks do not correspond to the structure, as this photo-unstable product is further photodegraded into multiple isomers with the same mass (see **Figure 3.2c-d**).

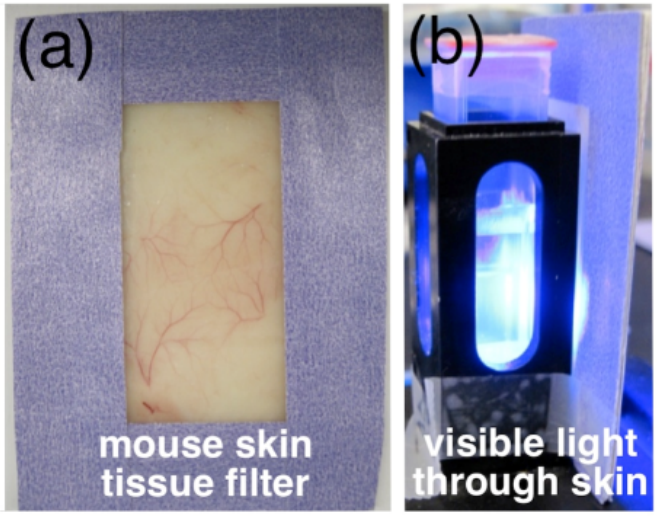

Figure 3.11: Visible light penetrates mouse skin. (a) Tissue filter (0.45 mm mouse skin between two glass coverslips). (b) Visible light irradiation through the tissue filter.

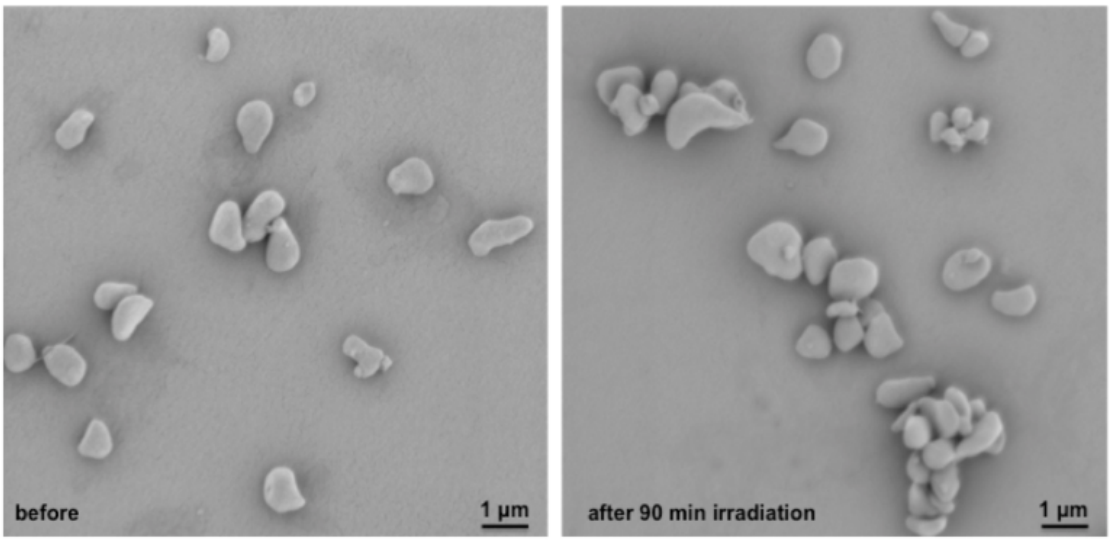

Figure 3.12: Representative SEM images of P-**1**-NR before (left) and after (right) 90 min of visible light irradiation.

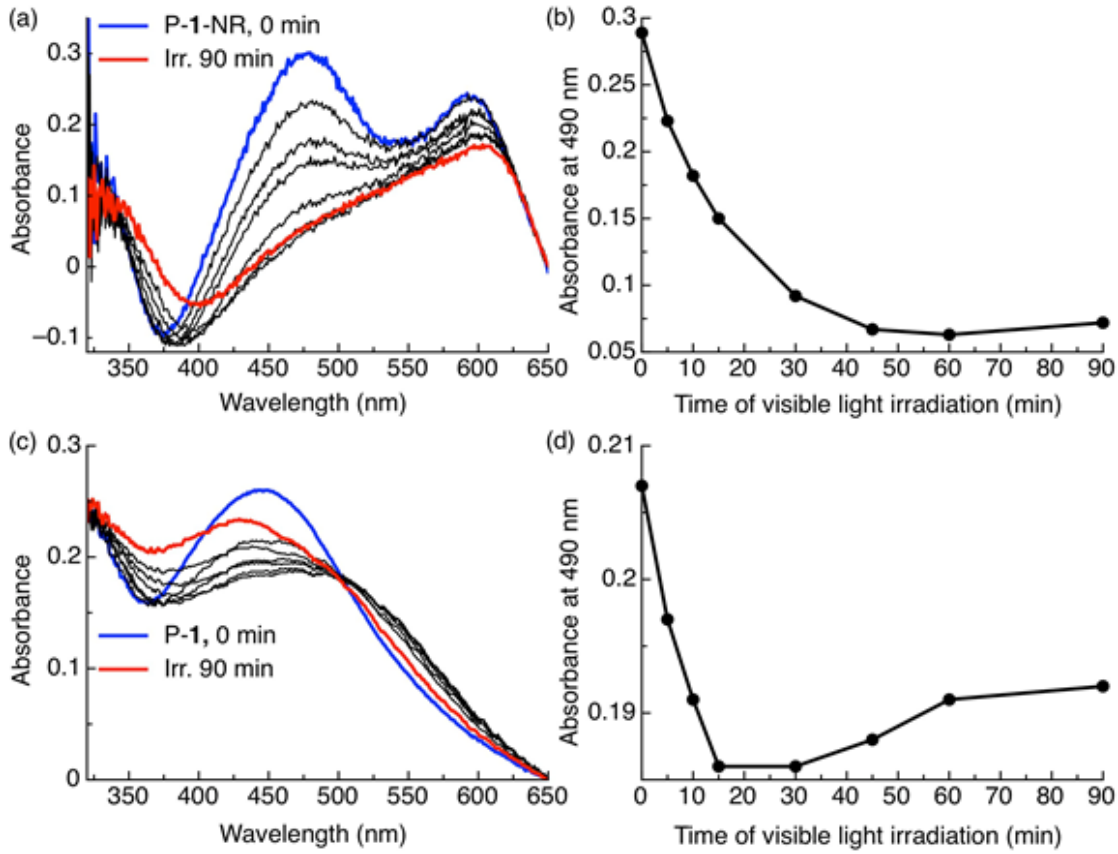

Figure 3.13: Particle photolysis. (a) Changes in the UV-Vis spectra of P-**1**-NR (0.08 mg/ml, 1 ml) in water as it is irradiated with visible light (λ_{ex} = 400-500 nm, 0.18 W, 0.21 W/cm^2). (b) Changes in absorbance at 490 nm of P-**1**-NR over time as it is irradiated with visible light. (c) Changes in the UV-Vis spectra of P-**1** (0.08 mg/ml, 1 ml) in water as it is irradiated with visible light (λ_{ex} = 400-500 nm, 0.18 W, 0.21 W/cm^2). (b) Changes in absorbance at 490 nm of P-**1** over time as it is irradiated with visible light.

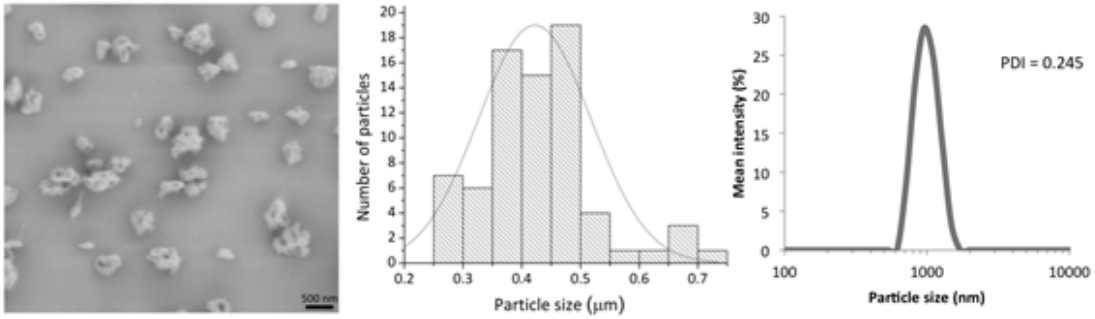

Figure 3.14: Representative SEM image of P-**1**-Dex and size distribution from SEM (middle graph) and DLS (right graph).

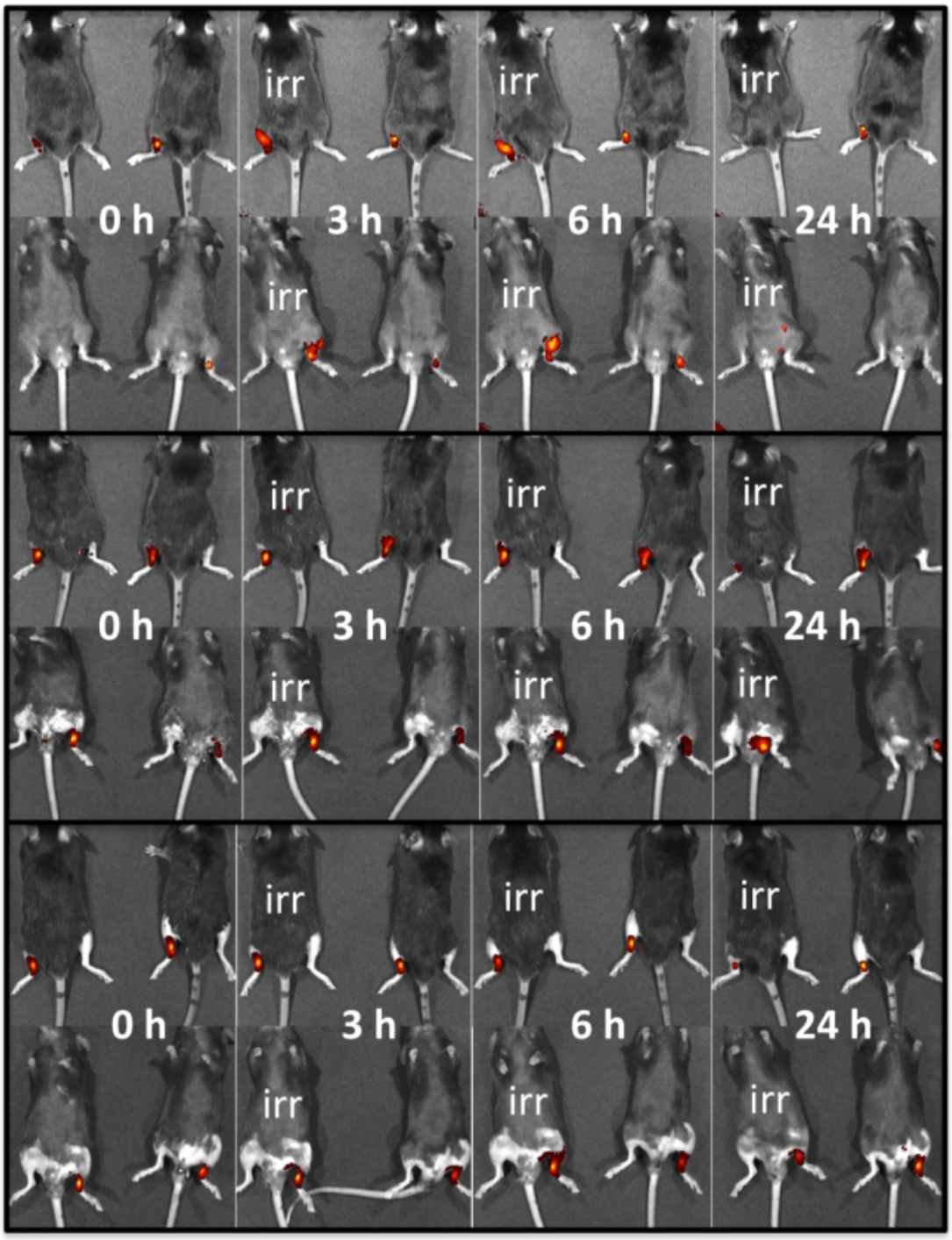

Figure 3.15: Distribution of NIR fluorescent depots in P-**1**-Dex+light (1 mark on tail) and P-**1**-Dex (3 marks on tail) mice (3 mice per group) over time as visualized by IVIS imaging (λ_{ex} = 780 nm, λ_{em} = 800 nm)

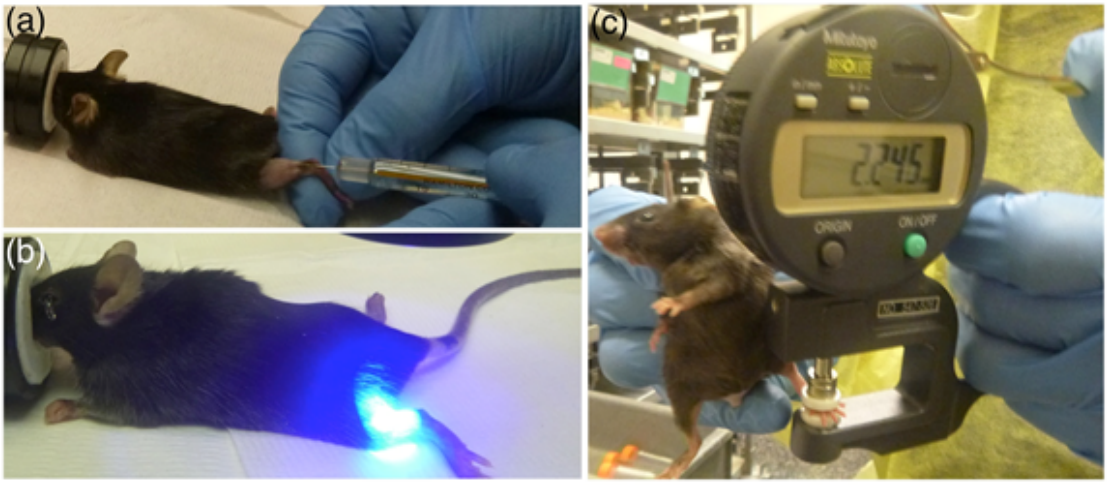

Figure 3.16: *In vivo* procedures. (a) Injection of the P-**1**-Dex depot in the hind hock. (b) Irradiation of the depot. (c) Measurement of the hind paw using a caliper.

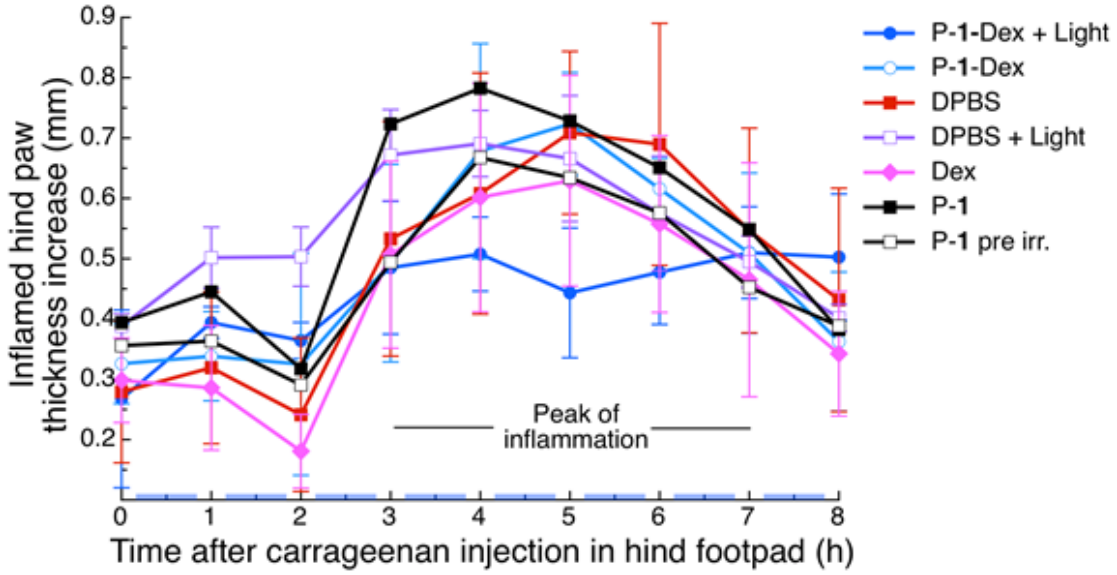

Figure 3.17: Inflamed hind paw thickness over time of all experimental groups. The skin just above the left hind hock was injected subcutaneously with the indicated solution (25 μL; the P-**1**-Dex dose was 200 μg containing 2 μg Dex; free Dex dose was 2 μg; P-1 dose was 200 μg). n=3 for all groups except DPBS, for which n=6. Materials were injected 1 h before injection of carrageenan (2% w/v in 25 μL DPBS) in the left hind footpad. Hind paw thickness increases are relative to non-inflamed right hind paws (injected with 25 μL DPBS). P-**1**-Dex + Light and DPBS + Light mice were irradiated 40 min per hour throughout the experiment as indicated by the blue boxes. Error bars are standard error of mean.

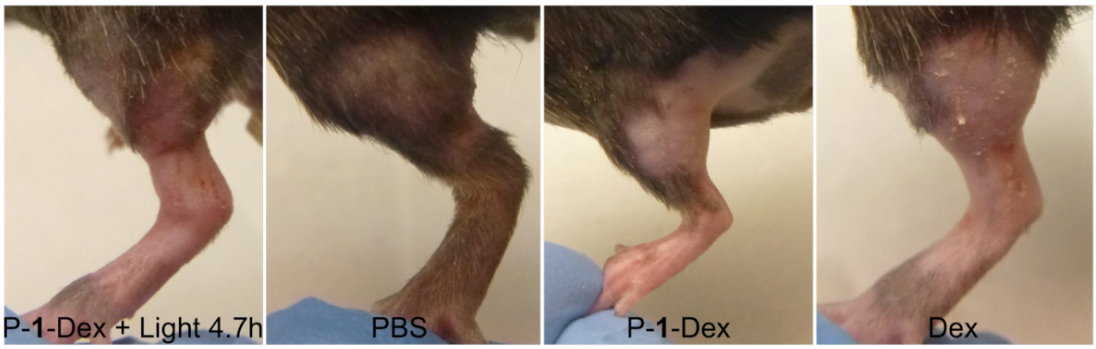

Figure 3.18: Representative photographs of mice 24 h after injection of carrageenan.

Figure 3.19: Oedema in DPBS + Light mouse after light exposure for 3 h. Swelling resolved within 1 d.

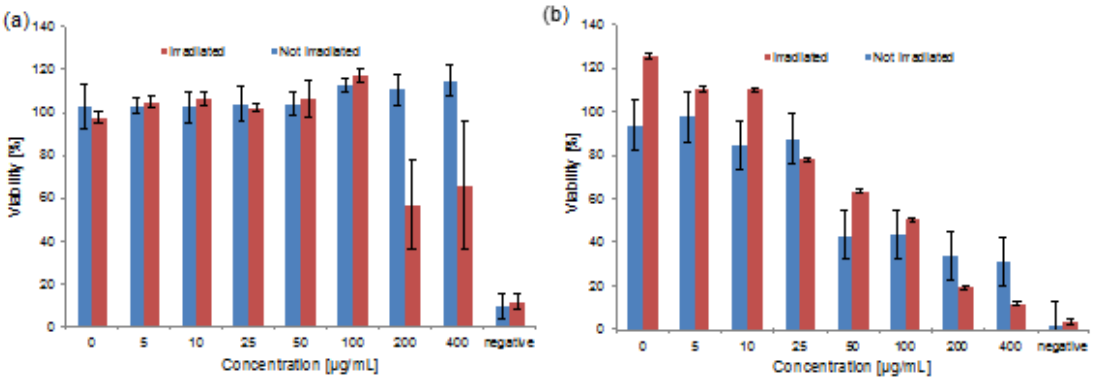

Figure 3.20: Effects of P-**1** and polymer **1** on cell metabolism in Raw 264.7 mouse macrophages by MTT assay. (a) P-**1** before and after irradiation (90 min). (b) Polymer **1** before and after irradiation (90 min).

3.7 References

(1) K. Deisseroth, *Nature Methods*, 2011, **8**, 26–29.

(2) N. Fomina, J. Sankaranarayanan and A. Almutairi, *Advanced Drug Delivery Reviews*, 2012, **64**, 1005–1020.

(3) P. Klan, T. Solomek, C. G. Bochet, A. Blanc, R. Givens, M. Rubina, V. Popik, A. Kostikov and J. Wirz, *Chemical Reviews*, 2013, **113**, 119–191.

(4) A. P. Goodwin, J. L. Mynar, Y. Z. Ma, G. R. Fleming and J. M. J. Frechet, *Journal of the American Chemical Society*, 2005, **127**, 9952–9953.

(5) M. L. Viger, M. Grossman, N. Fomina and A. Almutairi, *Advanced Materials*, 2013, **25**, 3733–3738.

(6) M. K. G. Jayakumar, N. M. Idris and Y. Zhang, *Proceedings of the National Academy of Sciences of the United States of America*, 2012, **109**, 8483–8488.

(7) M. L. Denton, M. S. Foltz, L. E. Estlack, D. J. Stolarski, G. D. Noojin, R. J. Thomas, D. Eikum and B. A. Rockwell, *Investigative Ophthalmology & Visual Science*, 2006, **47**, 3065–3073.

(8) Q. N. Lin, Q. Huang, C. Y. Li, C. Y. Bao, Z. Z. Liu, F. Y. Li and L. Y. Zhu, *Journal of the American Chemical Society*, 2010, **132**, 10645–10647.

(9) Q. N. Lin, C. Y. Bao, Y. L. Yang, Q. N. Liang, D. S. Zhang, S. Y. Cheng and L. Y. Zhu, *Advanced Materials*, 2013, **25**, 1981–1986.

(10) J. Olejniczak, J. Sankaranarayanan, M. L. Viger and A. Almutairi, *Acs Macro Letters*, 2013, **2**, 683–687.

(11) M. Frasconi, Z. C. Liu, J. Y. Lei, Y. L. Wu, E. Strekalova, D. Malin, M. W. Ambrogio, X. Q. Chen, Y. Y. Botros, V. L. Cryns, J. P. Sauvage and J. F. Stoddart, *Journal of the American Chemical Society*, 2013, **135**, 11603–11613.

(12) L. Donato, A. Mourot, C. M. Davenport, C. Herbivo, D. Warther, J. Leonard, F. Bolze, J. F. Nicoud, R. H. Kramer, M. Goeldner and A. Specht, *Angewandte Chemie-International Edition*, 2012, **51**, 1840–1843.

(13) M. A. Azagarsamy, D. L. Alge, S. J. Radhakrishnan, M. W. Tibbitt and K. S. Anseth, *Biomacromolecules*, 2012, **13**, 2219–2224.

(14) D. Woll, J. Smirnova, M. Galetskaya, T. Prykota, J. Buhler, K. P. Stengele, W. Pfleiderer and U. E. Steiner, *Chemistry-a European Journal*, 2008, **14**, 6490–6497.

(15) S. Chakraborty, I. C. Liao, A. Adler and K. W. Leong, *Advanced Drug Delivery Reviews*, 2009, **61**, 1043–1054.

(16) S. Tsurufuji, K. Sugio and F. Takemasa, *Nature*, 1979, **280**, 408–410.

(17) C. J. Morris, *Methods Mol Biol*, 2003, **225**, 115–21.

Chapter 4

Drug depot responsive to recurrence of pathological angiogenesis for long-term management of retinal vascular disorders

4.1 Abstract

Purpose: Treatment of pathological angiogenesis with anti-angiogenic drugs currently requires repeated injections. As the pathophysiology of these diseases involves oxidative stress (ROS), we are examining whether delivering EYLEA in nanoparticles that degrade and release cargo in response to hydrogen peroxide lengthen its lifetime in the eye. This approach should tailor the amount of drug released to the progression of the disease, especially in its long-term management.

Methods: The efficacy of EYLEA in the following formulations are being compared in mice with oxygen-induced retinopathy (OIR) and with laser-induced choroidal neovascularization (CNV): in peroxide-sensitive polymer (PSP) particles, slowly-degrading particles comprised of poly(lactic-co-glycolic acid) (PLGA), and free drug. Avascular areas in OIR and CNV spot size measure therapeutic efficacy.

To assess lifetime, we examine whether EYLEA delivered up to three months prior to laser induction protects against CNV.

Results: PSP particles are compatible with intravitreal administration, as they have no effect on electroretinography, expression of inflammatory cytokines, or visual acuity up to 12 months following injection. EYLEA is effective in preventing neovascularization in OIR when administered as a free drug (40 μg) or in PSP, but not in PLGA. PSP particles are also effectively releasing EYLEA that inhibits choroidal neovascularization in animals injected three months prior to the insult.

Conclusions: EYLEA retains activity upon formulation in particles by nanoemulsion. ROS-responsive particles allow greater release of EYLEA in eyes affected by neovascularization than PLGA particles.

Translational Relevance: The study presents a drug delivery system with potential to respond to recurrence of pathological angiogenesis.

4.2 Introduction

Angiogenesis is a natural process of formation of new blood vessels from pre-existing vascular network. Disrupted regulation of this process leads to severe loss of vision. This pathological angiogenesis is linked to a spectrum of disorders such as wet age-related macular degeneration (AMD), diabetic retinopathy, retinal vein occlusion (RVO), and retinopathy of prematurity (ROP). Among those, AMD is a leading cause of vision loss, accounting for over 8% of blindness worldwide[1,2]

and causes an estimated annual economic burden of $30 billion in the United States alone.[3] Even moderate AMD causes a 32% decrement in the quality of life of patients, comparable to that of patients with severe chest pain or fractured hip.[4] One of the most common treatments for neovascular AMD involves using a needle to directly deliver a dose of anti-VEGF (vascular endothelial growth factor) drugs, such as bevacizumab (Avastin), ranibizumab (Lucentis), and aflibercept (Eylea)[5] to the intravitreous space. Since the introduction of these injectable drugs for AMD in 2005,[6] the yearly frequency of this procedure in the US has increased from around 200,000 to over 4 million in 2013, and is expected to reach 6 million in 2016.[7,8] This number is expected to further increase based on the growing pipeline of novel injectable drugs for retinal disorders, such as lampalizumab (Roche) for geographic atrophy,[9,10] various angiopoietin (ANGPT/TIE2) pathway inhibitors,[11,12] and anti-PDGF (platelet-derived growth factor) molecules such as Fovista^{TM} (Ophthotech) for use in combination with anti-VEGF therapies.[13,14] The sheer number of time the IVT procedure is performed yearly, combined with the often complex logistics involved in getting the patients in and out of the clinic, cause a considerable burden to the patients, doctors and the medical system as a whole,[15].[16] Hence, strategies to reduce the frequency of injections while keeping the treatment effective are in great demand.

Much of the work aiming to reduce the number of injections was focused on optimizing the treatment regime, which led to the rise of pro re nata (PRN,

As-needed basis), and Treat-and-extend type of injection schedules.[17–19] Many ophthalmologists also developed their own treatment algorithms, which are continually refined as more long-term clinical data becomes available.[12,20] There is also a strong push to develop systems that extend the lifetime of anti-angiogenics following intravitreal injection, in a form of implants,[21–24] including micro-[25,26] and nanoparticles,[27,28] as well as hydrogels,[29,30] and even cellular reactors.[31] In addition to these near zero-order kinetics systems, there exists a limited amount of reports on on-demand drug delivery systems for intraocular drug delivery, such as the refillable MicroPump device with programmable drug release rates by Replenish Inc.,[32,33] and a light-actuated intravitreal polymeric depot.[34]

All the above approaches have either a pre-set release profile based on the composition of the materials used, and require external intervention (invasive or non-invasive) to deliver the additional dose of drug. In this study, based on recent advances in disease-responsive materials,[35,36] we propose an inflammation-triggered intraocular depot that is able to react and release therapeutics during the recurrence of the disease state.

4.3 Materials and Methods

All chemicals were purchased from Sigma-Aldrich (St. Louis, MO) unless otherwise stated. Likewise, buffers and bio-assay agents were acquired from Thermo Fisher Scientific (Carlsbad, CA). All animal experiments were approved

by the UC San Diego Institutional Animal Care and Use Committee (IACUC), and adhered to the ARVO Statement for the Use of Animals in Ophthalmic and Vision Research.

4.3.1 Nanoparticle formulation

PSP was synthesized as previously published[37] (MW 60 kDa, PDI 1.3 by gel permeation chromatography). Samples were kept ice-cold during formulation by a double-emulsion protocol. Polymer (10 mg) was dissolved in 270 μL dichloromethane (DCM) containing Span 80 (sorbitan monooleate, 6 mg), 30 μL aflibercept (20 mg/mL; EYLEA, Regeneron) was added, and the mixture was sonicated in a bath sonicator (Misonix S-4000, Qsonica, Newtown, CT) for 1 min total (30 s ON/30 s OFF/30 s ON) at 20 W. The primary emulsion was then added to 6 mL of sterile-filtered polyvinyl alcohol (PVA, 1% w/v in PBS), and probe sonicated for 4 min at 10 W to form the secondary emulsion. DCM was evaporated under house vacuum conditions while stirring at 600 RPM for 4 h in an ice-water bath. Remaining PVA was removed by tangential cross-flow filtration (Pellicon XL 500 kDa, Millipore), eluting with 250 mL PBS at 45 RPM. The retentiate was then freeze-dried to yield nanoparticle powder. Nanoparticle size and distribution were analyzed by dynamic light scattering (DLS, Zeta Nanosizer, Malvern Instruments) and scanning electron microscopy (SEM, FE-SEM 8500, Agilent). Buffer containing the drug was replaced by 30 μL PBS for empty particles

preparation. To formulate fluorescent particles for retention studies, PSP was conjugated with NHS-Rhodamine, and the internal aqueous phase was replaced with 30 μL PBS containing Ovalbumin, Alexa Fluor 488 Conjugate (20 mg/mL). PLGA (ester-terminated, 24-38 kDa) was used as a model slowly hydrolyzing polymer.

4.3.2 Quantification of aflibercept encapsulation and activity

Aflibercept encapsulation was measured by a sandwich ELISA assay using an anti-human IgG (Fc specific; I2136, Sigma-Aldrich) antibody as capture, and anti-human sVEGF R2/KDR (DY357, 841244, R&D Systems) as detection antibody. ELISA plates (DY990, R&D Systems) were coated overnight at 4°C with the capture antibody in PBS (1:333 dilution, 250 μL/well).[38] Following the coating, sample addition and detection was carried out following kit instructions. Binding affinity of aflibercept released from nanoparticles was quantified following a published protocol.[39] Briefly, solutions of released aflibercept were added to 10 pM solutions of human VEGF (68-8784-63, eBioscience) and incubated overnight at room temperature. Unbound human VEGF was quantified using a human VEGF-specific ELISA kit (DVE00, R&D Systems). Long-term aflibercept release from particles was quantified using fluorescamine protein assay. Suspensions of particles (10 mg/mL) in PBS or PBS containing 500 μM H_2O_2 were incubated on a shaker at room temperature. At each time point, the suspensions were centrifuged (13000 rcf, 5 min), supernatant was collected and replaced with fresh buffer; fluorescamine

(3 mg/mL in DMSO) was then added in 3:1 ratio to the supernatants. Following a 15-min incubation in the dark, aflibercept concentration was measured by fluorescence spectroscopy ($\lambda_{ex}/\lambda_{em}$ = 365/470 nm, Horiba Jobin Yvon FL-1000).

4.3.3 Short-term therapeutic efficacy *in vivo*

Therapeutic potential of intravitreous (IVT) PSP-EY (EYLEA-containing PSP particles) was evaluated in murine oxygen-induced retinopathy (OIR) model in comparison to that of IVT EYLEA, PLGA-EY (EYLEA-containing PLGA particles), empty particle controls (PSP, PLGA), and saline. OIR model was realized according to previously published protocols.[40,41] Briefly, day 7 (P7) neonatal C57BL/6 mice were exposed to 75% oxygen atmosphere for 5 days. At P12, the animals were brought out to ambient conditions and were injected IVT with nanoparticles (PSP and PLGA, empty and containing 0.4 μg aflibercept), free aflibercept (0.4 μg), or PBS. To elucidate the degradation mechanism of PSP *in vivo*, P12 OIR mice were injected with PSP-EY in saline, and PSP-EY in saline containing 20 mM peroxide scavenger, N-Acetylcysteine (NAC) in the contralateral eye. After 5 days at ambient conditions, the animals were anesthetized by isoflurane and injected intravenously with 25 μL FITC-Dextran solution in PBS (50 mg/mL; 2 MDa). After 30 min, mice were euthanized, their eyes enucleated and fixed in 4% PFA for 1 h. Retinas were then flat-mounted and imaged with a fluorescence microscope (Biorevo BZ-X700, Keyence, Itasca, IL). Avascular and

neovascular areas were quantified in Adobe Photoshop CS2.

4.3.4 Delivery material biocompatibility

For short-term biocompatibility testing, healthy C57BL/6 mice (4-8 weeks, male) were injected IVT with PSP, PLGA nanoparticles (1 μL, 100mg/mL in PBS) or PBS, as well as same-age healthy controls (no injection, n = 3 eyes for each group). Animals were euthanized 7-days post-injection, their eyes were enucleated and retinas extracted. RNA extraction, reverse transcription, and qRT-PCR was carried out following previously reported protocol.[34] Each cDNA sample was run in duplicate and quantified by comparative CT algorithm. The average of two values was used in analysis. All gene expression levels were normalized to GAPDH. Mouse primer sequences for interleukin-1β (IL-1β), tumor necrosis factor-α (TNF-α), and glyceraldehyde 3-phosphate dehydrogenase (GAPDH) were obtained from literature, and confirmed using Primer-BLAST (NCBI, Table S1).

Rhodamine-labeled PSP nanoparticles were injected IVT for long-term retention and compatibility testing in healthy C57BL/6 mice. Following the injection, *in vivo* retinal imaging (Micron III, Phoenix Labs, Pleasanton, CA) and a suite of tests was performed longitudinally for up to 12 months. Bilateral Ganzfield full-field electroretinograms (ERGs) were taken following a previously reported protocol 34. Recordings were processed in Microsoft Excel. Retinal optical coherence tomographs (OCT) were taken using HRT3 Retina Module (Heidelberg,

Carlsbad, CA) with a 30° objective. The acquisition software was used to quantify total retinal layer thickness, as well as ONL thickness along the median sagittal cross-section of the eye.

One year post-implantation, in addition to the regular measurements, the animals were subjected to focal ERG (Micron III, Phoenix Labs, Pleasanton, CA) and optomotor response tests.[42] Results were compared to age-matched healthy controls.

Following the final *in vivo* safety testing, animals were euthanized, their eyes were enucleated and processed for histopathological analysis. Enucleated eyes were cleaned of the surrounding tissue and fixed for 24 h in Davidson's Fixative (Sigma-Aldrich), followed by 48 h incubation in sucrose (30% w/v in PBS). The ocular globe was then embedded in Tissue-Tek OCT Compound (Sakura Finetek) on dry ice and stored at -80 °C until cryosectioning. Frozen sections of 10 μm thickness were cut using a microtome-cryostat. Tissue slices were stained with hematoxylin and eosin (H&E). Mounted samples were imaged in bright-field microscope at 10x magnification (Biorevo BZ-X700, Keyence, Itasca, IL). Micrographs were quantified using Adobe Photoshop CS2.

4.3.5 Laser-induced choroidal neovascularization (CNV)

To evaluate long-term efficacy of PSP-EY in response to a angiogenic flare-up, healthy B6.CB17$^{Prkdcscid/SzJ}$ (B6 scid, 3-4 weeks old, male) were injected IVT

with PSP-EY, PLGA-EY, free EY and saline as control. Twelve weeks post-implantation, mice were subjected to laser-induced disruption of Bruch's membrane in both eyes using an OcuLight GL 532 nm laser photocoagulator (IRIDEX, Mountain View, CA) with a slit lamp delivery system. Four spots in the posterior pole of the choroid were irradiated through the dilated pupil (150 mW, 75 μm spot, 100 ms). One week following laser photocoagulation, the mice were anesthetized by isoflurane, and injected intravenously with 50 μL FITC-Dextran solution in PBS (50 mg/mL; 2 MDa). After 30 min, the mice were euthanized, their eyes collected and fixed in paraformaldehyde (4% in PBS) for 1h. Choroids were then flat-mounted and stained with Alexa Fluor 594-conjugated isolectin GS-IB4. Samples were mounted onto slides with VECTASHIELD Antifade Mounting Medium with DAPI (Vector Labs, Burlingame, CA). Slides were imaged at 10X magnification (Biorevo, Keyence), and images were quantified in Adobe Photoshop CS2. For short term validation of the model, CNV was induced first, followed by IVT injection with particles, PBS, and free drug (0.4 μg aflibercept/eye) as controls.

4.3.6 Analysis

ANOVA with Tukey post-hoc was used to investigate statistical significance of the OIR and CNV experiments (OriginPro, OriginLab). MannâĂŞWhitney U test was used to differentiate PSP and PBS in biocompatibility studies (OriginPro, OriginLab).

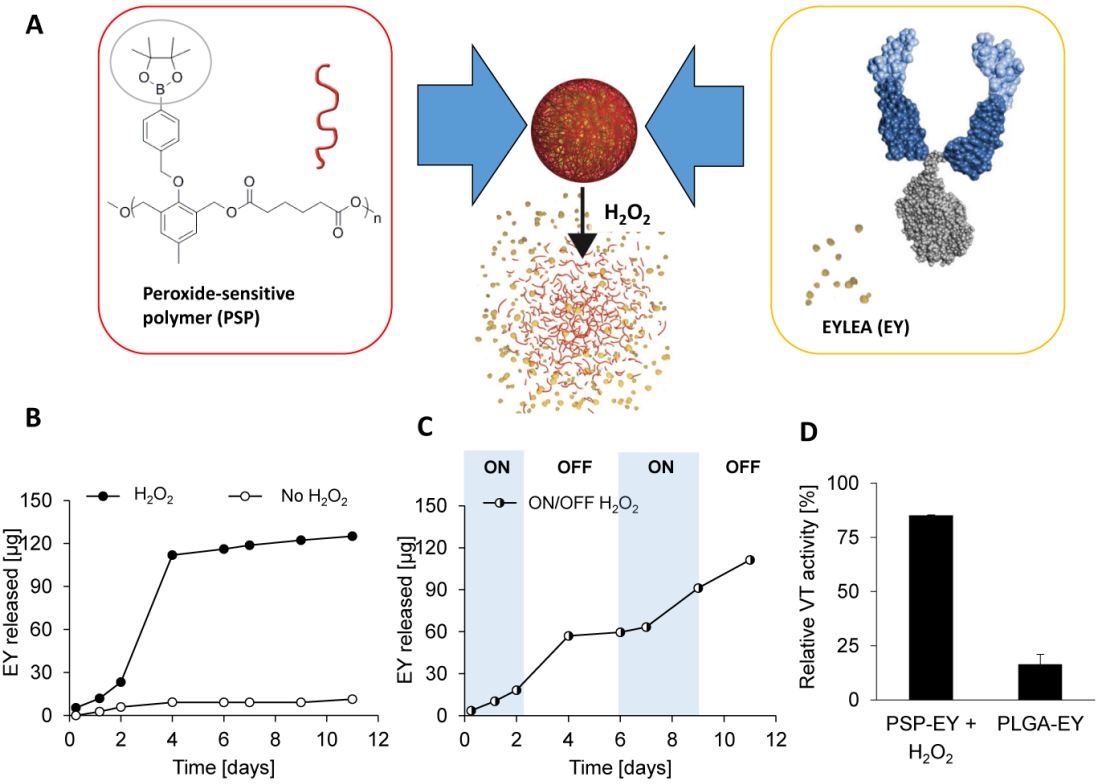

Figure 4.1: A. Schematic showing system design. B. Release of aflibercept (EY) from PSP nanoparticles in presence (black circles), and absence (white circles) of 100 mM H_2O_2. C. Triggered step-wise release of aflibercept from PSP nanoparticles by exposing (ON), and removing (OFF) 100 mM H_2O_2 during incubation. D. Activity of aflibercept released from PSP particles (PSP-EY), or PLGA particles (PLGA-EY) compared to native aflibercept by a functional ELISA assay.

4.4 Results

Formulated PSP and PLGA nanoparticles (NPs) were monodisperse at 231 ± 25 nm and 254 ± 20 nm by DLS (Figure 4.7A), their morphology round (Figure 4.7B). PSP particles rapidly released aflibercept in presence of H_2O_2 (Figure 4.1B), in contrast to non-responsive PLGA particles which, following the initial burst, slowly hydrolyzed, freeing the payload (Figure 4.8). Importantly, PSP particles exhibited H_2O_2-dependent release of aflibercept - the release rate increased in presence of trigger, and decreased when trigger was removed (Figure 4.1C). Upon re-introduction of H_2O_2 trigger, mimicking disease recurrence, EYLEA release rate again increased. This indicated the system's capability to deliver multiple drug doses by sensing the changes in the environment. EYLEA loading was 0.4 μg/mg, and its activity upon release from PSP was 80% of native by ELISA (Figure 4.1C). In contrast, EYLEA released from similarly-sized PLGA NPs was greatly diminished, likely due to acidic degradation products of PLGA.[43]

Intravitreal PSP-EY injected in P12 OIR neonates inhibited angiogenesis, increasing avascular areas by 40% and reducing neovascular areas by 50% compared to controls on retinal flat-mounts at P17 (Figure 4.2B). This effect was comparable to that of an injection of equal dose of free EYLEA (EY), and statistically different from all other experimental groups ($p < 0.01$), most notably slowly releasing PLGA-EY ($p = 0.009$). Co-injection of PSP-EY with a peroxide scavenger, NAC,

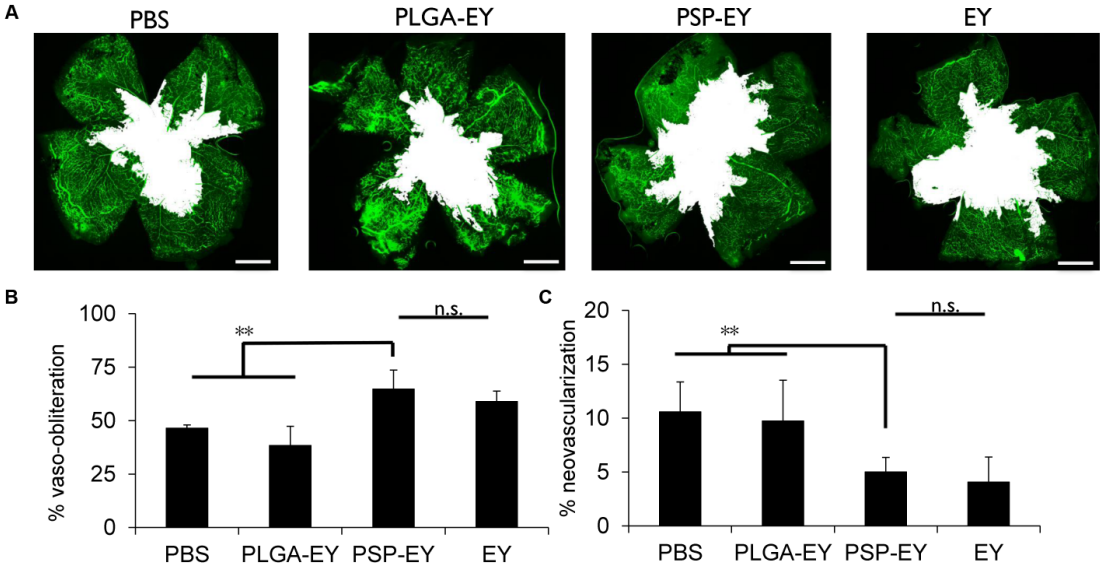

Figure 4.2: A. Fluorescence micrographs of flat-mounted retinas, with blood vessels stained green through a perfusion of FITC-Dextran before euthanasia. White area delineates avascular area of the flat-mount. Scale = 100 μm. B. Quantification of avascular areas on micrographs normalized to whole retina size (% vaso-obliteration). n = 4, ** indicates $p < 0.01$. Error bars represent SEM. C. Quantification of neovascular areas on micrographs compared to whole retina (% neovascularization). n = 4, ** indicates $p < 0.01$. Error bars represent SEM.

resulted in recovery of the OIR disease phenotype, suggesting H_2O_2-dependency of drug release *in vivo* (Figure 4.9).

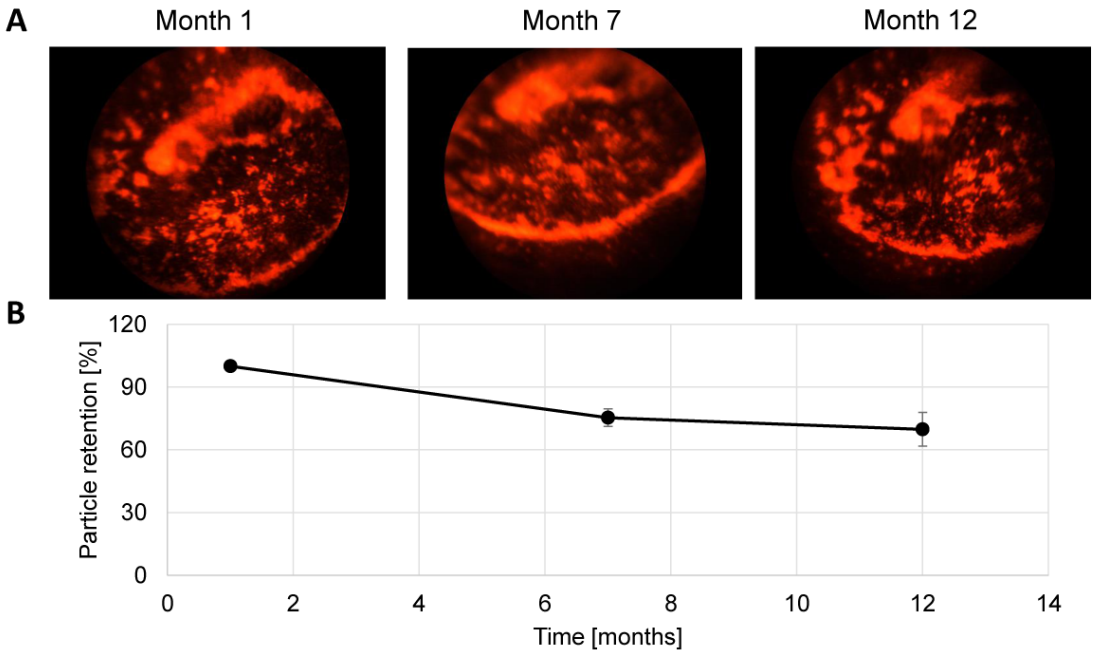

Figure 4.3: A. In-vivo retinal fluorescence micrographs of rhodamine-labeled PSP particles injected IVT. B. Quantification of PSP particle retention from retinal micrographs in A. n = 6. Error bars represent SEM.

After 12 months in healthy animals, approximately 70% of the particles remained in the eye (Figure 4.3). Throughout the study, nanoparticulate implant caused no adverse health effects on the animals. Heidelberg retina tomographs showed no difference in thickness of the outer nuclear layer, as well as overall retinal thickness, between particle- and saline- injected mice, up to 12 months after injection (p = 0.2-0.9), indicating no tissue toxicity (Figure 4.4AB). These results are consistent with quantified H&E-stained histology slices of retinal tissue

(Figure 4.4CD), as well as those reported in literature.[44]

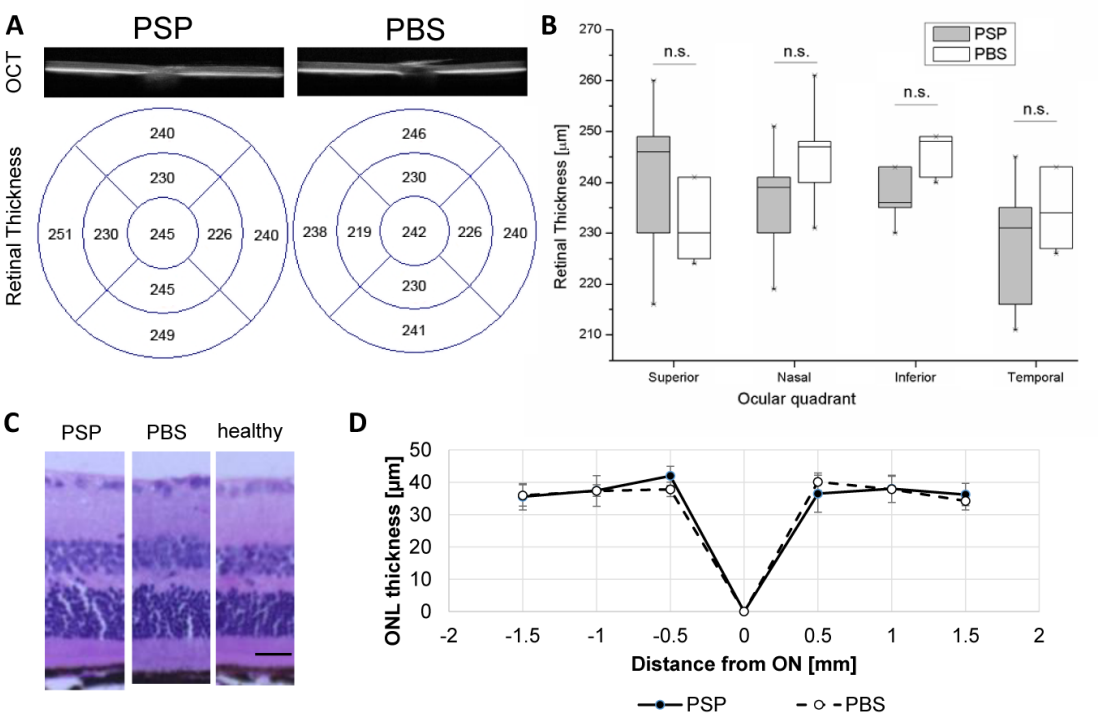

Figure 4.4: A. Heidelberg optical coherence tomographs (OCT) comparing sagittal sections of PSP- and saline-injected eyes. ETDRS grids below show quantified retinal thickness from OCT scans. B. Comparison of retinal thickness in four quadrants of the eye between PSP- (grey) and saline-injected (white) eyes. n = 4. C. Micrographs of H&E stained retina slices comparing PSP-injected, PBS-injected, and healthy animals. Scale bar = 25 μm. D. Quantification of micrographs from C comparing PSP- (solid line) and PBS-injected (dashed line) eyes. n = 4. Error bars represent SD.

Electroretinography testing 12 months post-injection showed no difference in scotopic potentials between the particle- and sham- injected, and healthy mice, indicating no visual function loss (p = 0.6, Figure 4.10). Scotopic visual acuity measured in optomotor response testing was near 0.3 cpd for all experimental groups (Figure 4.5B), consistent with the expected acuity for 1.5-year-old mice.[45]

Similarly, we found no differences in contrast sensitivity one year post-implantation between particle-, sham-injected, and healthy animals (Figure 4.5C).

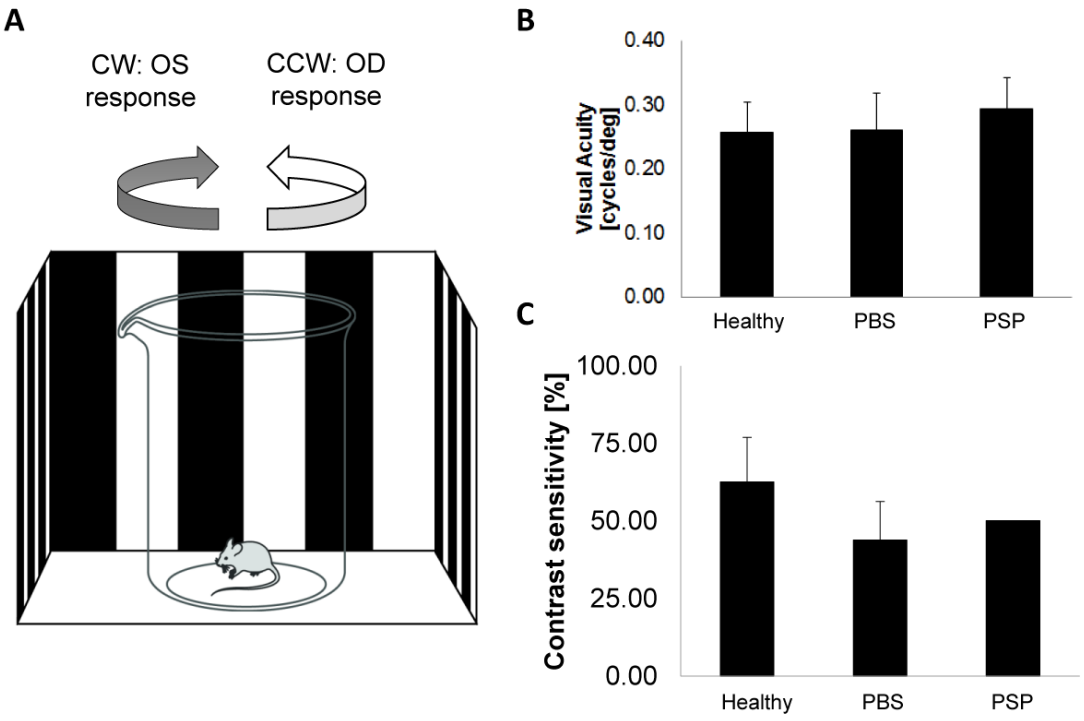

Figure 4.5: A. Schematic representation of the experimental setup for visual acuity measurements. B. Comparison of visual acuity between healthy, PBS-injected, and PSP-injected eyes. n = 4. Error bars represent SD. C. Comparison of contrast sensitivity between healthy, PBS-injected, and PSP-injected eyes measured at 0.1 cycles/deg. n = 4. Error bars represent SD.

In a murine model of laser-induced choroidal neovascularization (CNV), inflammation triggered release of EYLEA (EY) from PSP resulted in attenuation of blood vessel growth on the choroid as compared to slow-degrading PLGA nanoparticles ($p = 0.02$), comparable to that of free drug (Figure 4.11). More importantly, when CNV was induced 3 months post-implantation, CNV spots in eyes treated with PSP-EY decreased an average of 28% compared to all other experimental

groups (Figure 4.6).

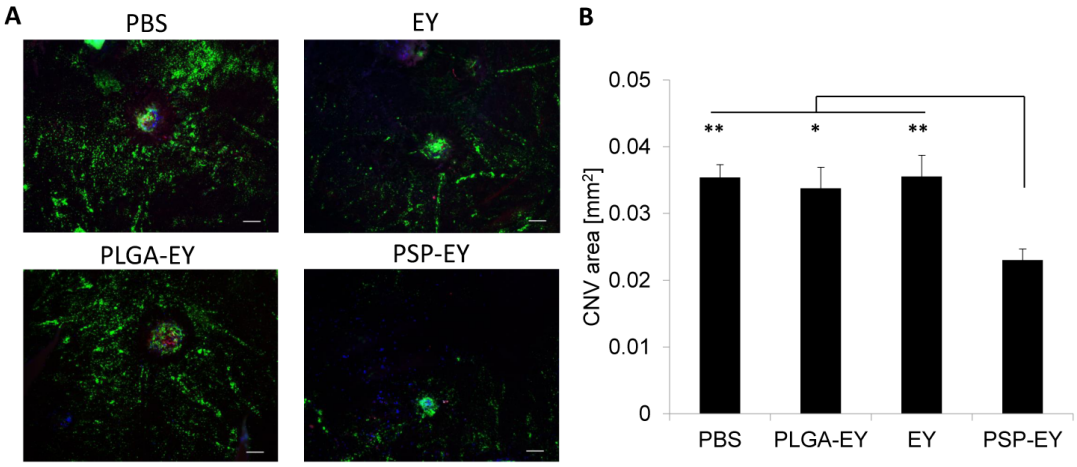

Figure 4.6: A. Fluorescence micrographs showing stained CNV spots. Red - isolectin B4, Green - FITC-Dextran; Blue - DAPI. Scale = 100 μm. B. Quantification of CNV spot sizes between experimental groups. * $p < 0.05$; ** $p < 0.01$. Error bars represent SEM.

4.5 Discussion

Long-term management of pathological angiogenesis in the eye remains a pressing problem. The American Academy of Ophthalmology Preferred Practice Pattern for neovascular AMD indicates that following the initial aggressive treatment every 4 weeks to reduce the macular fluid, the treatment follow-up intervals varies depending on the clinical findings and judgement of the treating ophthalmologist. These can range monthly to bimonthly injections, treat-and-extend, or as-needed treatment regimes. While there is no clear consensus on which of these treatment plans is better, the doctors act with patients' best interest in mind -

prevention of vision loss while minimizing treatment burden. This is imperative for the primarily elderly AMD patient population.

Bio-responsive drug delivery systems aim to alter that equation by tailoring the delivery of the drug to the presence of disease markers, in this case presence of ROS. This would allow for minimization of both the treatment burden and risk of vision loss. Translation of these types of systems needs to be coupled with deepening the understanding of the bioenvironment of the diseased tissue. While there is strong evidence for an association between AMD and oxidative stress levels,[46,47] it is not known what the ROS levels are, especially in a varied patient population. ROS levels in animal models also differ from those in patients. Further investigations are required to find the right balance of sensitivity, specificity, and stability of these types of smart drug delivery systems.

Here we presented a proof of concept drug delivery system that regulates release of anti-angiogenics in the eye based changes in ROS concentration in murine disease models. The system can respond to disease recurrence more quickly than engineered constant release rate systems up to 12 weeks post-implantation. This study describes an approach for long-term management of macular degeneration and other retinovascular diseases. Following further preclinical evaluation of ocular tolerance in larger animals, clinical studies would be required to confirm efficacy in treating multiple disease recurrences in a varied patient population.

4.6 Acknowledgments

The authors would like to acknowledge the National Institute of Health (5R01EY024134) as the funding source for these studies. NMR spectra were collected at the UCSD Skaggs School of Pharmacy and Pharmaceutical Sciences NMR Facility. Optical coherence and Heidelberg retina tomographs were acquired at UCSD School of Medicine Core Imaging Facility, and histology was acquired at Shiley Eye Center Histology Core, both supported by the National Eye Institute (P30EY022589).

Chapter 4, in full, is currently being prepared for submission for publication of the material. Nguyen Huu, Viet Anh; Zhu, Jie; Luo, Jing; Collet, Guillaume; de Gracia-Lux, Caroline; Zhang, Kang; Almutairi, Adah. The dissertation/thesis author was the primary investigator and author of this paper.

4.7 Supporting Information

Table 4.1: qRT-PCR primers

Primer	sequence (5' $->$ 3')
mGAPDH-F	GTCAAGGCCGAGAATGGGAA
mGAPDH-R	TTGGCTCCACCCTTCAAGTG
mIL-1β-F	GGGCCTCAAAGGAAAGAATC
mIL-1β-R	TACCAGTTGGGGAACTCTGC
mTNFα-F	TCAGCCGATTTGCTATCTCA
mTNFα-R	CGGACTCCGCAAAGTCTAAG

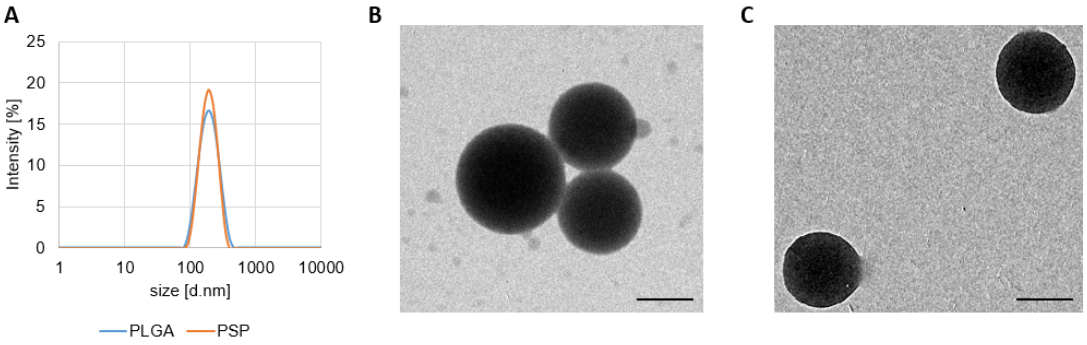

Figure 4.7: A. Dynamic light scattering intensity of formulated PLGA, and PSP nanoparticles. B. TEM micrograph of PSP particles. Scale = 200 nm. C. TEM micrograph of PLGA particles. Scale = 200 nm.

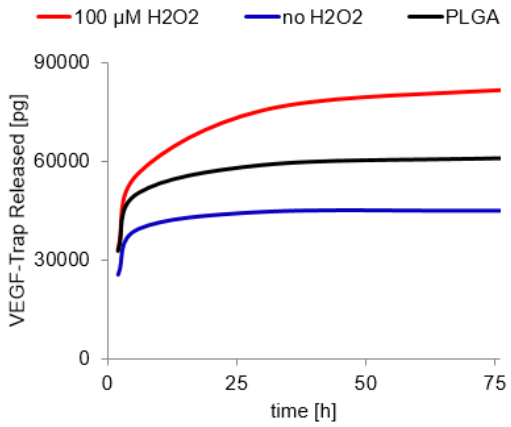

Figure 4.8: Release profile of VEGF-Trap from PLGA particles (black), PSP particles without peroxide (blue), and PSP particles in presence of 100 μM hydrogen peroxide (red).

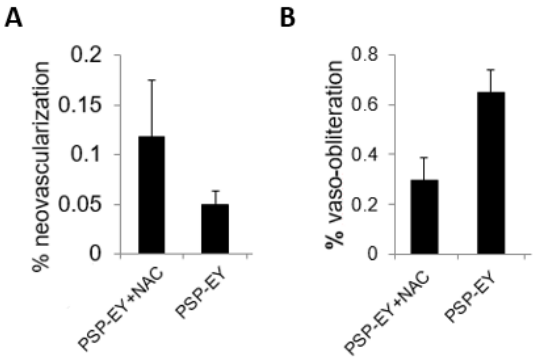

Figure 4.9: Quantification of neovascular (A) and avascular (B) areas in ROP eyes comparing eyes treated with PSP-EY particles, and eyes co-injected with PSP-EY particles and N-acetylcysteine (PSP-EY+NAC), a peroxide scavenger. Error bars represent SEM.

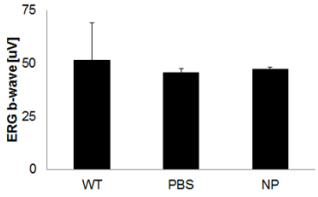

Figure 4.10: Comparison of ERG scotopic waves in eyes of healthy eyes (WT), eyes injected with saline (PBS), and eyes injected with PSP nanoparticles (NP). Error bars represent SD.

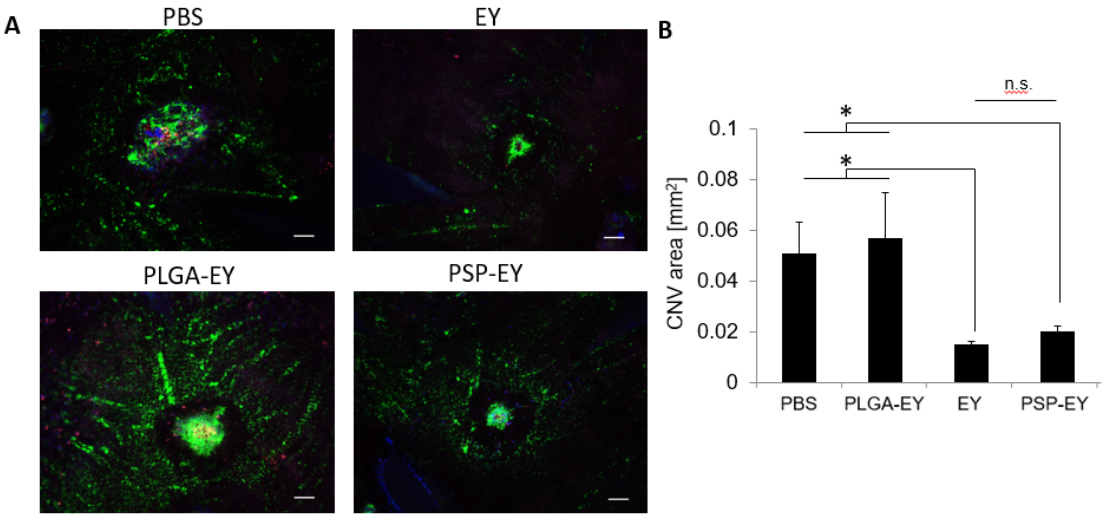

Figure 4.11: A. Fluorescence micrographs showing stained CNV spots. Red - isolectin B4, Green - FITC-Dextran; Blue - DAPI. Scale = 100 μm. B. Quantification of CNV spot sizes between experimental groups. * $p < 0.05$. Error bars represent SEM.

4.8 References

(1) R. Kawasaki, M. Yasuda, S. J. Song, S. J. Chen, J. B. Jonas, J. J. Wang, P. Mitchell and T. Y. Wong, *Ophthalmology*, 2010, **117**, 921–927.

(2) W. L. Wong, X. Y. Su, X. Li, C. M. G. Cheung, R. Klein, C. Y. Cheng and T. Y. Wong, *Lancet Global Health*, 2014, **2**, E106–E116.

(3) D. S. Friedman, B. J. O'Colmain, B. Munoz, S. C. Tomany, C. McCarty, P. T. de Jong, B. Nemesure, P. Mitchell and J. Kempen, *Arch Ophthalmol*, 2004, **122**, 564–72.

(4) G. C. Brown, M. M. Brown, S. Sharma, J. D. Stein, Z. Roth, J. Campanella and G. R. Beauchamp, *Trans Am Ophthalmol Soc*, 2005, **103**, 173–84, 173–84.

(5) D. H. Nguyen, J. Luo, K. Zhang and M. Zhang, *Discov Med*, 2013, **15**, 343–8.

(6) E. S. Gragoudas, A. P. Adamis, J. Cunningham, E. T., M. Feinsod and D. R. Guyer, *N Engl J Med*, 2004, **351**, 2805–16.

(7) G. Williams, *IVT Injections: Health Policy Implications*, 2014.

(8) J. Cosgrowe, *Medicare Information on Highest-Expenditure Part B Drugs*, tech. rep., United States Government Accountability Office, 2013.

(9) L. S. Jack, M. A. Sadiq, D. V. Do and Q. D. Nguyen, *Dev Ophthalmol*, 2016, **55**, 302–9.

(10) K. N. Le, L. Gibiansky, M. van Lookeren Campagne, J. Good, T. Davancaze, K. M. Loyet, A. Morimoto, E. C. Strauss and J. Y. Jin, *CPT Pharmacometrics Syst Pharmacol*, 2015, **4**, 595–604.

(11) G. M. Palmer, Z. Tiran, Z. Zhou, M. E. Capozzi, W. Park, C. Coletta, A. Pyriochou, Y. Kliger, O. Levy, I. Borukhov, M. W. Dewhirst, G. Rotman, J. S. Penn and A. Papapetropoulos, *Br J Pharmacol*, 2012, **165**, 1891–903.

(12) P. A. Campochiaro, L. P. Aiello and P. J. Rosenfeld, *Ophthalmology*, 2016, **123**, S78–S88.

(13) M. Singer, *F1000Prime Rep*, 2014, **6**, 29.

(14) R. A. Mittra and L. J. Singerman, *Optom Vis Sci*, 2002, **79**, 218–24.

(15) S. Sivaprasad and S. Oyetunde, *Clin Ophthalmol*, 2016, **10**, 939–46.

(16) J. L. Prenner, L. S. Halperin, C. Rycroft, S. Hogue, Z. Williams Liu and R. Seibert, *Am J Ophthalmol*, 2015, **160**, 725–31 e1.

(17) K. Berg, T. R. Pedersen, L. Sandvik and R. Bragadottir, *Ophthalmology*, 2015, **122**, 146–52.

(18) G. A. Lalwani, P. J. Rosenfeld, A. E. Fung, S. R. Dubovy, S. Michels, W. Feuer, J. L. Davis, J. Flynn, H. W. and M. Esquiabro, *Am J Ophthalmol*, 2009, **148**, 43–58 e1.

(19) A. E. Fung, G. A. Lalwani, P. J. Rosenfeld, S. R. Dubovy, S. Michels, W. J. Feuer, C. A. Puliafito, J. L. Davis, J. Flynn, H. W. and M. Esquiabro, *Am J Ophthalmol*, 2007, **143**, 566–83.

(20) A. C. Ho, B. G. Busbee, C. D. Regillo, M. R. Wieland, S. A. Van Everen, Z. Li, R. G. Rubio and P. Lai, *Ophthalmology*, 2014, **121**, 2181–92.

(21) J. L. Bourges, C. Bloquel, A. Thomas, F. Froussart, A. Bochot, F. Azan, R. Gurny, D. BenEzra and F. Behar-Cohen, *Adv Drug Deliv Rev*, 2006, **58**, 1182–202.

(22) Y. Ali and K. Lehmussaari, *Adv Drug Deliv Rev*, 2006, **58**, 1258–68.

(23) J. Barar, A. Aghanejad, M. Fathi and Y. Omidi, *Bioimpacts*, 2016, **6**, 49–67.

(24) V. Delplace, S. Payne and M. Shoichet, *J Control Release*, 2015, **219**, 652–68.

(25) A. C. Amrite, S. P. Ayalasomayajula, N. P. Cheruvu and U. B. Kompella, *Invest Ophthalmol Vis Sci*, 2006, **47**, 1149–60.

(26) F. Paganelli, J. A. Cardillo, A. R. Dare, J. Melo, L. A., D. R. Lucena, J. Silva, A. A., A. G. Oliveira, A. C. Pizzolitto, D. Lavinsky, M. Skaf, A. A. Souza-Filho, A. L. Hofling-Lima, Q. D. Nguyen, B. D. Kuppermann, R. Herrero-Vanrell, J. Belfort, R., P. Brazilian Ocular and G. Pharmaceutical Technology Research, *Expert Opin Drug Deliv*, 2010, **7**, 955–65.

(27) A. C. Amrite and U. B. Kompella, *J Pharm Pharmacol*, 2005, **57**, 1555–63.

(28) T. Iwase, J. Fu, T. Yoshida, D. Muramatsu, A. Miki, N. Hashida, L. Lu, B. Oveson, R. Lima e Silva, C. Seidel, M. Yang, S. Connelly, J. Shen, B. Han, M. Wu, G. L. Semenza, J. Hanes and P. A. Campochiaro, *J Control Release*, 2013, **172**, 625–33.

(29) B. M. Rauck, T. R. Friberg, C. A. Medina Mendez, D. Park, V. Shah, R. A. Bilonick and Y. Wang, *Invest Ophthalmol Vis Sci*, 2014, **55**, 469–76.

(30) B. V. Stanzel, Z. Liu, R. Brinken, N. Braun, F. G. Holz and N. Eter, *Invest Ophthalmol Vis Sci*, 2012, **53**, 490–500.

(31) C. G. Thanos, W. J. Bell, P. O'Rourke, K. Kauper, S. Sherman, P. Stabila and W. Tao, *Tissue Eng*, 2004, **10**, 1617–22.

(32) J. C. Gutierrez-Hernandez, S. Caffey, W. Abdallah, P. Calvillo, R. Gonzalez, J. Shih, J. Brennan, J. Zimmerman, J. C. Martinez-Camarillo, A. R. Rodriguez, R. Varma, A. Santos, G. Sanchez and M. Humayun, *Transl Vis Sci Technol*, 2014, **3**, 8.

(33) M. Humayun, A. Santos, J. C. Altamirano, R. Ribeiro, R. Gonzalez, A. de la Rosa, J. Shih, C. Pang, F. Jiang, P. Calvillo, J. Huculak, J. Zimmerman and S. Caffey, *Transl Vis Sci Technol*, 2014, **3**, 5.

(34) V. A. N. Huu, J. Luo, J. Zhu, J. Zhu, S. Patel, A. Boone, E. Mahmoud, C. McFearin, J. Olejniczak, C. D. Lux, J. Lux, N. Fomina, M. Huynh, K. Zhang and A. Almutairi, *Journal of Controlled Release*, 2015, **203**, 39–39.

(35) S. Joshi-Barr, C. de Gracia Lux, E. Mahmoud and A. Almutairi, *Antioxid Redox Signal*, 2014, **21**, 730–54.

(36) J. Kost and R. Langer, *Adv Drug Deliv Rev*, 2012, **64, Supplement**, 327–341.

(37) C. D. Lux, S. Joshi-Barr, T. Nguyen, E. Mahmoud, E. Schopf, N. Fomina and A. Almutairi, *Journal of the American Chemical Society*, 2012, **134**, 15758–15764.

(38) D. K. Shah, J. Veith, R. J. Bernacki and J. P. Balthasar, *Cancer Chemother Pharmacol*, 2011, **68**, 951–8.

(39) J. Holash, S. Davis, N. Papadopoulos, S. D. Croll, L. Ho, M. Russell, P. Boland, R. Leidich, D. Hylton, E. Burova, E. Ioffe, T. Huang, C. Radziejewski, K. Bailey, J. P. Fandl, T. Daly, S. J. Wiegand, G. D. Yancopoulos and J. S. Rudge, *Proc Natl Acad Sci U S A*, 2002, **99**, 11393–8.

(40) L. E. H. Smith, E. Wesolowski, A. Mclellan, S. K. Kostyk, R. Damato, R. Sullivan and P. A. Damore, *Investigative Ophthalmology & Visual Science*, 1994, **35**, 101–111.

(41) A. Stahl, K. M. Connor, P. Sapieha, J. Chen, R. J. Dennison, N. M. Krah, M. R. Seaward, K. L. Willett, C. M. Aderman, K. I. Guerin, J. Hua, C. Lofqvist, A. Hellstrom and L. E. H. Smith, *Investigative Ophthalmology & Visual Science*, 2010, **51**, 2813–2826.

(42) G. T. Prusky, N. M. Alam, S. Beekman and R. M. Douglas, *Investigative Ophthalmology & Visual Science*, 2004, **45**, 4611–4616.

(43) D. J. Hines and D. L. Kaplan, *Crit Rev Ther Drug Carrier Syst*, 2013, **30**, 257–76.

(44) C. Dysli, V. Enzmann, R. Sznitman and M. S. Zinkernagel, *Transl Vis Sci Technol*, 2015, **4**, 9.

(45) A. V. Kolesnikov, J. Fan, R. K. Crouch and V. J. Kefalov, *J Neurosci*, 2010, **30**, 11222–31.

(46) S. G. Jarrett and M. E. Boulton, *Molecular Aspects of Medicine*, 2012, **33**, 399–417.

(47) S. Khandhadia and A. Lotery, *Expert Reviews in Molecular Medicine*, 2010, **12**.